Stability Control via In-Wheel Motors of a Solar-Electric Vehicle

by Anna Lidfors Lindqvist

Thesis submitted in fulfilment of the requirements for
the degree of

Doctor of Philosophy

under the supervision of Dr. Paul D. Walker
and Dr. Ricardo P. Aguilera

University of Technology Sydney
Faculty of Engineering and Information Technology

December 2021

Certificate of Original Authorship

I, Anna Lidfors Lindqvist declare that this thesis, is submitted in fulfilment of the requirements for the award of Doctor of Philosophy, in the School of Mechanical and Mechatronics Engineering at the Faculty of Engineering And Information Technology at the University of Technology Sydney.

This thesis is wholly my own work unless otherwise referenced or acknowledged. In addition, I certify that all information sources and literature used are indicated in the thesis.

This document has not been submitted for qualifications at any other academic institution.

This research is supported by the Australian Government Research Training Program.

Signed: Production Note: Signature removed prior to publication.

Date: 30-12-2021

Stability Control via In-Wheel Motors of a Solar-Electric Vehicle

by

Anna Lidfors Lindqvist

A thesis submitted in partial fulfilment of the requirements for the degree of Doctor of Philosophy

Abstract

Emission reduction and increased safety are crucial for future mobility development. Vehicle dynamic control systems have an important role in vehicle safety and the reduction of weight in vehicle design has been proven to improve efficiency and reduce energy consumption. Very lightweight vehicles, however, impose a challenge when it comes to the vehicles handling stability, as their inertial parameters are impacted by additional load from e.g. passengers. As such, this thesis presents the study of vehicle dynamics of a lightweight customised solar-electric vehicle which is sensitive to the variation in loading conditions.

This thesis investigates the principle and engineering application of dynamic yaw moment control through simulation and real-time testing of the Australian Technology of Networks (ATN) solar car. The ATN solar car competed in the Bridgestone World Solar Challenge (BWSC), 2019; an Australian international biannual competition, where teams drive 3,000 km from Darwin to Adelaide in custom designed solar-electric vehicles. The cruiser class vehicles were introduced to recognise the necessity of sustainable transportation by encouraging practical vehicle designs with two or more seats. Drivers are exposed to long driving stints in vehicles with generally poorer handling and steering performance, owing to the need for lightweight, high performing designs. In such the novelty of this research should be considered in terms of the control theory and its application to a unique vehicle configuration. The design features, particularly being rear-wheel drive and very light

weight, impact controllability and dynamic behaviour of the case study solar car in this research. This type of research is very important for extreme cases of vehicle design that is present in the Bridgestone World Solar Challenge vehicles. In addition, investigating vehicles susceptible to extreme handling, the handling safety can be improved within solar racing sports, but also within the development of future lightweight road vehicles.

To undertake this investigation a simulation-based approach was achieved via co-simulation of the vehicle model and control. Using Siemens Amesim a nonlinear 15-DOF model was realised, incorporating the load transfer effects and nonlinear tyre characteristics. The control algorithms were developed in MATLAB/Simulink

This thesis presents four control method that can be applied to the rear in-wheel motors; Dynamic Curvature Control (DCC), Proportional–Integral Control (PI), Sliding Mode Control (SMC) and Model Predictive Control (MPC).

Using this simulation-based approach the dynamics of the vehicle is studied. Large variations load-to-curb weight ratios are linked to significant changes in parameters critical to control design for vehicle stability control system. Unique and highly customised vehicles, such as the lightweight solar car, are more susceptible to the impact of such variations when developing control methods. As such the influence of variation in loading condition and the effect of ignoring changes in inertial parameters is studied. The study demonstrated that by ignoring the change in the inertial parameters in simulation environments can produce an incorrect translation of the control performance.

Finally, to verify the applicability and performance of the simulations, open loop real-time testing was performed. This is done by implementing the control to the vehicles Control Area Network (CAN), via a dSPACE MicroAutoBox II. The evaluation was performed by comparing a slow speed baseline vehicle to tests with higher velocity, addition of passenger, low tyre pressure and cases of uneven tyre pressures. It was found that despite significant sensor and estimation errors due to compromises caused by COVID-19, the SMC and MPC both have vigorous performance capabilities and are safe for future closed-loop testing.

Acknowledgements

Firstly I would like to thank my supervisor Paul D. Walker whose expertise was invaluable in order for me to complete my research, it has been a pleasure to work alongside you and thanks for giving me the free hands to explore my research topic and the extracurricular task of managing students and the solar car team. I would like to thank and acknowledge my co-supervisor Ricardo Aguilera Echeverria who's invaluable knowledge and help with the control design and integration was essential for the success of this research.

I also want to give warm thanks to my colleague and friend Shiei Zhou for your expertise knowledge and patience when working together with software integration issues, control design, vehicle integration, testing and for always lending a helping hand when needed. I would like to extend a thanks to my colleague Mohamed Awadallah for sharing his knowledge and working with us on the installation and realisation of the real-time control set-up on the dSPACE MicroAutoBox II and the integration to the solar car.

I would like to acknowledge each of the ATN solar car team, team members and associates, thanks for being part part of the journey and acknowledgement of the contributors to some images and graphics in this thesis. I would also like to thank the technical team Richard Jamie, Bang Nguyen and Michael Lee for supporting the work and testing of the solar car.

In addition, I would like to thank my dear friend and previous colleague, Hasti Hayati, for always being an inspiration and motivating me to achieve my goals. Also many thanks to my partner, and of course the scrubblets, my close friends Somaia Ahmadi, Martin Do and Ben Hayles, for reminding me there is life outside of the PhD work.

Finally, I could not have completed my dissertation without the support of my family and friends back home, who despite being far away when times are tough, have encouraged me to be persistent and work hard. Special thanks to my mum, Lena Lidfors, who's expert academic knowledge saved me on numerous occasions throughout my journey, my dad, Thomas Lindqvist, who's technical expertise helped me with trouble shooting even if he was on the other side of the world, and my sister, Linnea Lidfors Lindqvist for keeping me grounded; but most of all for their unlimited support to always strive for the very best.

Contents

List of Figures

List of Tables

Acronyms & Abbreviations

2DOF	Two Degrees of Freedom
3DOF	Three Degrees of Freedom
ADAS	Advanced Drivers Assistance Systems
ATN	Australian Technology of Networks
BWSC	Bridgestone World Solar Challenge
CAN	Controller Area Network
DCC	Dynamic Curvature Control
DSC	Dynamic Stability Program
DYC	Direct Yaw Moment Control
ECU	Electronic Control Unit
ESC	Electronic Stability Control
ESP	Electronic Stability Program
EV	Electric Vehicle
GPS	Global Pointing System
IMU	Inertial Measurement Unit
MBD	Model-Based Design
MDoF	Multiple Degrees of Freedom

MF	Magic Formula
MAB	MicroAutoBox
MPC	Model Predictive Control
PI	Proportional Integral
PiL	Processor-in-the-Loop
RPC	Rapid Control Prototyping
SAS	Steering Angle Sensor
SMC	Sliding Mode Control
TV	Torque Vectoring
VCU	Vehicle Control Unit
VDC	Vehicle Dynamics Control
VSC	Vehicle Stability Control
UTS	University of Technology Sydney

Nomenclature

	General Notations
X	Robot Pose vector in 2D space. Consists of the position components $x,\ y$ and the orientation component ϕ.
Y	Position.
ϕ	Roll angle
θ	Pitch angle
ψ	Yaw angle
δ	Steering wheel angle
r	Yaw rate
F_x	Longitudinal tractive/breaking force of the tires
F_y	Lateral cornering force of the tires
F_z	Vertical/normal force of the tires
m	Total mass of the vehicle.
I_x	Moment of inertia around the x-axis
I_y	Moment of inertia around the y-axis
I_z	Moment of inertia around the z-axis
C_f	Tyre cornering stiffness of the front wheels
C_r	Tyre cornering stiffness of the rear wheels
r_w	tire radius
l	Wheelbase; the distance between centre of the front and rear wheels.
l_f	Length from the centre of the front wheel to COG.
l_r	Length from the centre of the rear wheel to COG.

t_r	Track; the distance between the centre line of two wheels on the same axle.
m_{fl}	Mass measured at the front left wheel.
m_{fr}	Mass measured at the front right wheel.
m_{rl}	Mass measured at the rear left wheel.
m_{rr}	Mass measured at the rear right wheel.
m_l	Left hand side mass, about the center line of the track.
m_{Right}	Right hand side mass, when added with $m_l = m$
m_f	Front mass in relations to the center of l
m_r	Rear mass, makes up m with m_f
h_z	Vertical height raised at the rear axis during COG measurement.
m_{fh_z}	front mass when raised at height (h_z)
l_{adj}	The adjacent length below the vehicle during raised height (h_z)
$m_{\Delta f}$	Front axle mass change

Publications

2021 **Lidfors Lindqvist A.**, Walker P.D. (2021) *Handling Dynamics of an Ultra-Lightweight Vehicle During Load Variation.* In: Oberst S., Halkon B., Ji J., Brown T. (eds) Vibration Engineering for a Sustainable Future. Springer, Cham. DOI:10.1007/978-3-030-47618-2_7

2020 **Lidfors Lindqvist A.**, Zhou S., Walker P.D. (2020) *Direct yaw moment control of an ultra-lightweight solar-electric passenger vehicle with variation in loading conditions*, Vehicle System Dynamics, DOI: 10.1080/00423114.2020.1853784

2020 **Lidfors Lindqvist A.**, Walker P.D. (2020) *Handling Dynamics of a Lightweight Solar-Electric Vehicle with Direct Yaw Moment Control.* In: Klomp M., Bruzelius F., Nielsen J., Hillemyr A. (eds) Advances in Dynamics of Vehicles on Roads and Tracks. IAVSD 2019. Lecture Notes in Mechanical Engineering. Springer, Cham. DOI: 10.1007/978-3-030-38077-9_136

Chapter 1

Introduction

In this chapter the research background is presented, together with the background information of the case study vehicle, the research aims and objectives and the thesis organization.

1.1 Background

Electrical vehicles have a driving range which is restricted by the capacity of their battery, which has increases the demand of highly efficient and streamlined vehicle designs and powertain layouts [1]. It has long been accepted that an effective way to improve the overall vehicle driving efficiency is by reducing the curb weight of a vehicle, or exploiting a lightweight design [2–4]. However, this can cause issues in terms of a vehicles driving dynamics as the reduction in mass result in a lesser normal force on the tyres. The normal force is used to define properties such as friction and cornering stiffness. As such, lower normal force reduces the ability for the vehicle to grip during cornering which may cause accidents.

This thesis investigates the dynamic behaviour of the custom designed Australian Technology of Networks (ATN) solar car, which participated in Bridgestone World Solar Challenge (BWSC), cruiser class, 2019. The Bridgestone world solar challenge is an Australian international biannual competition, where teams drive 3,000 km from Darwin to Adelaide

in custom designed solar-electric vehicles. The cruiser class vehicles were introduced to recognise the necessity of sustainable transportation by encouraging practical vehicle designs with two or more seats. Drivers are exposed to long driving stints in vehicles with generally poorer handling and steering performance, owing to the need for lightweight, high performing designs. Because these vehicles are designed for energy efficiency, there are no spoilers or wings to apply downward force for better grip during cornering which is usually the case for high-performance race cars. Improving the vehicle handling is particularly important to increase safety within solar racing as a sport, but also for the emerging development of lightweight production vehicles.

During the Bridgestone World Solar Challenge, 2019, several teams were forced of the road due to experiencing sudden wind gusts, either produced by nature or by passing road trains. Solar cars are typically designed for energy efficiency, in such for low drag and weight. In terms of vehicle stability, low vehicle mass and drag coefficient unfavorably affect crosswind stability. However, numerous factors determine the vehicle behavior in crosswind, which makes it rather complex [5]. Some of the factors that determine the vehicles behavior include (i) reaction of the driver (ii) characteristics of the wind e.g. velocity, direction, flow etc. (iii) driving conditions and (iv) vehicle characteristics.

Lightweight vehicles are also more susceptible significant changes in inertial parameters when the weight of driver, passenger/s and/or luggage is introduced [2]. As the curb weight of a vehicle is reduced, the ratio between its loaded weight and curb weight, load-to-curb-weight ratio, radically increase. Although the increase of total mass is conspicuous, large load-to-curb-weight ratios are linked to changes in inertia, location of centre of gravity and tyre properties; all which are important parameters when developing control strategies.

In recent years the use of in-wheel motors have increased in popularity [1, 6]. These motors are located inside of the wheel, rather than on-board the chassis as in conventional combustion engine vehicles. The ATN solar car, is rear wheel driven and equipped with two in-wheel motors. Some of the key benefits with in-wheel motors include; increase of space in the chassis, a more even weight distribution, low energy consumption and increased controllability due to the lower response time of the electric motors [6–8]. These motors can also control the braking power of the vehicle, eliminating the need of traditional

hydraulic brake systems [9]. Due to the regulations of the BWSC, the ATN solar car is equipped with a mechanical braking system and this is not investigated further in this thesis.

The flexibility and controllability of in-wheel however has become a central part when it comes to the development Advanced Drivers Assistance Systems (ADAS) [6]. ADAS is a collective term for electronic systems which either warn the driver or intervene, to avoid or reduce severity of of accident. The ability to control in-wheel motors individually, allows for implementation of an ADAS known as Direct Yaw Moment Control (DYC), or Torque Vectoring (TV). Traditionally the concept of DYC has been used to differentially brake the wheels to produce a corrective yaw moment to ensure stability during extreme conditions [10, 11]. However, this is achieved at the expense of reduced vehicle speed due to the increase of overall breaking toque [11]. Independently driven motors allow for direct manipulation of toque, making it possible to produce the assistive yaw moment without reducing overall speed and is a well recognised method to improve the lateral stability and handling of a vehicle with independent wheel drive [1, 6, 7, 12].

1.2 The ATN Solar Car Project

The ATN is a group of Australia's most innovative and enterprising universities, at the time of the vehicles development these included; University of Technology Sydney (UTS), Queensland University of Technology (QUT), Royal Melbourne Institute of Technology (RMIT), University of South Australia (UniSA) and Curtin University. The joint effort of these universities makes up of the ATN solar car team, which designed, built and competed with the solar car, Priscilla, in the Bridgestone World Solar Challenge (BWSC) 2019.

The Bridgestone World Solar Challenge is bi-annual race from Darwin to Adelaide, stretching 3,000 km across the Australian outback. The vehicles competing have been designed to use solar power as their source of energy. The ATN solar car has a top speed of 130 km/h and has a driving range of 1,200 km without external charge. The car competed in the cruiser class category, which require the vehicle to have enough room for a driver and at least one passenger. The concept of the cruiser class is to recognise sustainable

transportation alternatives and encourage a design that is both practical and acceptable by consumers.

As such, the ATN solar car is a lightweight two-seated solar electric vehicle, driven via two electric in-wheel motors located in the vehicles two rear wheels. The car has been designed for practicality and efficiency which produces a unique test bed for research into dynamic handling.

FIGURE 1.1: The ATN solar car in relations to commercial vehicles. Image: ATN solar car project, 2019.

A major part of my research journey was my work with the ATN solar car team, where I was nominated Team Manager. I started by co-managing engineering students and interns at UTS in early 2018. During this time I was also the lead supervisor of a Bachelor thesis on down-scaled version of the solar car. I then accepted the challenge of leading a cross-disciplinary team from five universities through the virtual phase and into the competition. It was an excellent opportunity for me to widen my leadership and management skills,

leading, engaging and/or leasing with students, academics, researchers, industry, media, government and other associated parties.

FIGURE 1.2: The ATN solar car close-up. Image: ATN solar car project, 2019.

The main highlight of the project was that the team managed to develop a vehicle from across five states, but also that beat teams with more than 20 years experience by achieving:

- Lightest cruiser class vehicle in the competition
- Fastest Cruiser Class vehicle in dynamic scrutineering
- Top 10 of the whole competition speed assessment around track (against speed-designed vehicles).
- The 2nd fastest of the whole competition dynamic maneuvering assessment.

- The ATN solar car team was one of two teams (out of 45), that was invited to partake in the Chief Minister reception at the Northern Territory Parliament house.

1.3 Contributions

The global interest in the reduction of injury and fatality in traffic is not only limited to the vehicle industry, but also national and global governance as well as the general public. In new cars and commercial vehicles, some ADAS functions are so effective they are mandatory in certain countries. The reduction of injury and fatality in traffic has always been a well argued topic. The exploitation of lightweight design and reduction of curb-weight is known to improve a vehicles driving efficiency, however at a cost of the vehicles handling capability. Since the automotive industry is moving towards lighter vehicles to improve their efficiency and to reach environmental targets, it could be said that the issue with instability due to constricted vehicle weight is an upcoming issue.

Literature examining lightweight vehicles tend to focus on small sized vehicles, with narrow track and wheelbase, whilst the ATN solar car is designed as a consumer friendly vehicle with a larger track and wheelbase compared to its weight, which better corresponds with commercial vehicles. In addition, in solar car racing, drivers are exposed to long driving stints in vehicles with generally poorer handling and steering performance, owing to the need for lightweight, high performing designs.

The value of investigating lightweight vehicles, rather than commercially available vehicles, is that they are more susceptible to extreme handling, which normally is not considered. As indicated in [2], the load-to-curb weight ratio over-proportionally increase as curb weight is reduced, even for fairly low relative additional loads. The unique and highly customised lightweight vehicle in this research is more vulnerable to the impact of such variation than current commercial passenger vehicle. Particularly because the reduced weight, together with the track and width, contributes to a larger possibility of location of additional mass, which would then contribute to larger variations. In addition, very light vehicles have smaller normal force which affect their ability to obtain the same grip as commercial vehicles during cornering, influencing their handling. Whereas high-performance

race vehicles are equipped with spoilers or wings to apply downward force to customise their handling, the ATN solar car does not due to being optimised for straight driving efficiency. Introducing a yaw control has the potential to prolong the maximum cornering force [13].The novelty of this research should be considered in terms of the control theory and its application to a unique vehicle configuration.

The direct implications of the success of this research is that this research will provide fundamental knowledge into the dynamic behaviour of vehicles with extreme design parameters such as the ATN solar car and; (i) provide better vehicle safety, thereof reduce the number of injury and/or fatality (i.e. from improving stability and handling during emergency manoeuvring), (ii) explore the impact of load conditions on consumer sized lightweight vehicles (iii) allow for tailoring of the vehicles dynamic behaviour,(iv) impact of controllability due to inertial parameters and dynamic behaviour of the vehicle.

As such, this research looks improve handling safety within solar racing sports and contribute fundamental knowledge into solving handling issues for emerging development of lightweight vehicles. The aims, objectives and corresponding significance are presented in the following sections.

1.3.1 Aims

i. To identify the dynamic behaviour of the ATN solar car, which has a streamlined design, optimised for aerodynamics and lightweight in a simulation environment.

ii. To produce a control strategy that ensures safe handling during uncertainties caused by cross-wind or due to changes in loading conditions, by exploiting the individual drive in-wheel motors

iii. To verify the properties of the controller in real-life environment.

iv. To validate the control strategy.

1.3.2 Objectives

i. Develop a simulation of the ATN electric solar vehicle to simulate the dynamic behaviour.

ii. Develop a control strategy utilising in-wheel motors to improve dynamic behaviour.

iii. Real-time validation of the control response by implementing the control to the vehicle.

iv. Validate and compare the control by implementing it on the ATN solar vehicle.

1.3.3 Significance of Aims and Objectives:

i. The simulation allows for the investigation into the vehicle dynamics and the different vehicle states (i.e. sideslip and yaw rate) during the emergency manoeuvres and external influences. The information from the simulation will provide details required to design of the control system. The measure of success is that the vehicle model corresponds with the properties of the actual vehicle.

ii. The control system has the potential to improve the stability during emergency manoeuvres and externally unstable conditions which otherwise could have detrimental outcomes. The novelty of the controller has the ability to respond to the dynamic challenges that comes with the extreme design conditions, specifically the instability due to the large wheelbase and track area compared to its weight. The measure of success for this objective is that the controller improves the stability when enabled compared to when disabled in a simulated environment.

iii. The implementation of the controller on the vehicle provides physical evidence of the control systems properties are safe to be enabled. The measure of success for this objective is that the torque output should be within safe regions and not produce large sudden changes.

1.4 Methodology

Model-Based Design (MBD) process is a method used to design control systems and is a systematic approach for structuring the design process. The MBD process is alike to the V-model, which is a common project management method which graphically represents the system development life-cycle. It is often divided into the definition of a project, time, test and integration. This research is structured as per Figure 1.3 and detailed in the subsequent sections.

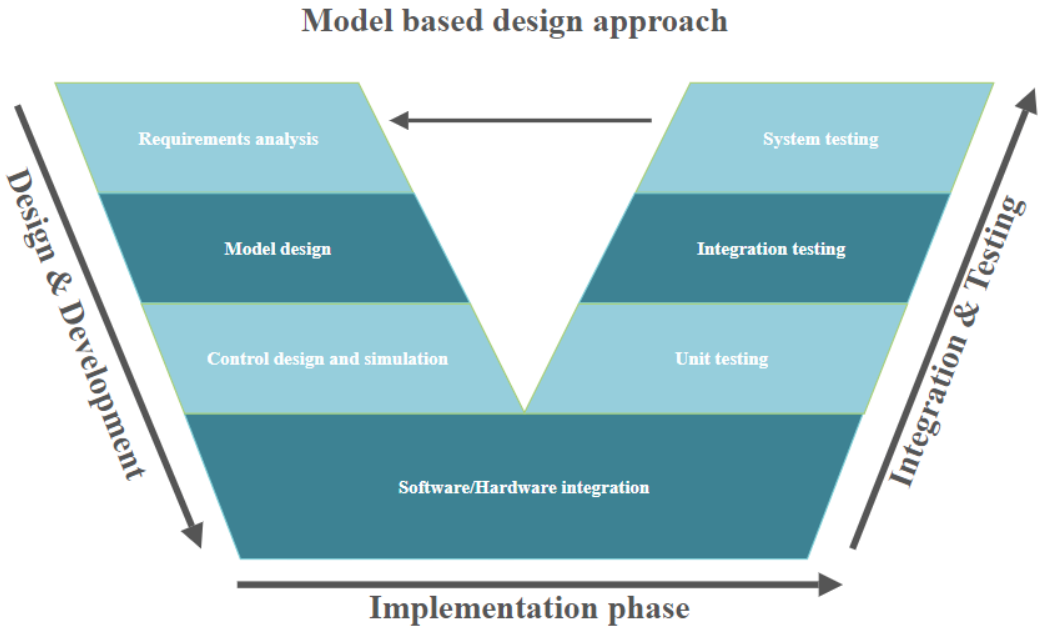

FIGURE 1.3: Flow chart of control logic.

1.4.1 Design and Development

Simulation is the imitate operation, function and/or behaviour of a real system. The simulation models are derived from the mathematical model of the system and allows for the study of how the vehicle will behave. In this research, Siemens Amesim^{TM} is used for vehicle modelling and MATLAB Simulink is used for control development. The co-simulation between these software allows for the study of the simulated vehicle behaviour when the control is integrated, which aid in the tuning and design iterations process.

Due to the nature of the solar car project, the tuning of the model and control was reiterated as presented in each chapter and section. This is due to the concurrent design and build of the real vehicle.

1.4.2 Implementation

To verify a control system in a real-time test-bed environment the Simulink control model is implemented into the actual ECU hardware. It relies on acceptable model simplifications and selection of robust fixed-step solvers for implementation and simulation of the vehicle.

In this research the control was implemented to the vehicle using dSpace MicroAutoBox II, which is a real-time system for control applications and operates like an ECU.

1.4.3 Integration and Testing

Adjustments were made for the dSpace MicroAutoBox II to run with the control strategies in real-time and then implemented to the vehicle to allow for system testing. During this time sensor tuning and adjustments were made.

1.5 Limitations

This research is limited by the engineering application, availability of advance equipment and funding. Since the final outcome is physical application of the controller to the ATN solar car, the safety of participants, property and the vehicle must be considered. Due to the time overlap of the vehicle development and inability for direct measurements, some of the vehicle parameters have been estimated as noted in the corresponding sections.

Due to the impact of COVID-19 there were considerable delays, loss of efficiencies and budget which have impacted this research.

The delivery of the solar car was immensely delayed due to state-wide lockdown, upon arrival works were on hold until delivery of the custom battery from another state.

The lack of budget reduced the ability of obtaining the manpower required to get the vehicle road ready, as such concurrent works had to be ceased whilst focus was on maintenance. As such, the Processor-in-the-Loop (PiL) set-up was disregarded, this was decided to allow for the set-up of communication between the MicroAutoBox and the vehicles CAN network.

The test phase has been limited and a less than ideal test area was used for driving performance with limited area and a non-flat surface. As such the control will not be enabled, however data attained can be used to examine the control viability and parameter estimation and tuning.

1.6 Thesis Outline

This thesis is organised as follows:

- **Chapter 2:** This chapter presents a literature review, focusing on direct yaw moment control.
- **Chapter 3:** The vehicle simulation modeling and desired handling is derived in this chapter.
- **Chapter 4:** In this chapter the control hierarchical layout is presented together with the four control strategies which were development.
- **Chapter 5:** This chapter includes the simulation studies, highlighting the importance of control of a lightweight solar car and the influence load has on the vehicle and control properties.
- **Chapter 6:** This chapter presents the vehicle integration and parameter estimations in order to update and run the controller successfully.
- **Chapter 7:** In this chapter real-time testing is performed during different load cases and tyre pressures in order to study the response of the control.

- **Chapter 8:** In order to confirm the control is safe to enable and to support future work using the simulation model, this chapter presents the model validation and the correlation of the control properties in comparison with Chapter 7.
- **Chapter 9:** This is the final chapter, which gives a brief summary of the thesis and its contribution, future work and recommendations.

Chapter 2

Review of Related Work

In this chapter a literature review or related work of direct yaw moment control is presented in order to get an overview of current research and possibilities to improve vehicle safety.

2.1 Introduction

The unceasing concern of the environmental impact of pollution from the transportation sector has increased the demand of energy efficient and low emission vehicles. Due to this global rise in demand, need for further research in sustainable transportation is more crucial than ever [6]. The vehicle electrification offers an energy efficient solution to emissions resulting from the transportation sector, yet, these vehicles will always have a driving range limited to their battery [1]. The reduction of vehicle curb weight, or lightweight design, has long been accepted as a solution to improve overall vehicle driving efficiency [3, 4]. However, this can cause issues in terms of vehicle handling dynamics, even for every day driving scenarios [2].

During emergency manouvers and/or unexpected changes in external conditions a vehicles may experience unexpected unstable and dangerous behaviour. Vehicle stability systems aim to ensure stability during these critical conditions as well as during normal conditions to improve manouverability and handling [14]. Introducing active control, such as DYC, can assist in maintaining the desired path and stability conditions [15–17]. Direct yaw

moment control is the manipulation of torque to generate an assistive yaw moment, which can increase lateral stability and handling of a vehicle [1].

The new generation of electric vehicles offer a new type of vehicle design and layout which can improve efficiency and safety [18]. A major research interests in the vehicle industry is the change in layout of the propulsion system, which has made a shift towards the use of in-wheel motors [6]. The flexibility and controllability of the motors have become a central part when it comes to the development of direct yaw moment control [1, 6]. Independent wheel drive configurations allows for the control of the separate wheels, which can improve the vehicle dynamics through torque distribution, also known as torque vectoring [1]. Which is one of the most recognised ways of improving the dynamic behaviour and stability independent wheel drive vehicles [6, 7, 12].

The increased popularity of utilising in-wheel motors is due to the ability to improve vehicle performance significantly as they; (i) provide more precise and direct torque allocation (ii) reduces overall vehicle weight, (iii) increase the space within the chassis, and (iv) generally improve the energy efficiency [3, 6–8, 16]. Since these motors also can control the braking power, they eliminate the need of traditional hydraulic brake systems [9]. Existing research on electrical vehicles with in-wheel motors is quite substantial, however these are often focused on passenger cars or smaller urban cars [19].

2.2 Vehicle Handling and Stability

Vehicle handling generally refers to the vehicles ability to respond to steering commands.The two basic concepts of handling refer to the vehicle ability to remain on a desired path during maneuvering or due to external disturbances. Vehicle stability is discussed in terms of the deviation of the desired path, also referred to as driver intent, which is evaluated from a stability factor which is derived from the vehicles designed steering behaviour. The drivers intent is defined as the proportional turning of the vehicle and the steering wheel angle, deviation would be considered as a mismatch between the two. The vehicles steering behaviour is divided into three categories (i) neutral steer, which follows the intended

path (ii) understeer, which cause the vehicle to turn less than intended, and (iii) oversteer, where the vehicles turns more than intended.

The steering behaviour can be defined by the understeer gradient, which is a measure of how much steering is required for a steady state turning as a function of lateral acceleration. By estimating the stability region the vehicles stability boundary can be found, which is leveraged for the integration of stability controllers [20]. A vehicles steady state response during cornering is often assessed in terms of its understeering factor [21]. The understeer and oversteer radically change with the vehicle velocity, which cause an unstable behaviour of a vehicle [19]. The characteristics of a vehicles understeer behaviour can successfully be altered through yaw rate based torque vectoring controllers [22]. Vehicles with torque vectoring systems can be designed to achieve nearly any desired steer behaviour compared to vehicles without, where the characteristics are decided from properties in the vehicle structure [21]. The deviation of the intended driver path during cornering is due to the generation of lateral forces at the tyres [23]. The inequality of magnitude of the front and rear forces produce either an excessive or reduced yaw, which is what results in under- or oversteering behavuiour. Researchers have been able to counteract these tire forces by introducing a counteracting or assistive yaw moment, which we know as the direct yaw moment control [24, 25].

This explains why the vehicle steering wheel angle also can reduce the turning resistance during cornering. For a vehicle to remain at a constant cornering trajectory at a set velocity, the steering angle cannot be reduced without being compensated for. In such by adding the counteractive yaw moment via direct yaw moment control techniques, the turning angle can be reduced and in such the turning resistance [1]. Torque vectoring also allows for greater friction attainability which has the possibility to prolong the maximum cornering force [13].

The vehicle sideslip angle is the angel between the velocity direction, longitudinal axis and the sideslip rate [26]. The slip angle during cornering can easily be controlled by the manual steering by the driver during low lateral accelerations, however as the acceleration increase this becomes less effective since the tire sideslip angle also increase with acceleration [25].

The sideslip angle is an important vehicle state, as it is used in the control architecture to re-establish the stability of the vehicle [26].

2.3 Load-to-Curb Weight Ratio

Load-to-curb weight ratios are used to describe the contrast between the weights of an empty vehicle compared to its laden weight [2]. Thus, the lower cub weight of a vehicle, the higher the load-to-curb-weight ratio will be in comparison to heavier vehicles with the same additional load [2, 3]. As such, the curb-to-load weight ratio progressively grows with the reduction of curb weight [3]. In particular for lightweight vehicles, this means that loading scenarios can substantially differ between each trip [3]. Large load-to-curb weight ratios are linked to significant changes in parameters such as location of centre of gravity, inertia and direct influence of the tire properties [2, 3, 27, 28].The influence of payload and its effect on the vehicle states was presented by [29]. In [27] about 600 load scenarios were calculated, with the variation of passenger and load weights, and an Unscented Kalman filter based on normal ride conditions was proposed to improve dynamic controllers. In [30], a VSC with adaptive mass, tyre cornering stiffness and road surface environments was proposed.

The implementation of DYC systems with in-wheel motors deal with handling changes in loading conditions have also been investigated in literature. In [3], in-wheel motors were used to compensate for the influence of loading condition, by introducing a yaw rate gain which match the unloaded vehicle handling characteristics. In [31] an adaptive radial basis function network sliding mode control (ARBFN-SMC) was proposed and the variation of cornering stiffness and unknown external disturbance was studied. Although research indicates that robustness during sensitivity studies in simulation environment due to change in mass is possible, there is not always a clear indication if the change in the vehicles inertial parameters have been considered. Literature has shown that there is potential for using DYC systems to deal with variation in load [3]. However, vehicles as light as the ATN solar car have not been considered.

2.4 Direct Yaw Moment Control

Critical maneuvers and hazardous driving conditions can cause unstable vehicle behavior, which can lead to accidents. To improve vehicle handling, active chassis control systems have become a standard in commercial vehicles and is extensively explored in literature. These systems are commonly referred to as Vehicle Stability Control (VSC) Systems, Vehicle Dynamics Control (VDC), Electronic Stability Control (ESC) or Electronic Stability Program (ESP). Most which are based of the introduction of an assistive yaw moment in order to ensure a desired handling, hence the referenced direct yaw moment control [32].

Most direct yaw moment control strategies work under the same principle, where the basic concept is to vary the torque between the left and right hand side in order to generate the assistive yaw moment [1, 6, 19**?**]. There are several strategies used to achieve this, such as; differential breaking [1, 30], torque differentials [33, 34], active steering [35], and the integration between these systems [32].

The brake based methods, are passive controls that limit the torque by applying the brake to the individual wheels. This has been found to improve the vehicles stability during critical conditions by reducing the under steer behaviour. However, the drawbacks with this method is that the reduction in speed result in an increased energy consumption as well as affect the driving experience and comfort [1, 36].

Torque differentials actively shifts the torque between the driving wheels either mechanically or electronically. Most commercial electric vehicles often have a similar powertrain layout as conventional combustion engine vehicles, with a single motor which acts on a mechanical differentials [33, 37]. The mechanical differentials comprise of gears which split torque between the driving wheels, commonly in order to allow for faster speed of the inner wheel during cornering [33]. The predominant drawback with mechanical differentials is that they add to the drive line in terms of components an weight, and if frictional multiplate clutches are used additional energy is required [1]. Replacing mechanical differentials with electronic differentials, can lower the energy consumption due to higher powertrain efficiency and reduction in weight [33, 37, 38].

Electronic differential techniques provide the required torque directly to each of the driving wheels, in order to enhance the dynamics of the vehicle [1]. A method which is also referred to as TV [3, 32] This is achieved from the use of multiple motors which can be located either on-board or within the wheel [21]. The in-wheel motors are optimal when it comes to adopting VSC strategies as torque can be modulated by each individual driving wheel with relatively precis torque at a desired ratio, which eases the implementation of torque vectoring [3, 16, 19, 32, 39].

In comparison to frictional break methods, safe driving conditions can been extended during transient emergency manoeuvres for greater velocities when implementing torque vectoring through the drivetrain [21]. In addition, many premium vehicle manufacturers are looking to advance on the market by developing next generation driving experience by tailoring the vehicle performance to the individual. The use of torque vectoring offers a substantial opportunity for tailoring the handling of the vehicle [13].

Despite the large volume of studies on electronic differential systems, there is currently no single accepted design method on how to significantly improve the handling and stability. The systems can be designed to either only work for emergency manoeuvres or running continuously [22]. The advantages with having a continuously running torques system is that there is potential of increasing stability during acceleration, braking and during external disturbances [21].

Various aspects of dynamic performance has been studied throughout literature, although many are focusing on the influence during various steering inputs. It has been straight running stability can be improved via optimal torque distribution of the in-wheel motors [15]. The implementation of direct yaw control has also been found to improve the vehicle stability when exposed to various load cases [40]. Additionally, it has the potential to counter act cross wind [41].

However, common for literature, such as the studies by [42], [40] and and [41] is that the results were extrapolated from simulations. Which provides a good indication of the controllers success, but is missing the physical validation.

2.4.1 Control Strategies

Direct yaw moment control is interchangeably referred to as torque vectoring when discussing individual-wheel motor torque allocation and the various control methods have extensively been investigated throughout literature [1, 6, 34]. These systems enables the designed to achieve steady state cornering by targeting a steady state yaw rate and sideslip reference [14, 34, 43–45].

The bicycle reference model is the most common method to estimate the vehicle states and is used to derive the vehicle steady state reference and used as the system model for the control design [14, 46]. This model require little computation and generates a noise-free sideslip [47]. However, as mentioned in [48], these type of linear reference models do not handle the change in vehicle parameters very well.

The hierarchical control layout approach is recurrent throughout literature and is commonly used for designing the systems [16, 21, 43]. These control layouts do not necessarily have identical structures, however in general there are three main levels of the control operations, which can be divided into: upper controller, lower controller and supervisory controller [49].

The role of the upper controller is to ensures that the stability control assume desired driving torque and yaw moment, which is then sent to the lower control [50]. Commonly the upper control consists of two blocks, which is the driver interpreter,and the closed-loop control law [49, 51]. The driver interpreter generates the driver intent based of steady-state cornering, whislt the closed-loop control is the control method chosen to generate the assistive yaw moment. The lower control, also known as toque allocator, uses the yaw moment command from the upper controller and distributes it as torque at the driving wheels [16, 51]. The observatory control is used to estimate the sideslip angle [47].

2.4.1.1 Closed-Loop Control

Extensive investigations have been made into DYC systems and numerous control approaches have been proposed, including PID configurations [8–11] sliding mode control (SMC) [12–15], model predicting control (MPC) [16,17].

The feedback portion of the controller is responsible for the correction of reference yaw rate and it is important that it is robust and smooth against changes in vehicle characteristics [21]. Although the layouts are rather alike, there are several different control strategies used for the design of the systems [6, 8, 16].

PID, PI and PD controllers have widely been used as a high level controller where the error between the desired values and actual values is used to control the yaw and sideslip. The controller adjusts the yaw moment as the input variables change [52]. In [53] it was suggested that a PID controller is more suited for real vehicle application due to the predictable behaviour, good frequency response and ease of implementation.

In [54] a PD controller was used to output the torque contribution, with the error of the tire slip difference between front and rear as the input. Unlike many other studies, the focus was on the wheelslip angles rather than the vehicle sideslip angle. In [55] a PID operation was used to output the torque contribution, with the use of error in yaw rate and a force calculated from the vehicle velocity. Similar for both these control methods is that the tire slip needs to be estimated and as mentioned by [47], the tire forces are also depend on the road friction, wear, pressure etc. which may cause error. PID control have also be used to attain the desired longitudinal speed and front-to-rear torque distribution [56].

Sliding Mode Control (SMC) or Sliding Surface Control (SSC), uses the tracking error between the reference and measured values to define a sliding surface which the control is forced to follow. The closed-loop stability condition can be defined by using Lyapunov stability theorem declare that as the system states are firstly attracted to the sliding surface, and then they will approache their desired steady-state references, i.e., the tracking error will approach to 0. The use of SMC has been found to be robust against uncertainties whilst not having exceedingly complex control laws [21, 57]. The drawbacks with this control strategy is the sometimes unsmooth response and chattering [57]. In [53] it was found that the SMC caused oscillations in the yaw rate at high steering amplitudes during step steer testing. In [57] it was proposed to combine a PID and slide surface controller, however the study focused on lap time and there was no evaluation of the controllers properties compared to a pure PID or sliding controller.

Optimal control methods, such as Linear Quadratic Regulators (LQR) and the Linear Quadratic Gaussian (LQG) controls, were previously a more common approach to control torque vectoring [8]. The LQR and LQG methods, control the driving/braking torque to provide more stability based on the reference model [8, 39]. The controller updates the reference model when the working conditions change, from estimates of the vehicle states. Even though it has been shown to improve the vehicle handling, the uncertainty that arise when estimating parameters are a concern when it comes to fast transient manoeuvres [8, 39]. In [39] it was noted that a the vehicle has to reduce its speed to maintain stability when using the LQR method, which would ultimately increase the energy consumption. Another drawback is that LQR controls are sensitive of change in parameters and towards influence of external disturbance, due to limited gain margins [58].

Model Predictive Control (MPC) is an optimised in-the-loop algorithm used as it provides an optimised solution [59]. It is a future predictive control, where at each sampling instant a new optimal plan is created. The control is based of the system model, which is also used to derive the prediction model and of course accoutns for the vehicles steady states. The prediction horizon, is the controllers ability to look ahead and take account of the present and future constraints when deriving a control policy. The ability of handling multi-variable system constraints is why this control strategy is popular [17]. There are various version of the MPC such as LTV-MPC and NMPC, both of which have showed success in controlling the lateral dynamics [17, 60] The major drawbacks with MPC methods are that they can be computationally heavy [60]. Additionally, since NMPC is an offline solution, this strategy requires external storage [17, 60].

Many torque vectoring systems integrate with other control systems to obtain the inputs to increase the stability of the vehicle [9, 19]. In [9] it was suggested to integrate between electric stability controller and a rear wheel active steering system to ensure vehicle stability. In [19] the path tracking controller of an autonomous vehicle was used to generate the reference yaw rate for their torque vectoring control. The reference yaw rates were pre-defined by look-up tables, which could then be selected to fit specific conditions. To ensure that the response is stable during unstable tire-road friction conditions, an additional reference yaw rate that is compatible with the existing condition has been defined

In [8] a real-time feedback system was proposed to be used during quick transient manoeuvres and a linear control system to be in use during steady state conditions. Compared to LQR controllers, yaw index controllers have been found to be more efficient at reducing the sideslip angle [39]. It has also been found that by introducing neuro-fuzzy estimator for the forces in the tires vertical direction, an estimation of the maximum grip can be attained. This has ultimately been able to provide a better match in yaw rate and has reduced the error by 33% [6].

Rule-based algorithms have become more popular since they can account for various driving conditions, however they require significant computing which can become a burden [61]. In fact, many of the recent studies use rather complex multivariable controllers, however literature suggest that simple PI-based control techniques with single-input and single-output are more efficient for the development of advanced torque vectoring. The motivation behind this is the simplicity of the low computational requirements and the predictable behaviour [19]. Although, a simulation study by [9] states that an integrated control systems between ESC and rear-wheel-active-steering has been found to withstand external interference during open-loop tests better than a vehicle with a more simple controller. The use of look-up tables is also another less complex control method since the output is predefined for given input signals [62]. As mentioned earlier, [19] utilised this method in their strategy. The drawbacks with this type of method is the limitation to specific predefined configurations and that memory storage is required [62].

2.4.1.2 Observatory Control

Most production vehicles with ESP generally are equipped with wheel speed sensors, gyroscope, Steering Angle Sensor (SAS) and accelerometers to obtain data required for vehicle dynamic analysis and control [48].The use of measured knowledge, has improved the handling of transient manoeuvres as the control action is directly decided from the movement of the vehicle [7, 8]. The drawbacks with directly measured information is the cost, reliability and accuracy [47].

In general one of the major issues with ESC is that not all the vehicle states can be directly measured [47]. As such, the major inadequacies with DYC systems is that the performance

is dependent on the accuracy of the estimation of sideslip [47, 63].The vehicle sideslip is not easily and inexpensively directly measured, hence literature shows the use of different types of observatory controllers, used to estimate sideslip [47, 64].

The two main methods to estimate vehicle sideslip is via model based observers or kinematic observers [26, 65]. The model based observer is derived from the bicycle reference model and can include feedback error from measured signals which forms a closed loop observer [65, 66]. Since the model based observer rely on the reference model, this means the it rely on accurate and predefined parameters such as vehicle and the tyre-road behaviour [65]. The common problem for an adequate estimation of sideslip angle is the non-linearity of the tires [47]. Large changes between pre-programmed values and a vehicles physical parameters can be the cause of estimation errors [27], which commonly occurs due to a changes in vehicle loading conditions as presented earlier. The kinematic observer on the other hand is based of the relationship between measurable signals, which makes it independent from knowledge of these parameters [26, 65].

These methods use different variations and combinations of Kalman filters [11, 47, 67], Fuzzy logic [6] or neural networks [68].

The methods which are using Kalman filters, also require the tire-road friction information as they rely on the tire model [69]. The use of unscented Kalman filtering require prior knowledge of the noise statistics of the measurement and process [47]. This means that excellent results may be obtained for post-processing, but does not necessarily reflect well on results in real-time if the conditions have changed (e.g. tire-road friction due to change in weather).

A Fuzzy PID controller was designed by [15], in which the fuzzy controller generate the target yaw moment to minimize the error feed into the PID. Similar combination was designed by [52], where the PID control was used for the error yaw rate since it can directly be measured and the fuzzy logic was used for the estimation of sideslip. Fuzzy networks, Adaptive Neuro-Fuzzy Interference system was found to provide a smaller estimation error than Neutral networks and Kalman filtering [47]. In [6] it was proposed to combine neuro-fuzzy and fuzzy, which provided a better match to the reference yaw rate.

In [64, 70], the concept of using Dynamic Curvature Control (DCC) for DYC systems was introduced to eliminate the need for estimation of sideslip during physical testing since it uses directly measurable variables. This is generally considered to be more cost effective than other sensor based techniques, and has better precision than what is achieved using various model based observers. The DCC, leverages the same relationship as established for kinematic based observers [65, 70]

2.4.1.3 Low Level Control

The low level control methods are fairly straight forward, depending on the vehicle layout the torque distribution is achieved differently. In-wheel motors can be modelled as a first order transfer function [55]. The wheels output torque is a combination between the maximum limit of the motor, the demanded torque from the driver and the torque contribution from the upper controller [54]. The wheel torque allocation is then simply extrapolated from the force at the corresponding driving wheels [55]. In [7] torque relationship between the different side wheels of the vehicle was assumed. In [56] a PID control was used to adjust front to rear torque distribution and a sliding mode controller to tune the left to right distribution on a four-wheel-drive vehicle.

The relationship between wheel force and total torque is often leveraged for torque allocation algorithms [71, 72]. For example [72], uses a dynamic load distribution ratio, which is calculated from the ratio of total vertical load to vertical loads at each wheel. This is fairly easy to obtain in a simulation environment; however, as pointed out by [71], the vertical forces of the tires require estimation during driving since there is no cost-effective way to measure them. Estimation of the vertical forces is formidable as is, and easily aggravated by uneven road, weight transfer and more importantly variation in mass and centre of gravity.

Chapter 3

Vehicle Dynamics

In this chapter the basic vehicle dynamics is presented in order to explain how the vehicle is affected by physics. The vehicle coordinate field is defined together with the common definitions used in dynamic studies, followed by the full vehicle simulation model, tyre model, reference model and the steady state handling definition.

3.1 Vehicle Dynamics Basics and Definition

In order to be able to study the vehicles behaviour it is important to be able to model the vehicles dynamics to understand and explain how physics affect the vehicle. Vehicle models are mathematical models which are derived from the vehicles equation of motion.There are many benefits with modelling and simulating a vehicles properties, such as the reduction of cost, time and risk.

For commercial vehicles the dynamic properties do not vastly vary and packaged software can be used to not only design but to validate vehicle models. In this thesis Siemens Simcenter Amesim^{TM} is employed to realise a 15-DOF model. Siemens Simcenter Amesim^{TM} is a software which allows for the study of a more complex vehicle model with further degrees of freedom and the involvement of the chassis, suspension and steering systems, without the computational burden.

3.1.1 Driver-in-the-Loop

The use of simulation to design, analyse and test vehicle systems prior physical manufacturing is an universal trend in the automotive engineering, however it is debatable how these system work with a real driver [73].

In vehicle dynamic studies, driver in the loop, reflecting the driver-vehicle interaction, plays an important role, particularly for the design of safety systems [74]. For a realistic response a validated real time driver model or ability for real driver inputs for steering and acceleration/braking is necessary. There are numerous methods presented in literature, such as in [75], where the driver model compose of proportional control with look-ahead and response delay behaviour. Or in [73] where a driver model using a fuzzy logic was presented.

The use of a driver-in-the-loop, also known as human-in-the-loop allows for the use of a real driver who interacts with the vehicle in a simulator setting or the real vehicle. In the reviewed literature in Chapter 2, the mentioning of the type of diver model used for research into direct yaw moment control was not consistently raised or what the impact could be if real human interaction was provided.

In this thesis an advanced driver model is not considered, instead, the simulation studies employ an open-loop driver, meaning that the velocity remains a constant input and the steering angle is given as an input to reflect the vehicle maneuver, however does not consider any type of adjustment feedback. During real-time physical testing and actual driver is introduced to provide the real driver interaction and feedback whilst testing.

3.1.2 Vehicle Coordinate Field

For a systematic approach to vehicle modelling and for the derivation of the equations of motion a coordinate system is defined as per ISO 8855:2011 [76] as:

- The positive x is defined as the forward direction of the vehicle.
- The positive y is defined as to the left of the vehicle if looking from the top.

- The positive z direction is defined as the vertical upwards direction from the ground.

The rotational motion along these axes are defined as:

- Rotation around the $x - axis$ is defined as roll angle ϕ.
- Roation around the $y - axis$ is defined as pitch angle θ.
- Rotation around the $z - axis$ is defined as yaw angle ψ.

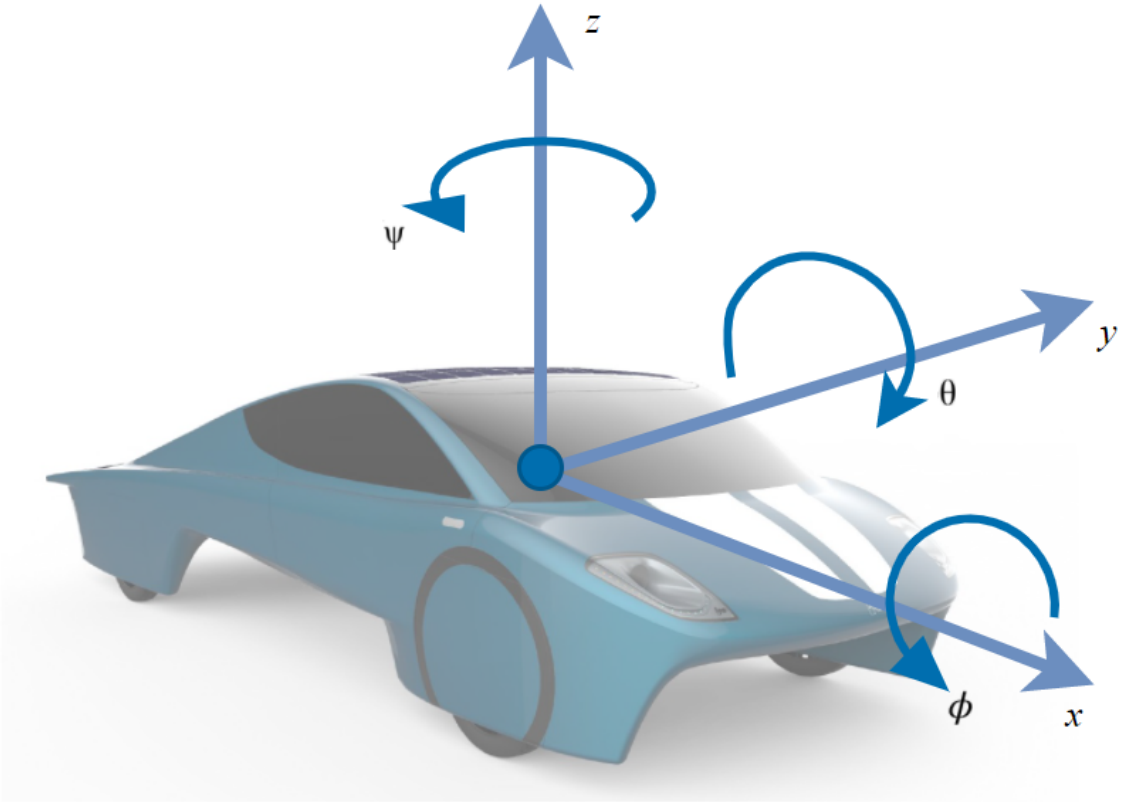

FIGURE 3.1: Vehicle coordinate field defenition. Adapted from graphics supplied by ATN Solar Car Project, 2019

3.2 Full Vehicle Model

Siemens Simcenter Amesim^{TM} was used to realise the vehicle model, by utilising the iCAR model application. The application environment allows for the use of predefined chassis subsystems which can be altered to accommodate vehicle specifications. In this research, a

15-DOF chassis model with steering, suspension, brakes, tyres and road components were used.

As per Figure 3.2, the chassis model accounts for:

- Displacement in the vertical, longitudinal and lateral direction.
- Pitch, yaw and roll angles of the sprung mass.
- The rotational and vertical displacement of the four wheels.
- The vertical movement of the steering rack.

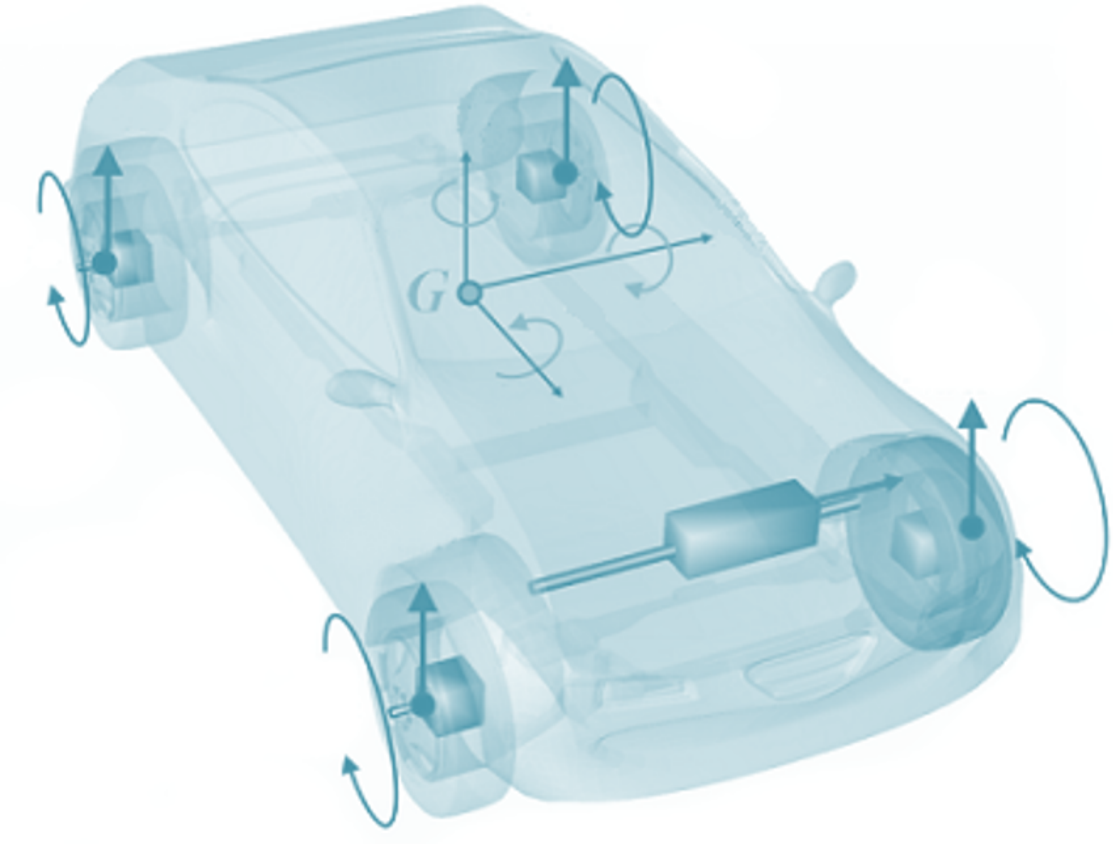

FIGURE 3.2: Siemens Simcenter Amesim^{TM} iCar model.

The Siemens Amesim^{TM} iCar model library includes a supercomponent for post processing as Figure 3.3. Inside the supercomponent, several sensors compues variables which are frequently used in vehicle dynamics. This include the vehicle sideslip angle at center of

gravity, front axle and rear axle; yaw, pitch and roll angles; yaw, pitch and roll velocities; yaw, pitch and roll accelerations; lateral, longitudinal and vertical accelerations etc.

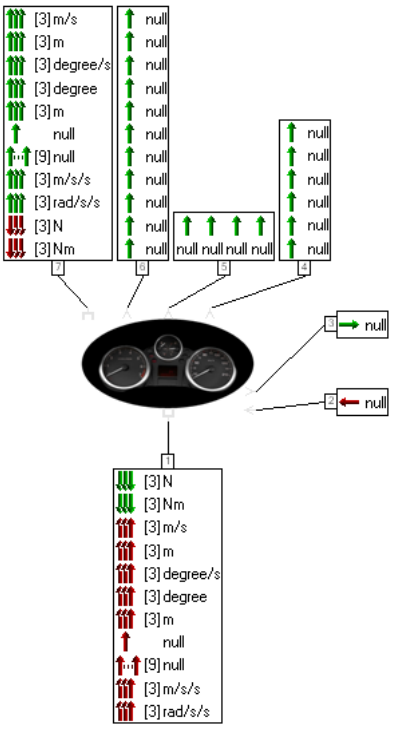

FIGURE 3.3: Siemens Amesim^{TM} post processing supercomponent

3.3 Tyre Model

The vehicle motions are largely affected by the forces generated between the tyres and road. The tyre modelling is an essential part of the mathematical model and must produce realistic forces whilst braking, accelerating, cornering, and combinations, on various road surfaces. There are several types of tyre models with different levels of accuracy and complexity, which can be expressed as a range from physical to empirical models [77]. The tyre models are generally selected and developed depending on the application of the vehicle simulation [78].

The physical models describe the mechanical characteristics of a tyre by mathematical expressions of the physical structure and the working mechanism of the tyre, such as Fiala [79] and, Gim and Dugoff [80].

Unlike the physical models, which use a theoretical approach, the empirical tyre models are established using experimental data. Semi-empirical models are tyre models which require measurements for parameterisation. These models have higher precision as they use a theoretical model and experimental data [81]. The Magic Formula (MF) tyre model is based on extensive experimental testing , as first described by Pacejka in [82], and then frequently used in literature [4, 21, 31, 43]. The Magic Formula Tyre model is a semi-empirical a model, since it is based on the tyres physical prototype and the measured data. Due to the wide application in industry and literature, as well as the available validated software models, this research employs the Magic Formula.

3.3.1 Tyre Forces and Coordinate System

The standard tyre axis system contains three forces and three moments, known as the tyre six-component wheel forces [83]. As per [78] these can be summarised as:

- F_x is the longitudinal tractive/breaking force
- F_y is the lateral cornering force
- F_z is the vertical/normal force
- M_z is the aligning moment
- M_x the overturning moment
- M_y the rolling resistance.

The Magic Formula can be used to describe these six-directional wheel forces in the steady state [81].

3.3.2 The Magic Formula Tyre Model

The Magic Formula was employed in Simcenter Amesim^{TM} to realise the tyre properties. The software deploys the tyre model that computes the lateral and longitudinal forces as well as X, Y and Z torques from the vertical load and slip coefficients.

The general Magic Formula was developed using mathematical functions that relate the lateral force and the aligning moment as functions of the tyre sideslip angle, and the longitudinal force as a function of the longitudinal slip [78]. The tyre slip angle is the angle between the direction the wheel is facing in relations to the direction the wheel is heading. Whilst the slip ratio of a wheel is used to quantify the proportion of slip/sliding in relations to the rolling movement of the wheel.

The general formula for pure slip described in [82] and [77], can be expressed:

$$Y(X) = D \sin\left[C \arctan\{Bx - E(Bx - \arctan\left(Bx\right))\}\right] \tag{3.1}$$

$$Y(X) = y(x + S_H) + S_V \tag{3.2}$$

$$x = X + S_H \tag{3.3}$$

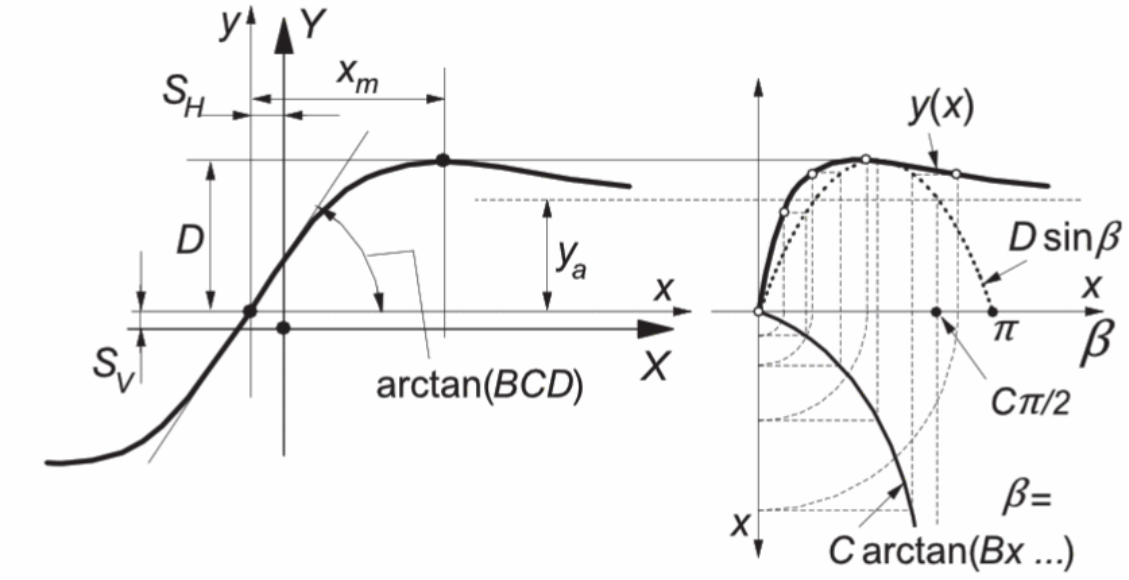

FIGURE 3.4: Interpretation of the MF curve parameters. Reprinted from Tyre and Vehicle Dynamics, Ed 3, Pacejka H., Semi-Empirical Tyre Models, pg.166 Copyright 2012, with permission from Elsevier.

Whereas the horizontal and vertical shift is described by S_H and S_V. Peak factor D, shape factor C, stiffness factor B and curvature factor E are described in **Figure 3** and

as follows:

$$D = y_m ax \tag{3.4}$$

$$C = \frac{2}{\pi} \arcsin \frac{y_s}{D} \tag{3.5}$$

$$B = \frac{\frac{dy}{dx}|_{x=0}}{CD} \tag{3.6}$$

$$E = \frac{Bx_n - \tan \frac{\pi}{2C}}{Bx_n - \arctan Bx_n} \tag{3.7}$$

Whereas the product of B, C and D correlates to the tyre corning stiffness $C_{y\alpha}$ for small tyre slip angles, as per:

$$BCD = C_{y\alpha} = \frac{\partial F_y}{\partial \alpha} \tag{3.8}$$

The complete expansion of the MF can be found in [82]. Due to the lack of tyre information, the default tyre data in Siemens Amesim$^{\mathrm{TM}}$ was used in for Chapter 6.

3.4 Reference Model

The bicycle model, also known as the single track model, is commonly used as a reference model for control analysis and design [15, 31, 32, 43, 46, 64, 84–89]. As per Figure 3.5, this is a linearised 2-DOF model of a vehicle which work under the following assumptions: (i) neglect the lift, rolling and pitching motions; (ii) it is a rigid body moving along a flat surface; (iii) the tyres forces operating within the linear region (iv) mass is concentrated at the centre of gravity and; (vi) the vehicle's wheels have been lumped into a single track along the centre line of the vehicle [32, 46, 89].

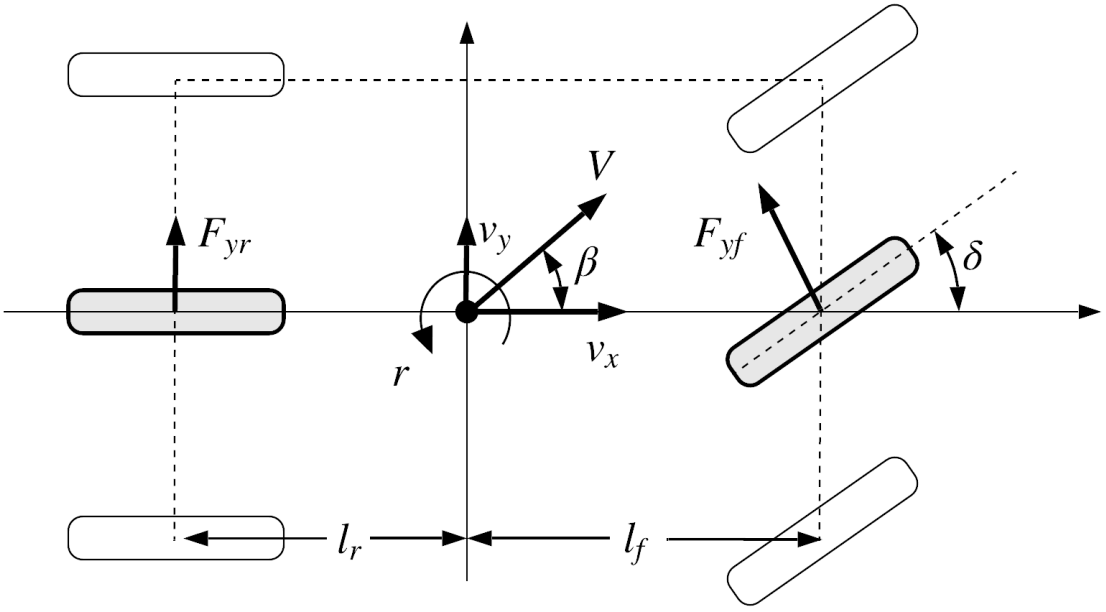

FIGURE 3.5: Vehicle reference model.

For a vehicle of mass m, moment of inertia I_z, lateral and longitudinal velocity v_x and v_y, yaw rate r, the equations of motion can be described as following:

$$m(\dot{v}_x - v_y r) = \sum F_x \tag{3.9}$$

$$m(\dot{v}_y + v_x r) = \sum F_y \tag{3.10}$$

$$I_z \dot{r} = M_Z \tag{3.11}$$

In which $F_{x/y}$ considers the sum of front and rear longitudinal/lateral forces.However, by assuming constant longitudinal velocity during the steering manoeuvre, the single track vehicle model is operating under the assumption of zero longitudinal forces, hence F_x can be neglected [32, 46]. In such the yaw moment M_z can be described as:

$$I_z \dot{r} = l_f \sum F_{yf} + l_r \sum F_{yr}. \tag{3.12}$$

Since there is no steering at the rear wheels, only the front wheel steering angle δ is considered. Assuming small tyre slip angles, then lateral tyre forces F_{yf} and F_{yr} can be described through linear approximation as:

$$\sum F_{yf} = -C_f(\beta + \frac{rl_f}{v_x} - \delta) \tag{3.13}$$

$$\sum F_{yr} = -C_r(\beta - \frac{rl_r}{v_x}). \tag{3.14}$$

Whereas rather than using $C_{y\alpha}$, C_f and C_r refers to the front and rear corner stiffness as described (3.8). Substituting Equations 3.13 and 3.14 in to Equations 3.11 and 3.12, equations of motion can be expressed as:

$$m(\dot{v}_y + v_x r) = \frac{(l_f C_f - l_r C_r)r}{v_x} - (C_f + C_r)\beta + C_f\delta \tag{3.15}$$

$$I_z\dot{r} = \frac{(l_f^2 C_f - l_r^2 C_r)r}{v_x} - (l_f C_f + l_r C_r)\beta + l_f C_f\delta. \tag{3.16}$$

3.4.1 Vehicle Steering Behaviour

A vehicles steering response depends on the vehicles design characteristics and velocity; at the limit of friction its behaviour can be defined by an understeering gradient. The understeering gradient is a fundamental concept which governs a vehicles handling. The equation leverage that the steering angle required to navigate a given curve is dependant on the vehicles longitudinal speed and design parameters of wheelbase, weight distribution and tire cornering stiffens.

Quasi-static cornering refers to when vehicle is traveling at a low enough speed for the front and rear slip angles to be small enough to be neglected. This means the radius (R) during cornering is given by a ratio based of the vehicles wheelbase (l) and steering angle input(δ), known as Ackermann geometry.

The understeering gradient K_s is essentially the difference between the Ackermann steer angle and the measured steer angle gradient [90].

$$R = \frac{l}{\delta}. \tag{3.17}$$

The Ackerman geometry declare that for any given velocity, the cornering radius would then remain the same [23]. However, as velocity is increased lateral forces are developed and slip angles at front and rear tyres can no longer be neglected. Whilst in the tyres linear region the relationship between the lateral force and slip angle can be expressed as:

$$F_{yf} = -C_f \alpha_f \tag{3.18}$$

$$F_{yr} = -C_r \alpha_r. \tag{3.19}$$

And as the tyres are still in the linear region the steering angle from (3.17) can be expressed as [46]:

$$\delta = \frac{l}{R} + \alpha_f - \alpha_r \tag{3.20}$$

Assuming there are two wheels at the front and rear, as well as small slip angles at each tire so that the lateral forces are proportional to its slip as in [91], it can be expressed that:

$$\alpha_f = \frac{F_{yf}}{2C_f} = \frac{m_f v_x^2}{2C_f R} \tag{3.21}$$

and

$$\alpha_r = \frac{F_{yr}}{2C_r} = \frac{m_r v_x^2}{2C_r R} \tag{3.22}$$

(3.20) can now be described as:

$$\delta = \frac{l}{R} + (\frac{m_f}{2C_f} - \frac{m_r v_x}{2C_r})\frac{v^2}{R} \tag{3.23}$$

where

$$\frac{v^2}{R} = a_y \tag{3.24}$$

As the stability factor (K_s) is the relationship of the slip angles at the front and rear tyres, (3.23) can be expressed as:

$$\delta = \frac{l}{R} + K_s a_y \tag{3.25}$$

In which, if K_s can be written in terms of total mass and location of CoG as in [91, 92] as:

$$K_s = \frac{m(l_r C_r - l_f C_f)}{2l^2 C_f C_r} \tag{3.26}$$

From (3.26), the steering behaviour can be evaluated and discussed follows:

Neutral steer: $K_s = 0$, as the slip angles of the tires at front and rear are equal. This means a vehicle can remain at a constant radius without adjusting the steering angle when increasing longitudinal velocity. This relationship also indicates a linear yaw rate gain as longitudinal velocity increase.

Under-steering behaviour: $K_s > 0$, as the slip angle at the front tire is greater than the rear, meaning the steering angle needs to be increased in order for the vehicle to remain at a constant set radius as velocity is increased. At low velocities an under-steered vehicle may still remain in a steady state, meaning no compensation is required. With an increase in longitudinal velocity the vehicles yaw rate gain will increase at a lower rate than a neutral steered vehicle. This results in insufficient yawing motion which is the cause of the vehicle not steering enough, unless compensated for by changing the steering angle.

Over-steering behaviour:$K_s < 0$, as the front tire slip angle is lower compared to the rear, meaning the steering angle needs to be decreased in order for a vehicle to remain at a constant set radius as velocity is increased. Similar to the under-steered behaviour, at low velocities the vehicle may remain in a steady state. As velocity is increased, so does the yaw rate gain, and in comparison to neutral steer, at a much higher rate. A vehicle with over-steering behaviour will eventually reach a critical speed, which is the velocity where the decrease in steering angle still cannot keep the path and the vehicle becomes unstable [92]

In real vehicles the critical speed is usually much lower than predicted by the single track model as there are additional degrees of freedom, unless driving in a straight [90]. Due to solar cars design properties and sensitivity to additional weight, as well as limited information of the tyres, critical speed is not considered as a measure for stability. However, the steering behaviour will be used to derive desired handling from the linear model to define the lateral control problem.

3.4.2 Desired Handling

In order to maintain the lateral stability of the vehicle, the vehicles steering behaviour is leveraged to determine the desired sideslip angle β_d and desired yaw rate r_d. Steady-state handling, also known at steady-state cornering is defined as circular trajectory with constant radius is maintained during constant velocity and steering angle [93].From steady-state handling of the reference model (3.15) and (3.16), and with limitation of the tyre friction the desired yaw rate can be expressed as in [84] as:

$$r_d = \begin{cases} r_t, & |r_d| < \frac{0.85\mu g}{v_x} \\ \frac{0.85\mu g}{v_x} sign(r_t), & |r_d| \geqslant \frac{0.85\mu g}{v_x} \end{cases} \tag{3.27}$$

whereas r_t is expressed using the under steering gradient (3.26) as:

$$r_t = \frac{v_x \delta}{l(1 + K_s v_x^2)} \tag{3.28}$$

In theory a vehicle can experience a lateral acceleration of gravity times maximum friction at the tires. If the friction co-efficient is equal to one, the lateral acceleration could be 9.81 m/s^2 with a sideslip angle of zero. The reference value for sideslip can be considered similar to yaw rate to be limited by the availability of friction as presented in [84, 94]. Due to the design properties of the solar car it was chosen to consider the desired sideslip as:

$$\beta_d = 0 \tag{3.29}$$

Chapter 4

Control Design

In this chapter, the yaw moment control structure and design is presented.

4.1 Overview

The yaw moment control system has a hierarchical structure and uses a reference model which follows the vehicles steady state cornering dynamic response, as derived in 3.

As described in [51], there are three major logical blocks that commonly accomplish the complete control system action when using a model reference approach. Figure 4.1 presents a block diagram of the control structure used in this research.

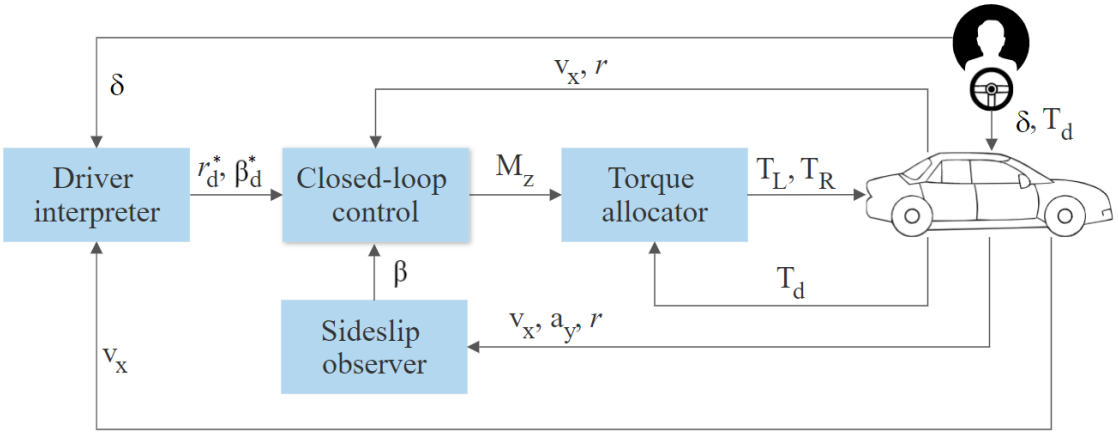

FIGURE 4.1: Block diagram of the yaw control structure.

1. **Driver interpreter**: generates the yaw rate reference $r_d^\star$ based on the vehicle velocity, v_x, and steering angle, δ, imposed by driver. The full details and assumptions of the reference bicycle model were presented in Chapter 3, Section 3.4.

2. **Closed-loop control**: designed by using the system dynamic model. In this thesis, the use of four different control strategies is investigated; Proportional Integral (PI) in 4.3, DCC in 4.4, MPC in 4.6, and SMC (in Chapter 4.5).

3. **Torque allocation**: assigns the assisting torque T_L and T_R to each motor. This is derived from the yaw moment control action.

4.2 System Model

The reference model presented in Chapter 3, Section 3.4, is commonly used as system model for a yaw rate control design. Implementing the corrective yaw moment M_z and considering four wheels, (3.16) can be expressed as:

$$I_z\dot{r} = \frac{2r(l_f^2C_f - l_r^2C_r)}{v_x} - 2\beta(l_fC_f + l_rC_r) + 2l_fC_f\delta + M_z. \tag{4.1}$$

Whereas the rate of change in the sideslip, $\dot{\beta}$, can be obtained from the steady state dynamic curvature as further explained in Chapter 6, as per (6.13a).

Base on this, in order to derived a continuous-time dynamic state-space system model for the reference model, we can define the system state and control input as:

$$\boldsymbol{x}(t) = \begin{bmatrix} \beta(t) \\ r(t) \end{bmatrix}, \; u(t) = M_z(t), \tag{4.2}$$

which leads to the following expression:

$$\dot{\boldsymbol{x}}(t) = \boldsymbol{A}_c\boldsymbol{x}(t) + \boldsymbol{B}_cu(t) + \boldsymbol{d}(t), \tag{4.3}$$

where

$$\boldsymbol{A}_c = \begin{bmatrix} -\frac{2(C_f+C_r)}{mv_x} & -\frac{2(l_fC_f-l_rC_r)}{mv_x^2} - 1 \\ -\frac{2(l_fC_f-l_rC_r)}{I_z} & -\frac{2(l_f^2C_f-l_r^2C_r)}{I_zv_x} \end{bmatrix}, \; \boldsymbol{B}_c = \begin{bmatrix} 0 \\ 1 \end{bmatrix} \tag{4.4}$$

It is important to emphasise that from a control viewpoint $\boldsymbol{d}(t)$ is a known input disturbance vector for (4.3), which is represented by:

$$\boldsymbol{d}(t) = \boldsymbol{E}_c \delta_f(t) \tag{4.5}$$

where

$$\boldsymbol{E}_c = \begin{bmatrix} \frac{2C_f}{mv_x} \\ \frac{2l_f C_f}{l_z} \end{bmatrix}. \tag{4.6}$$

Now, considering a forward Euler approximation, the following discrete time dynamic model can be derived:

$$\boldsymbol{x}(k+1) = \boldsymbol{A}\boldsymbol{x}(k) + \boldsymbol{B}u(k) + \boldsymbol{d}(k) \tag{4.7}$$

where

$$\boldsymbol{A} = \boldsymbol{I} + t_s \boldsymbol{A}_c, \ \boldsymbol{B} = t_s \boldsymbol{B}_c, \tag{4.8}$$

in which t_s is the sampling time.

4.3 Proportional-Integral Control

The use of Proportional-Integral-Derivative control (PID) configurations for systems has been well investigated as it is effective and carries a low computational burden [15, 19, 64]. The justification of using a PI configuration, rather than P, PD or PID was evaluated via simulation. Similar to [95], sideslip and yaw will be adjusted as follows:

$$\Delta M_{zr} = K_p^r e_r(t) + K_i^r \int_t^0 e_r(t)dt \tag{4.9}$$

$$\Delta M_{z\beta} = K_p^\beta e_\beta(t) + K_i^\beta \int_t^0 e_\beta(t)dt \tag{4.10}$$

In which the error for yaw rate $e_r(t)$ and sideslip $e_\beta(t)$ is:

$$e_r(t) = r_d(t) - r(t) \tag{4.11}$$

$$e_\beta(t) = r_\beta(t) - \beta(t) \tag{4.12}$$

The assistive yaw moment M_{zc} can then be described as the sum of (4.11) and (4.12) as:

$$\Delta M_{zc} = \Delta M_{zr} + \Delta M_{z\beta} \tag{4.13}$$

4.4 Dynamic Curvature Control

In [64, 70, 96], the dynamic curvature was introduced as a control variable. From the steady-state of the reference model, the curvature of a vehicles driving path for neutralsteer can be described as:

$$\frac{1}{R} = \frac{\delta}{L + mv_x^2(\frac{l_r C_r - l_f C_f}{2C_f C_r L})} \tag{4.14}$$

where R is the radius of the vehicles cornering path. As per [70], the dynamic curvature variable denoted as k can be expressed as:

$$k = \frac{\dot{\beta} + r}{v_x} \tag{4.15}$$

The use of $k(t)$ allows for the use of the instantaneous curvature at any time during manoeuvring. However, the drawbacks as described in [64] is the potential error due to the curvature being derived from the steady state model as well as the fact that the cornering stiffness of the tires have been linearized and approximated. To generate the assistive yaw moment, M_{zc}, the mathematical expression for the PI controller is described as:

$$\Delta M_{zc} = K_p^k e_k(t) + K_i^k \int_t^0 e_k(t)dt \tag{4.16}$$

whereas the error $e_k(t)$ can be expressed as:

$$e_k(t) = k_d(t) - r(t) \tag{4.17}$$

while k_d can be described in terms of (4.15), from the desired yaw rate in (3.27) and desired sideslip in (3.29) as:

$$k_d = \frac{\dot{\beta}_d + r_d}{v_x} \tag{4.18}$$

4.5 Sliding Mode Control

In a sliding mode control formulation, a sliding surface is firstly defined. In this case, it is chosen as follows:

$$s = e_1 + \lambda e_2 \tag{4.19}$$

where, e_1 is the yaw rate tracking error and e_2 is the sideslip angle tracking error. Moreover, λ is a positive real constant, i.e., $\lambda > 0$.

The desired yaw rate and sideslip angle are described in Chapter 3. In such, the tracking error of yaw rate is expressed as:

$$e_1 = r - r_d \tag{4.20}$$

Since $\beta_d = 0$, the tracking error for the sideslip angle is simply:

$$e_2 = \beta \tag{4.21}$$

This leads to the following sliding surface for the yaw rate control:

$$s = r - r_d + \lambda\beta \tag{4.22}$$

Now, a suitable candidate Lyapunov function for this problem can be the following standard quadratic function:

$$V = \frac{1}{2}s^2 \tag{4.23}$$

It is important to emphasize that whenever the tracking errors, e_1 and e_2, are not zero, V in (4.23) will take a positive value larger than zero, i.e., $V > 0$ for all $e_1, e_2 \neq 0$. Moreover, $V = 0$ only if $e_1 = e_2 = 0$. Consequently, leading the tracking errors to zero is equivalent to lead the Lyapunov function to zero, i.e, if $V \to 0$ then, $e_1 \to 0$ and $e_2 \to 0$. This can be achieved by forcing the derivative of the Lyapunov function to be negative whenever the tracking errors are not zero, i.e., $\dot{V} < 0$ for all $e_1, e_2 \neq 0$.

Based on the above discussion, it is convenient to introduce the Lyapunov function derivative, which is expressed as follows:

$$\dot{V} = s\dot{s} \tag{4.24}$$

Now, it is proposed to chose the surface derivative as follows:

$$\dot{s} = \dot{e}_1 - \lambda\dot{e}_2 = \dot{r} - \dot{r}_d + \lambda\dot{\beta} = -\hat{K}\text{sign}(s) \tag{4.25}$$

where $\hat{K} > 0$ is the controller gain. This leads to:

$$\dot{V} = s\dot{s} = s \cdot (-\hat{K}\text{sign}(s)) = -\hat{K} \cdot s \cdot \text{sign}(s) \tag{4.26}$$

Then, since $s \cdot \text{sign}(s) = |s|$, it follows that:

$$\dot{V} = s\dot{s} = -\hat{K}|s| \tag{4.27}$$

which clearly ensures the convergence of the Lypunov function to zero. This is formally known as Lypunov stability criteria for a sliding mode controller.

Finally, to satisfy the Lypunov stability criteria, the control input needs to be selected in order to satisfy (4.25). To ensure this even in the presence of uncertainties, it is possible to express

$$\dot{\beta} = f_1 + \Delta f_1 \tag{4.28}$$

and

$$\dot{r} = f_2 + \Delta f_2 + M_Z u(t) \tag{4.29}$$

in which Δf_1 and Δf_2 are representing uncertainty. Whilst f_1 and $f2$ are the corresponding rows from the state-space equation (4.3)-(4.4), which is:

$$f_1 = -\frac{C_f + C_r}{mv_x}\beta - \frac{l_f C_f - l_r C_R}{mv_x^2} - 1 - \frac{C_f}{mv_x}\delta_f \tag{4.30}$$

$$f_2 = -\frac{l_f C_f - l_r^2 C_r}{I_z v_x}\beta - \left(-\frac{l_f^2 C_f + l_r^2 C_r}{I_z v_x} r\right) - \frac{l_f C_f}{I_z}\delta_f \tag{4.31}$$

Substituting f_1 and f_2 into the sliding surface derivative as follows:

$$f_2 + \Delta f_2 + \mathbf{U(t)} \ - \dot{r}_d + \lambda(f_1 + \Delta f_1) = -\hat{K} sign(s) \tag{4.32}$$

Rearranging (4.32), the control input can be expressed as:

$$U(t) = +\dot{r}_d - f_2 - \Delta f_2 - \lambda(f_1 + \Delta f_1) - \hat{K} sign(s) \tag{4.33}$$

In [96] the uncertainties $\Delta f_1 \geq 0$ and $\Delta f_2 \geq 0$ were considered as the maximum change in mass and inertia. A zero uncertainty scenario was also considered to investigate the difference in robustness, in this case the control input can be simplified to:

$$U(t) = +\dot{r}_d - f_2 - \lambda f_1 - \hat{K} sign(s) \tag{4.34}$$

Afterwards, the Lyapunov stability criteria is verified to consider these maximum uncertainties. From (4.26), it follows that:

$$\dot{V} = s(\dot{r} - \dot{r}_d + \lambda\dot{\beta}) = s(\Delta f_2 + \lambda\Delta f_1 - \hat{K}\text{sign}(s)) \tag{4.35}$$

If $s < 0$, it implies that $\text{sign}(s) = -1$. This leads to $\dot{V} = s(\Delta f_2 + \lambda\Delta f_1 + \hat{K})$. Since $\Delta f_1, \Delta f_2, \hat{K} \geq 0$, it implies that $\dot{V} < 0$. Conversely, for the case when $s > 0$, it implies that $\text{sign}(s) = 1$. This leads to $\dot{V} = s(\Delta f_2 + \lambda\Delta f_1 - \hat{K})$. Clearly, this imposes a lower positive limit for $\hat{K}$ given by $\hat{K} > \Delta f_2 + \lambda\Delta f_1$ in order to ensure that $\dot{V} < 0$. Moreover, the bandwidth of the controller is directly related to the gain $\hat{K}$, which can be increased to achieve a faster closed-loop dynamic. However, this cannot be increased indefinitely since it will translate in a large control action, i.e., a large torque of the motors in this case. Therefore, the gain $\hat{K}$ can be practically tuned to satisfy the torque limitations of the motors while satisfying the Lyapunov stability criteria.

4.6 Model Predictive Control

4.6.1 Optimal Control Problem

AS previuosly mentioned, the control target for this system is to track the system state references, $\boldsymbol{x}^\star = \begin{bmatrix}\beta^\star & r^\star\end{bmatrix}^{\mathrm{T}}$. To achieve this, the MPC strategy is formulated considering the following quadratic cost function that evaluates the tracking error over a finite prediction horizon N, i.e.:

$$V_N = \sum_{\ell=k}^{k+N-1} \boldsymbol{x}_{\mathrm{e}}^{\mathrm{T}}(\ell+1)\boldsymbol{Q}\boldsymbol{x}_{\mathrm{e}}(\ell+1) + \sigma\Delta u^2(\ell) \tag{4.36}$$

where $\boldsymbol{x}_e(k) = \boldsymbol{x}(k) - \boldsymbol{x}^\star$ is the system state tracking error and $\Delta u(k) = u(k) - u(k-1)$ is the, so-called, control effort given by the rate change of the yaw moment. Moreover,

$$\boldsymbol{Q} = \mathrm{diag}(q_1, q_2) \tag{4.37}$$

is the diagonal state weighting matrix, in which $q_1, q_2 \geq 0$ are the individual weighting factors associated to each system state. This allows one to give more or lees importance to the control of the yaw rate versus sideslip angle. Finally, the scalar $\sigma > 0$ is the control weighting factor that allows one to trade system state tracking errors versus a control input effort. In this way, the MPC strategy seeks to obtain an input control sequence

$$\boldsymbol{U}(k) = \begin{bmatrix}u(k) & u(k+1) & \cdots & u(k+N-1)\end{bmatrix}^{\mathrm{T}} \tag{4.38}$$

that minimizes the cost function (4.36) over a prediction horizon N. Importantly, to forecast the future system behavior, the discrete-time system model (4.7) must be used, which considers the known input disturbance $\bar{\boldsymbol{d}} = \boldsymbol{d}(k)$ as persistent over the whole prediction horizon. This will lead to the following future system state predictions:

$$\boldsymbol{X}_{[1:N]} = \begin{bmatrix}\boldsymbol{x}^{\mathrm{T}}(k+1) & \cdots & \boldsymbol{x}^{\mathrm{T}}(k+N)\end{bmatrix}^{\mathrm{T}}. \tag{4.39}$$

Moreover, since the value that the yaw moment can adopt is physically limited by the torque of the motors, it is required to constraint the system control input along the whole

prediction horizon. Consequently, in a formal manner, the MPC strategy can be formulated as the following optimal control problem:

$$\boldsymbol{U}_{\text{opt}}(k) = \arg \min_{\boldsymbol{U}(k)} V_N(\boldsymbol{x}(k), \boldsymbol{U}(k)) \tag{4.40a}$$

$$\text{subject to: } \boldsymbol{x}(\ell+1) = \boldsymbol{A}\boldsymbol{x}(\ell) + \boldsymbol{B}u(\ell) + \bar{\boldsymbol{d}} \tag{4.40b}$$

$$u_{\min} \leq u(\ell) \leq u_{\max}, \forall \ell \in \{k, k+N-1\} \tag{4.40c}$$

The solution of the optimal control problem in (4.40) leads to the following optimal input vector:

$$\boldsymbol{U}_{\text{opt}}(k) = \begin{bmatrix} u_{\text{opt}}(k) & u_{\text{opt}}(k+1) & \cdots & u_{opt}(k+N-1) \end{bmatrix}^{\text{T}}. \tag{4.41}$$

Finally, following the receding horizon policy, only the first element of the optimal input vector, $u_{\text{opt}}(k)$, is applied to the system, discarding the remaining future optimal inputs. This yields the following predictive closed-loop equation:

$$\boldsymbol{x}(k+1) = \boldsymbol{A}\boldsymbol{x}(k) + \boldsymbol{B}u_{\text{opt}}(k) + \bar{\boldsymbol{d}} \tag{4.42}$$

Then, this procedure is repeated at each sampling instant using fresh measurements of the system states, vehicle speed, and steering angle.

4.6.2 Prediction Model

For simplicity, let us consider that at a given sampling instant k, the system state is denoted as $\boldsymbol{x}(0) = \boldsymbol{x}(k)$. Then, by iterating (4.7), the future predictive values for the state vector represented by:

$$\boldsymbol{X}_{[1:N]} = \begin{bmatrix} \boldsymbol{x}^{\text{T}}(1) & \cdots & \boldsymbol{x}^{\text{T}}(N) \end{bmatrix}^{\text{T}} \tag{4.43}$$

can be obtained as follows:

$$\boldsymbol{X}_{[1:N]} = \boldsymbol{\Lambda}\boldsymbol{x}(0) + \boldsymbol{\Phi}\boldsymbol{U}(k) + \boldsymbol{\Gamma}\bar{\boldsymbol{d}} \tag{4.44}$$

where

$$\begin{aligned}
\boldsymbol{\Lambda} &= \begin{bmatrix} \boldsymbol{A} \\ \boldsymbol{A}^2 \\ \vdots \\ \boldsymbol{A}^N \end{bmatrix}, \boldsymbol{\Phi} = \begin{bmatrix} \boldsymbol{B} & \mathbf{0}_{n\times m} & \cdots & \mathbf{0}_{n\times m} & \mathbf{0}_{n\times m} \\ \boldsymbol{AB} & \boldsymbol{B} & \cdots & \mathbf{0}_{n\times m} & \mathbf{0}_{n\times m} \\ \vdots & \vdots & \ddots & \vdots & \vdots \\ \boldsymbol{A}^{N-1}\boldsymbol{B} & \boldsymbol{A}^{N-2}\boldsymbol{B} & \cdots & \boldsymbol{AB} & \boldsymbol{B} \end{bmatrix}, \\
\boldsymbol{\Gamma} &= \begin{bmatrix} \boldsymbol{I} \\ \boldsymbol{A}+\boldsymbol{I} \\ \vdots \\ \boldsymbol{A}^{N-1}+\boldsymbol{A}^{N-2}\cdots\boldsymbol{A}+\boldsymbol{I} \end{bmatrix}.
\end{aligned} \tag{4.45}$$

Thus, to predict the future system behaviour, it is only required to know the present value of the system states, $\boldsymbol{x}(0) = \boldsymbol{x}(k)$, input disturbance $\bar{\boldsymbol{d}} = \bar{\boldsymbol{d}}(k)$, and the sequence of tentative input actions, $\boldsymbol{U}(k)$, to be applied to the system.

4.6.3 Quadratic Cost Function

To evaluate the future system behaviours, the cost function (4.36) needs to be evaluated. In order to find the optimal control input sequence, it is convinient to rewrite this cost function in the following compact form:

$$\begin{aligned}
V_N = {} & \boldsymbol{X}_{e,[1:N]}^{\mathrm{T}} \boldsymbol{Q}_N \boldsymbol{X}_{e,[1:N]} \\
& + \sigma(\boldsymbol{SU}(k) - \boldsymbol{G}u(k-1))^{\mathrm{T}}(\boldsymbol{SU}(k) - \boldsymbol{G}u(k-1))
\end{aligned} \tag{4.46}$$

where

$$\boldsymbol{Q}_N = \mathrm{diag}\{\boldsymbol{Q}, \cdots, \boldsymbol{Q}\} \tag{4.47a}$$

$$\boldsymbol{S} = \begin{bmatrix} 1 & 0 & 0 & \cdots & 0 & 0 \\ -1 & 1 & 0 & \cdots & 0 & 0 \\ 0 & -1 & 1 & \cdots & 0 & 0 \\ \vdots & & & \ddots & & \\ 0 & 0 & 0 & \cdots & -1 & 1 \end{bmatrix}, \ \boldsymbol{G} = \begin{bmatrix} 1 \\ 0 \\ 0 \\ \vdots \\ 0 \end{bmatrix}. \tag{4.47b}$$

Now, based on the prediction model in (4.44), it is possible to rearrange this cost function in order to represent it only as a function of the control input sequence, $\boldsymbol{U}(k)$. Thus, it follows that:

$$\begin{aligned}
&\boldsymbol{X}_{e,[1:N]}^{\mathrm{T}}\boldsymbol{Q}_N\boldsymbol{X}_{e,[1:N]} \\
=&\Big(\boldsymbol{\Lambda x}(0)+\boldsymbol{\Gamma}\bar{\boldsymbol{d}}-\boldsymbol{X}_{[1:N]}^{\star}+\boldsymbol{\Phi U}(k)\Big)^{\mathrm{T}}\boldsymbol{Q}_N\Big(\boldsymbol{\Lambda x}(0)+\boldsymbol{\Gamma}\bar{\boldsymbol{d}}-\boldsymbol{X}_{[1:N]}^{\star}+\boldsymbol{\Phi U}(k)\Big) \\
=&\left(\boldsymbol{\Lambda x}(0)+\boldsymbol{\Gamma}\bar{\boldsymbol{d}}-\boldsymbol{X}_{[1:N]}^{\star}\right)^{\mathrm{T}}\boldsymbol{Q}_N\left(\boldsymbol{\Lambda x}(0)+\boldsymbol{\Gamma}\bar{\boldsymbol{d}}-\boldsymbol{X}_{[1:N]}^{\star}\right) \\
&+2\left(\boldsymbol{\Lambda x}(0)+\boldsymbol{\Gamma}\bar{\boldsymbol{d}}-\boldsymbol{X}_{[1:N]}^{\star}\right)^{\mathrm{T}}\boldsymbol{Q}_N\boldsymbol{\Phi U}(k)+\boldsymbol{U}^{\mathrm{T}}(k)\boldsymbol{\Phi}^{\mathrm{T}}\boldsymbol{Q}_N\boldsymbol{\Phi U}(k)
\end{aligned} \tag{4.48}$$

and

$$\begin{aligned}
&\sigma(\boldsymbol{SU}(k)-\boldsymbol{G}u(k-1))^{\mathrm{T}}(\boldsymbol{SU}(k)-\boldsymbol{G}u(k-1)) \\
&\qquad=\sigma u^2(k-1)-2\sigma u(k-1)\boldsymbol{G}^{\mathrm{T}}\boldsymbol{U}(k)+\sigma\boldsymbol{U}^{\mathrm{T}}(k)\boldsymbol{S}^{\mathrm{T}}\boldsymbol{SU}(k).
\end{aligned} \tag{4.49}$$

Then, this leads to the the following compact quadratic cost function:

$$V_N(\boldsymbol{x}(k),\boldsymbol{U}(k))=\nu+\boldsymbol{U}(k)^{\mathrm{T}}\boldsymbol{HU}(k)+2f^{\mathrm{T}}(k)\boldsymbol{U}(k) \tag{4.50}$$

where

$$\boldsymbol{H}=\boldsymbol{\Phi}^{\mathrm{T}}\boldsymbol{Q}_N\boldsymbol{\Phi}+\sigma\boldsymbol{S}^{\mathrm{T}}\boldsymbol{S} \tag{4.51a}$$

$$f(k)=\boldsymbol{\Phi}^{\mathrm{T}}\boldsymbol{Q}_N\left(\boldsymbol{\Lambda x}(k)+\boldsymbol{\Gamma}\bar{\boldsymbol{d}}-\boldsymbol{X}_{[1:N]}^{\star}\right)-\sigma\boldsymbol{G}u(k-1). \tag{4.51b}$$

Additionally, the term

$$\nu=\left(\boldsymbol{\Lambda x}(k)+\boldsymbol{\Gamma}\bar{\boldsymbol{d}}-\boldsymbol{X}_{[1:N]}^{\star}\right)^{\mathrm{T}}\boldsymbol{Q}_N\left(\boldsymbol{\Lambda x}(k)+\boldsymbol{\Gamma}\bar{\boldsymbol{d}}-\boldsymbol{X}_{[1:N]}^{\star}\right)+\sigma u^2(k-1)$$

does not depend on the input vector $\boldsymbol{U}(k)$. Therefore, it does not participate in the optimization.

Finally, the original optimal control problem in (4.40) can be transformed into the following equivalent optimal problem:

$$\boldsymbol{U}_{\text{opt}}(k) = \arg \min_{\boldsymbol{U}(k)} \boldsymbol{U}^{\text{T}}(k)\boldsymbol{H}\boldsymbol{U}(k) + 2f^{\text{T}}(k)\boldsymbol{U}(k) \tag{4.52a}$$

$$\text{subject to: } u_{\min}\boldsymbol{I}_N \leq \boldsymbol{U}(k) \leq u_{\max}\boldsymbol{I}_N \tag{4.52b}$$

where $\boldsymbol{I}_N$ stands for an $N \times N$ identity matrix.

This optimization is a convex optimal problem due to the quadratic cost function and linear constraints. Therefore, standard Quadratic Programming (QP) algorithms can be used to obtain $\boldsymbol{U}_{\text{opt}}(k)$, e.g., `quadprog()` in Matlab.

4.7 Torque Allocation

Literature has indicated that the use of advanced algorithms for torque allocation in simulated environments are more effective than standard ones. These algorithms are often based on entities that are easy to obtain in simulation, but difficult to directly measure them in reality. This is not coherent when considering an engineering application.

The relationship between wheel force and total torque is often leveraged for torque allocation algorithms [71, 72]. For example, [36] uses a dynamic load distribution ratio, which is calculated from the ratio of total vertical load to vertical loads at each wheel. The vertical forces are easily obtained in simulations and during static conditions, as in Chapter 6, Section 6.2. However, they require estimation during driving since there is no cost-effective way to measure them directly in a safe manner. Estimation of the vertical forces is formidable as is, and is easily aggravated by uneven roads, weight transfer and more importantly variation in mass and centre of gravity would be further cause transmittable error in real driving [71]. In [97], the vertical forces were estimated with great success. However, authors mentioned this is only effective when parameters are known and remain constant, which is not the case in reality. As a consequence, this research ignores the localised load transfer for torque allocation and the toque will be equally divided to each of the rear wheels. The rotational dynamic equations of the rear wheels can be expressed

as:

$$I_w\dot{\omega}_3 = T_3 - r_w F_{x_3} \tag{4.53}$$

$$I_w\dot{\omega}_4 = T_4 - r_w F_{x_4}. \tag{4.54}$$

The control input applies the assistive yaw moment, denoted M_{zc}, to the system. This is done by adjusting the torque of the individual motors. The relationship between the yaw moment and torque can be expressed in relations to the tire forces as:

$$M_{zc} = (F_{x_3} - F_{x_4})\frac{t_r}{2} = \Delta F\frac{t_r}{2} = \frac{\Delta T t_r}{2r_w} = \frac{2Tt_r}{2r_w} = \frac{Tt_r}{r_w} \tag{4.55}$$

Rearranging (4.55), then the total torque input from the controls can be described as:

$$T = \frac{M_{zc}r_w}{t_r}. \tag{4.56}$$

When distributed to the rear wheels:

$$T_3 = \frac{T_{driver}}{2} + T \tag{4.57}$$

$$T_4 = \frac{T_{driver}}{2} - T. \tag{4.58}$$

Chapter 5

Simulation

This chapter presents the early stage investigations of the ATN solar cars dynamic properties and its parameters in a simplified simulation environment using MATLAB, followed by control verification by simulation and real-time simulation using Siemens Simcenter Amesim.

In the early stages of this research, the ATN solar car design was incomplete and does not correlate with the final design. As such, depending on which stage in the design or build phase of the real vehicle, the simulation studies use estimations of the parameters evaluated at that point in time. Each study indicate which parameters were used for ease of correlation.

5.1 Vehicle Comparison

To get a general idea how much the solar car differ compared to an average vehicle a comparison between vehicle parameters and estimations of the solar car were evaluated. In the first section, the PI controller presented in Chapter 4, Section 4.3 was applied to a simple vehicle model, and in the second section the PI control and the dynamic curvature control presented in Chapter 4, Section 4.4.

The two studies presented in this section use different vehicle parameters, due to the change in the solar car design at this point in time and the availability of software.

5.1.1 Simple Vehicle Model: PI Control

This study was performed prior to licensing was issued for Siemens Amesim^{TM} and uses a simple vehicle model in Appendix A. In this first study vehicle parameters from [98] were used as the general vehicle as per Table 5.1

TABLE 5.1: Vehicle parameters used in an early simulation study of comparison between a general sized vehicle and the ATN solar car.

Description	Symbol	General vehicle	ATN solar car	Unit
Mass	m	1298.9	465	Kg
Wheelbase	L	2.454	3	m
Length front wheel to COG	L_f	1	1.4210	m
Length rear wheel to COG	L_r	1.454	1.5790	m
Moment of inertia	I_z	1627	1500	Kg m^2
Front tire stiffness	C_f	13000	13000	N/rad
Rear tire stiffness	C_r	13000	13000	N/rad
Gravity	g	9.81	9.81	N

Note that for this early stage, very simple simulation, the direct yaw moment was implemented directly onto the vehicle model. This means that the corrective yaw moment is transferred in ideal condition with no losses, this would not be possible in practise as the torque would need to be allocated to the separate wheels and there would be physical limitations such as the maximum torque of the motors and upholding the drivers desired trajectory. Theoretically the direct yaw moment can be implemented successfully via a PI controller. The yaw rate in Figure 5.2, Figure 5.5 and Figure 5.8 the implementation on the ATN solar car is compared to a standard sized vehicle. The controlled yaw rate is almost identical to the desired yaw rate for all cases. Although implementation on the standard vehicle is successful, there slight deviation between the actual and desired yaw rate.

Sideslip angle in in Figure 5.3, Figure 5.6 and Figure 5.9 was also successfully restored via the direct yaw control. In comparison to the uncontrolled vehicle, the controlled sideslip is in general considerably lower. However, the abruptness of change may be reflect poorly on the vehicle handling. However since the vehicle model considered in this simulation is very simple it most likely does not reflect the true impact of the control very well, as discussed in Chapter 3, a more advanced vehicle model is required for more accurate results. In the simulation the linear region of the tyre was considered and simply represented by the cornering stiffness. Although the solar car sideslip diverges significant and with less overshoot, compared to the general vehicle may be due to a fairly large cornering stiffness compared to the vehicles weight. Due to lack of data the tires were simply estimated for this model whilst the standard vehicle parameters were borrowed from [98] which does not necessarily reflect the true value well, this is further discussed in Chapter 9

All values diverge, which is reasonable since the angle becomes constant. For the ATN BWSC 2019 vehicle the values diverge a lot quicker and more aggressively both for yaw and side slip angle compared to the standard vehicle. This is not surprising since the parameters are arguably lesser. Although less overshoot is desirable, there aggressiveness would in practice not be desired.

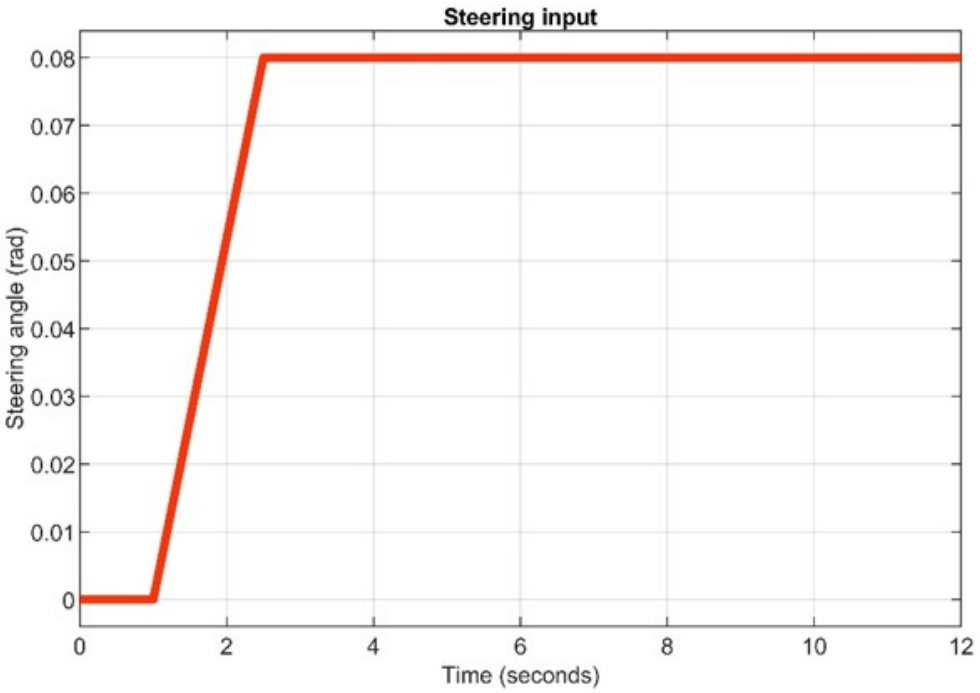

FIGURE 5.1: Gradual steering input

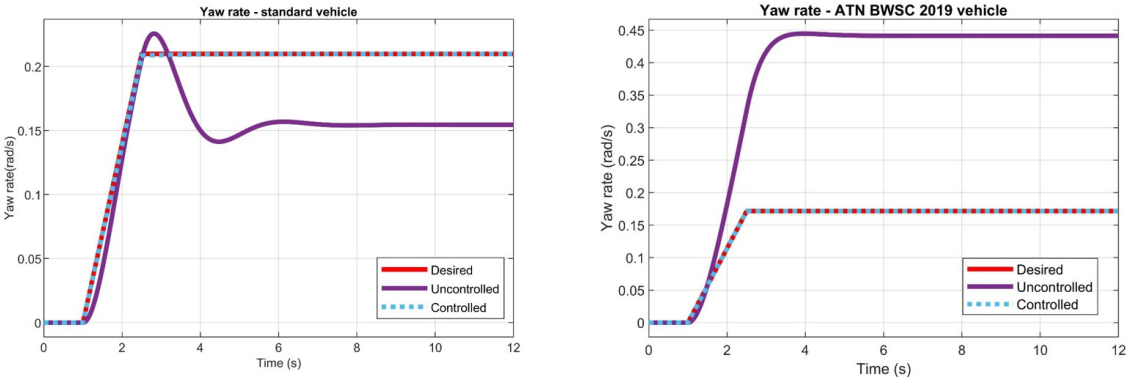

FIGURE 5.2: Yaw rate of an average sized vehicle compared to ATN solar car, with and without PI control dring gradual steer input

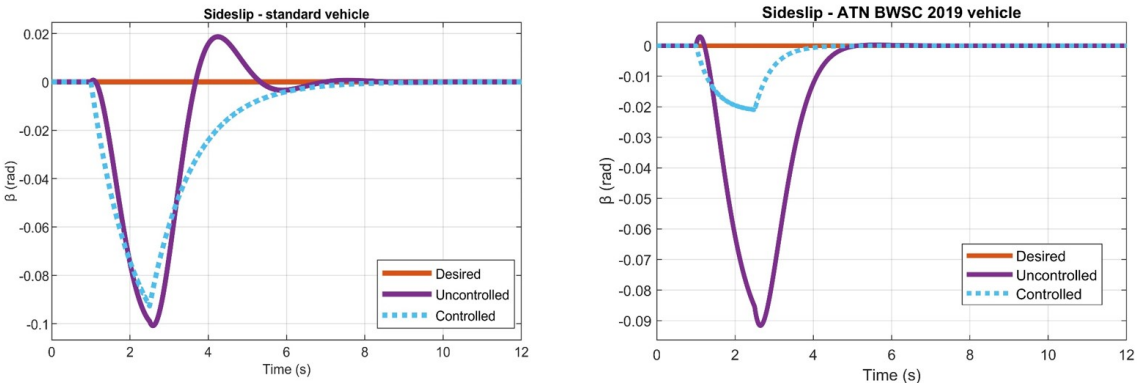

FIGURE 5.3: Sideslip of an average sized vehicle compared to ATN solar car, with and without PI control during gradual steer input

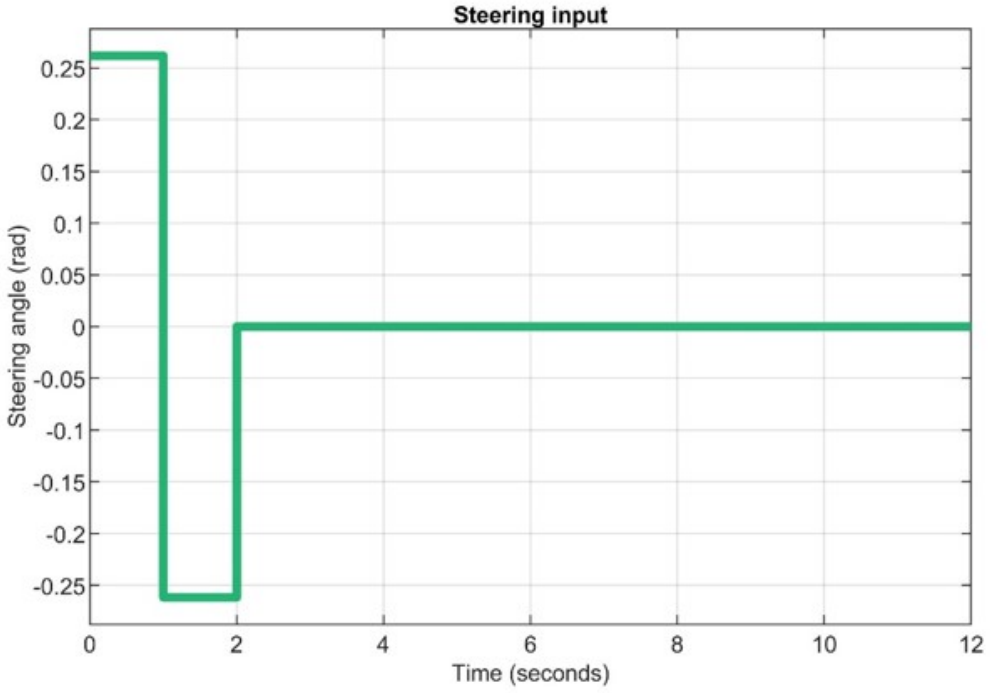

FIGURE 5.4: Step steer input

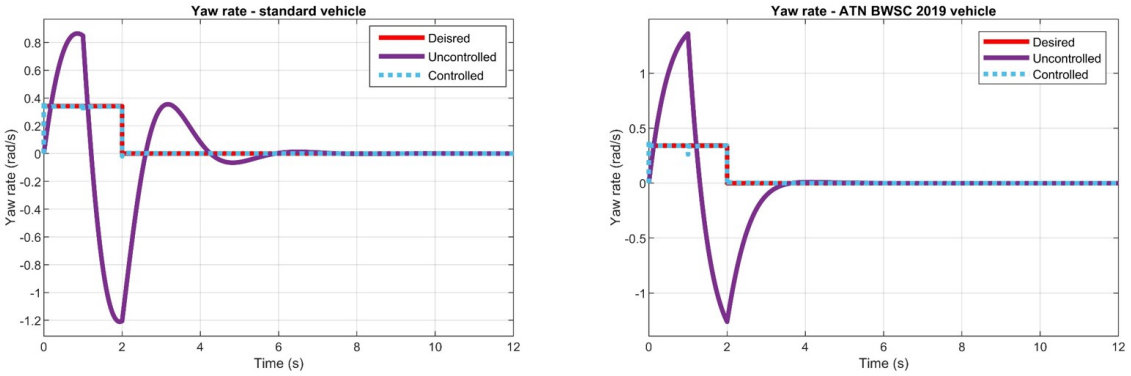

FIGURE 5.5: Yaw rate of an average sized vehicle compared to ATN solar car, with and without PI control during step steer input

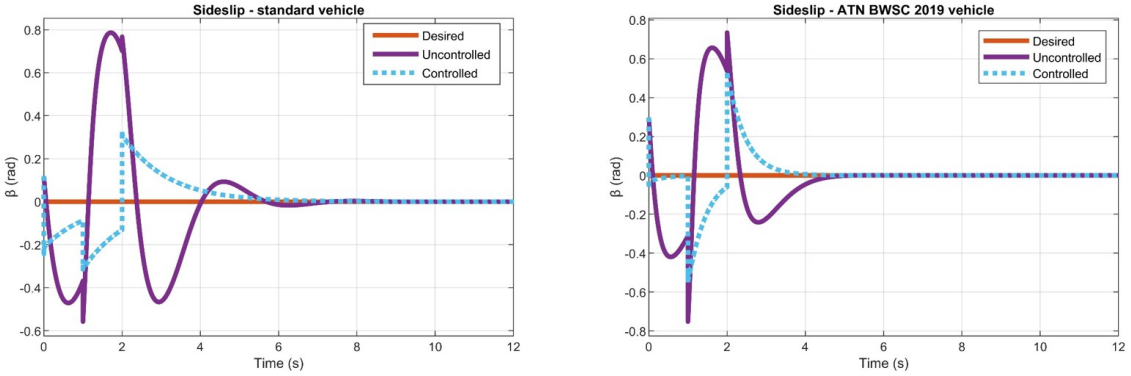

FIGURE 5.6: Sideslip of an average sized vehicle compared to ATN solar car, with and without PI control during step steer input.

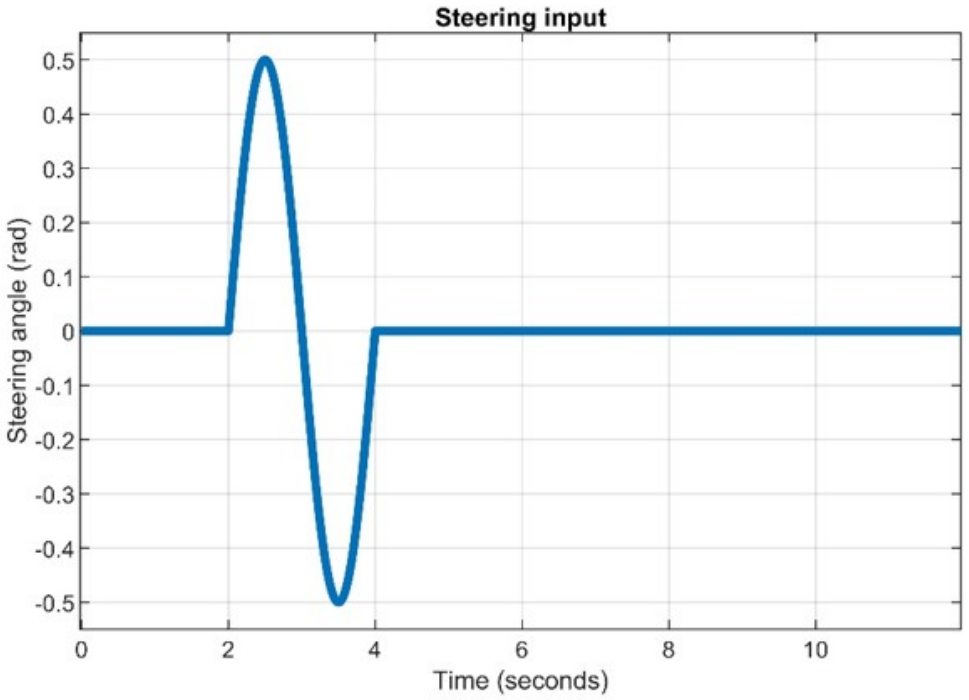

FIGURE 5.7: Swept sine steer input

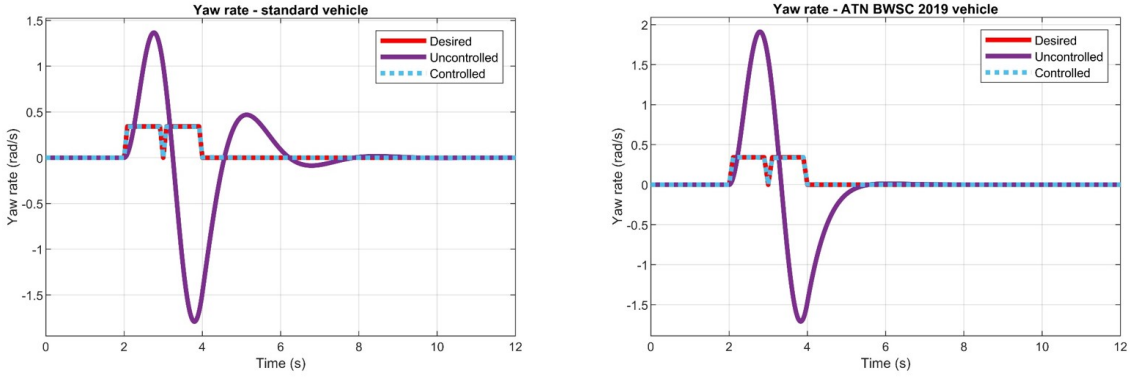

FIGURE 5.8: Yaw rate of an average sized vehicle compared to ATN solar car, with and without PI control during swept sine steer input

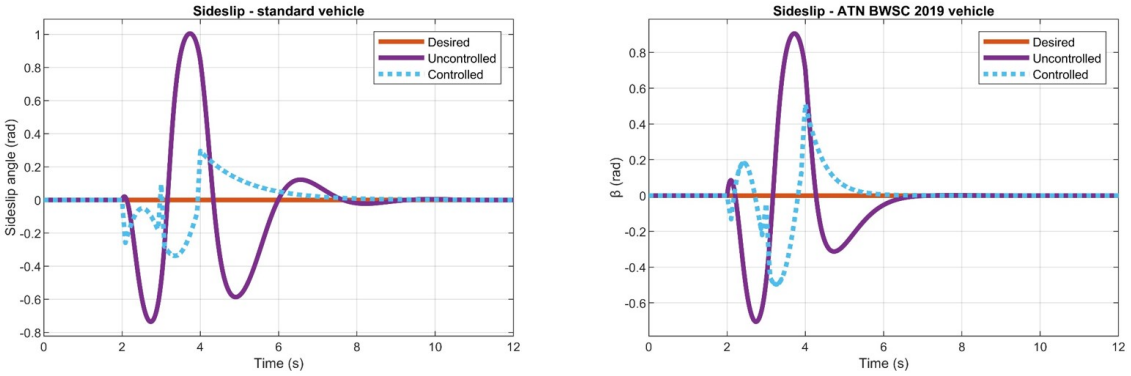

FIGURE 5.9: Sideslip of an average sized vehicle compared to ATN solar car, with and without PI control during swept sine steer input.

5.1.2 Advanced Vehicle Model: DCC

The general vehicle that is considered in this section has the default parameters as set in Simcenter Amesim^{TM} iCar model that can be found in the Table 5.2. Similar to the lightweight vehicle this vehicle is considered as a rear wheel drive.

TABLE 5.2: Vehicle parameters of general iCar model and ATN solar car.

Description	Symbol	General	ATN	Unit
Mass	m	1300	284	Kg
Yaw inertia	I_z	1300	566.58	Kg m^2
Wheelbase	L	2.454	3	m
Length fron front wheel to COG	L_f	1	1.516	m
Length fron rear wheel to COG	L_r	1.454	1.484	m
Track	L_t	1.45	1.615	m

Flat road with constant road grip ($\mu = 0.9$) has been assumed for this study. Ideal torque demand was assumed and influence by aerodynamics on the vehicle body have been neglected.The tire cornering stiffness was obtained from estimation using Pajeckas magic formula directly from the iCar tire mode in Simcenter Amesim^{TM} for the general vehicle. Due to lack of data for the tires on the lightweight vehicle, these have been approximated

To investigate the effectiveness of the control strategy a double lane change maneuver is performed. The vehicle body velocity remain constant throughout the maneuver, at the velocity of 80 km/h. The steering wheel angle profile is displayed in Figure 5.10.

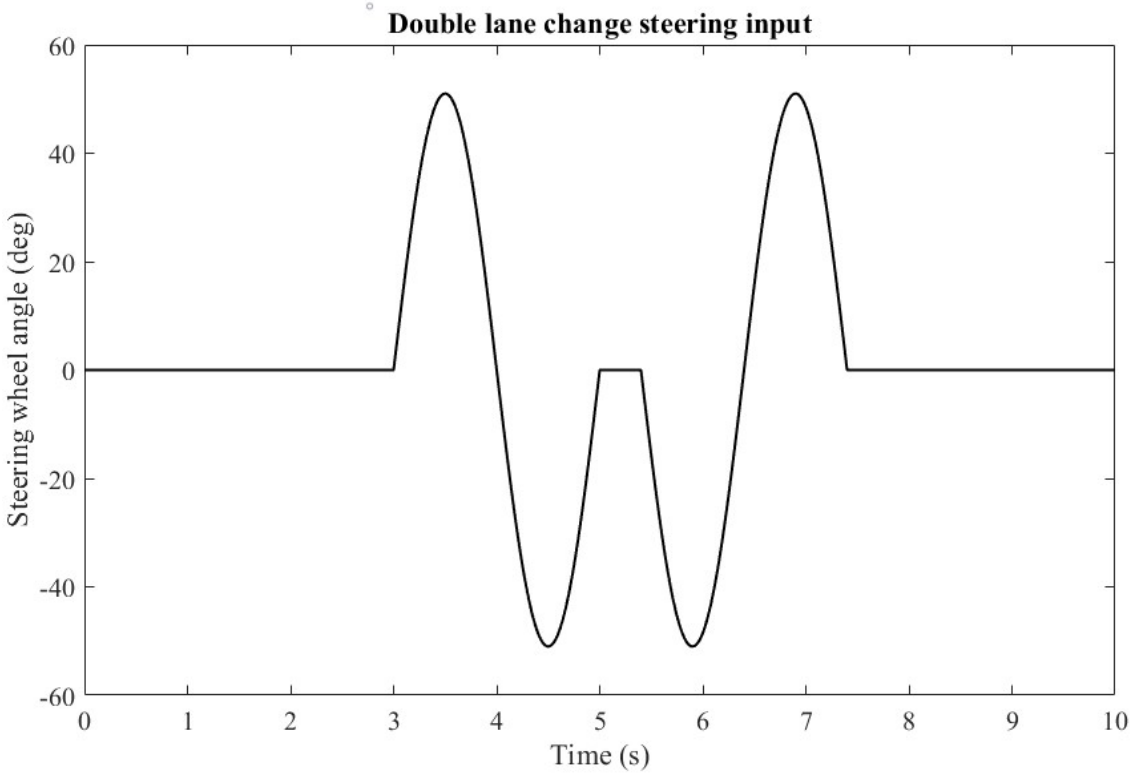

FIGURE 5.10: Double lane change steering wheel angle profile

There is improvement of the dynamic curvature for both controlled vehicles as seen in Figure 5.11. The magnitude of the uncontrolled vehicle was larger for the lightweight vehicle. The controlled lightweight vehicle is however able to achieve similar magnitude as the controlled general vehicle, but without the oscillation at the end. Although, the rate change is more drastic for the lightweight vehicle than for the general vehicle. This indicates poorer performance in terms of both drive stability and comfort.

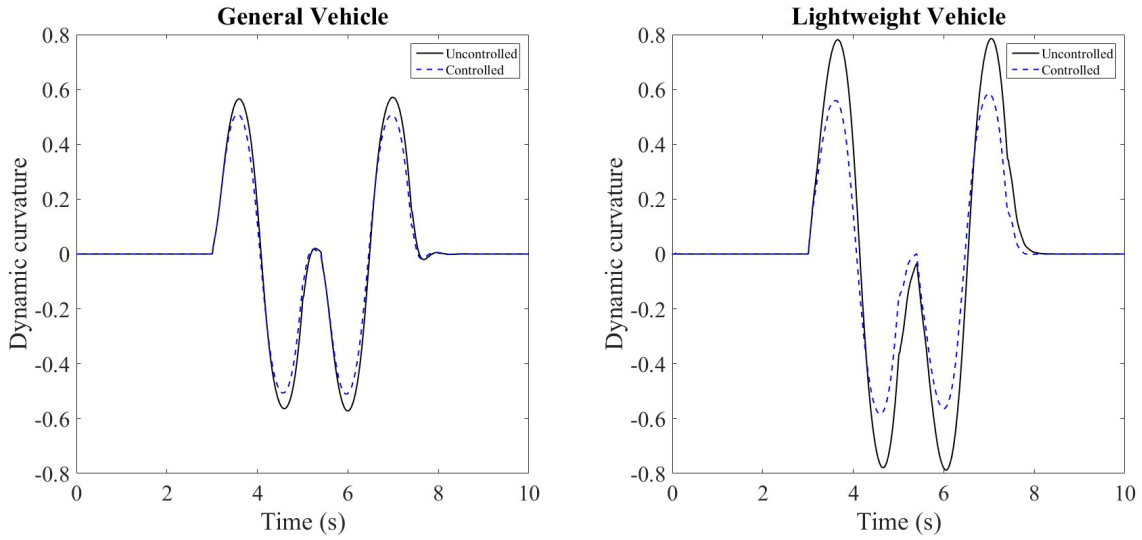

FIGURE 5.11: Dynamic curvature for the controlled and uncontrolled vehicles.

Similar to the dynamic curvature in Figure 5.11, the yaw rate for the uncontrolled lightweight vehicle has a larger magnitude than the general vehicle in Figure 5.12. Additionally,the lightweight vehicle has a smoother transitioning and settles to a stable output earlier. The controlled lightweight vehicle settles earlier than when uncontrolled.

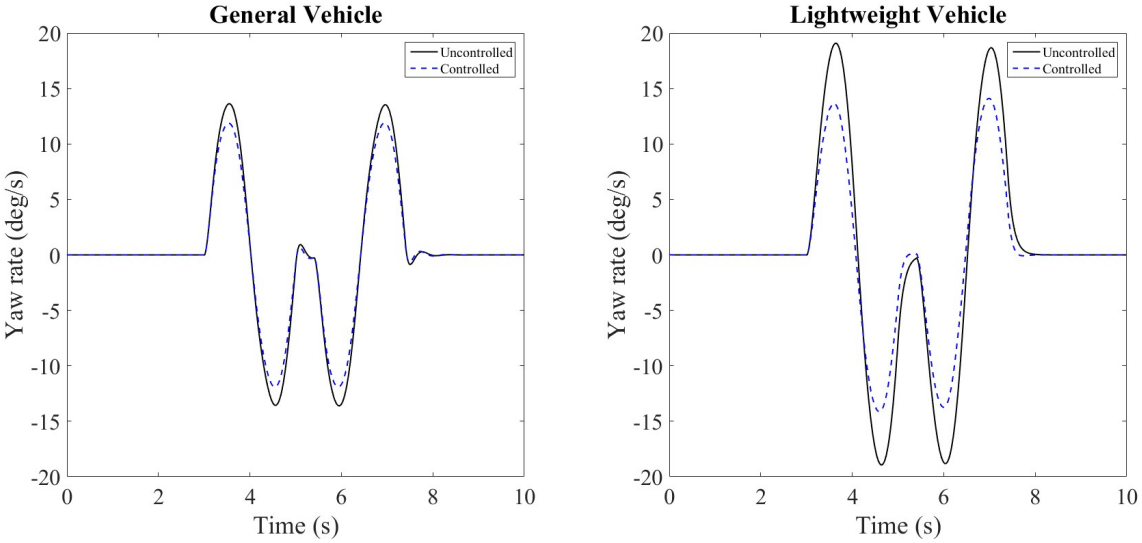

FIGURE 5.12: Yaw rate for the controlled and uncontrolled vehicles.

The controlled and uncontrolled sideslip for the two vehicles is displayed in Figure 5.13. Although the lightweight vehicle sideslip overshoots in the beginning of the maneuvering,

it returns to the desired sideslip quicker than the general vehicle. However, drastic changes as reflected in the dynamic curvature are also displayed.

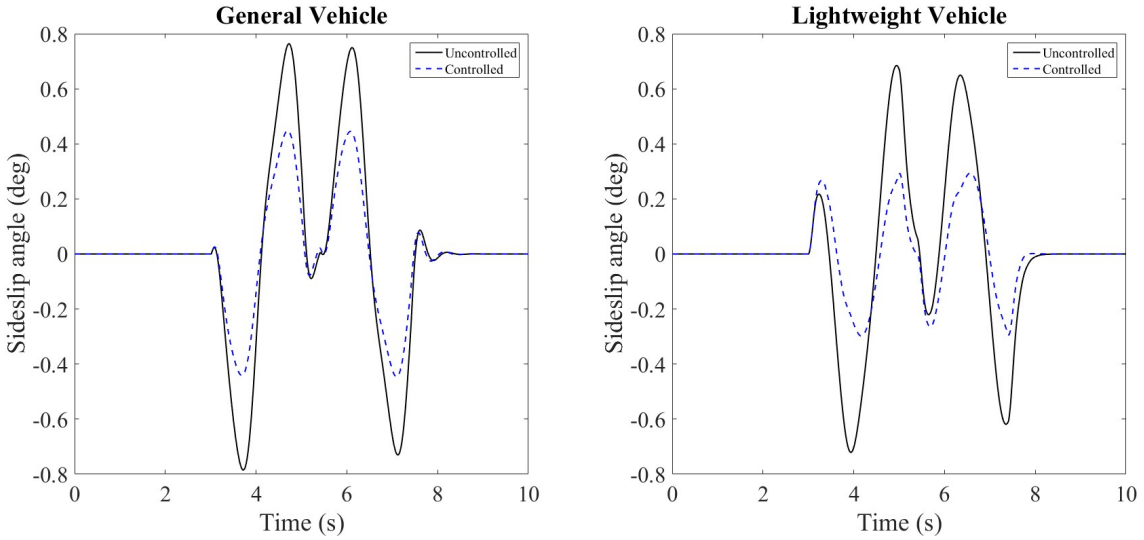

FIGURE 5.13: Sideslip for the controlled and uncontrolled vehicles.

As per Figure 5.14, both the controlled and uncontrolled general vehicle are within the lanes when performing the maneuver. The controlled vehicle is however able to perform tighter cornering. For the lightweight vehicle however, the uncontrolled vehicle is outside of the lane, which is not satisfactory. The controlled vehicle is however well within the lane, which is a satisfactory result. None of the results return to back to the middle of the lane, owing to open loop control of vehicle steering input.

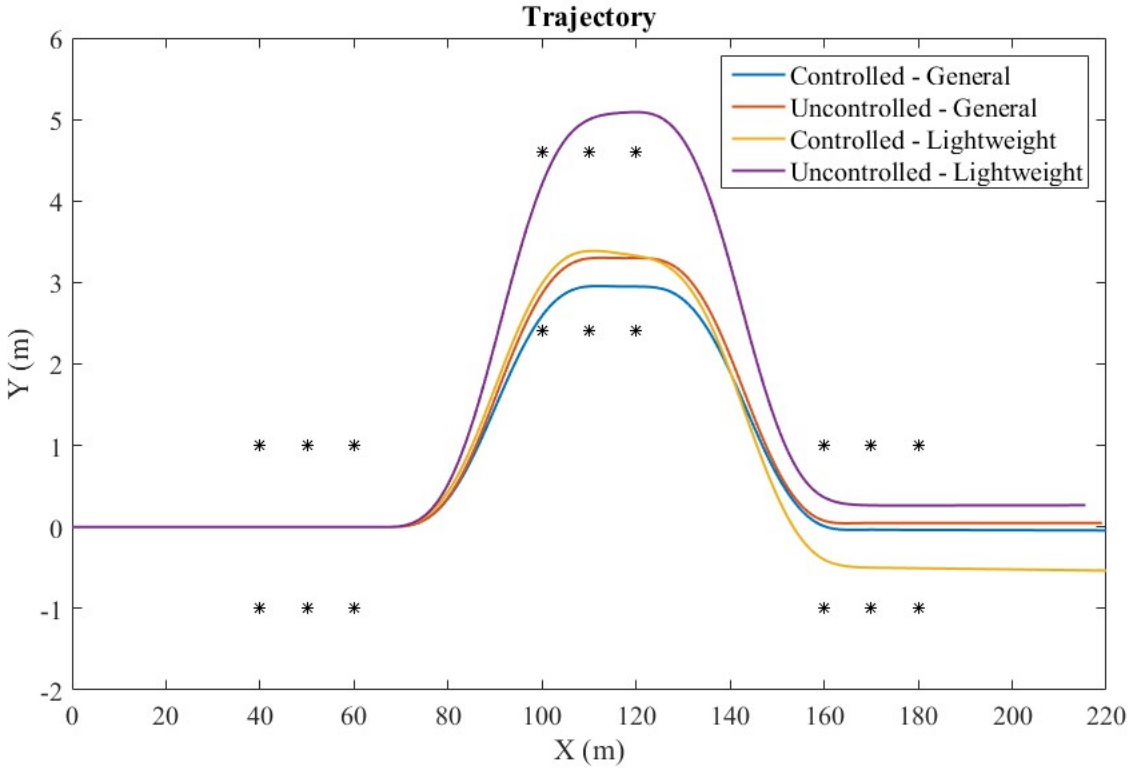

FIGURE 5.14: Trajectory of the two vehicles, controlled and uncontrolled

5.1.3 Conclusion

In this section the ATN solar car was compared to a general sized vehicle. The performance of the PI control was evaluated using a simpled model, and indicates that the control can sucessfully establish an assistive moment to improve the sideslip and yaw rate. The DCC control was evaluated on an advancecd model and the simulation results suggest that it is possible to use dynamic curvature as a means to improve both yaw and side slip for both vehicles. The simulation results indicate that the dynamic uncertainty of the lightweight vehicle requires appropriate chassis control. It further highlight the importance of studying lightweight vehicles as the solar car is unable to perform safe maneuvering without control for the simulated velocity, incomarison to a regular sized vehicle.

5.2 Load Sensitivity Study

Simcenter Amesim™ was used to realise the vehicle model, by utilising the iCAR model application as described in Chapter 3, Section 3.2.

Large variations load-to-curb weight ratios are linked to significant changes in parameters critical to control design for vehicle stability control system. Unique and highly customised vehicles, such as the ATN solar car, are more susceptible to the impact of such variations when developing control methods. The purpose of this study is to study the influence of variation in loading conditions and the effect of ignoring changes in inertial parameters. This study was presented in [96] and include the Sliding Mode Control (SMC) both the nominal and when including uncertainty, Dynamic Curvature Control (DCC) and the Proportional–Integral Control (PI) strategies presented in Chapter 4. Each controller was implemented through co-simulation via MATLAB© Simulink© and Siemens Amesim™ using a 15-DOF non-linear vehicle model presented in Chapter 3.

The base vehicle parameters for this study are described in Table 5.3

Table 5.3: ATN solar car vehicle parameters for load variation study

Parameter	Symbol	Value	Unit
Mass	m	281.52	kg
Moment of inertia	I_{zz}	567	kg m^2
Distance front axis to COG	l_f	1.52	m
Distance from rear axis to COG	l_r	1.49	m
Vehicle track	t_r	1.615	m
Tire cornering stiffness front	C_f	1052	N/deg
Tire cornering stiffness rear	C_r	1052	N/deg

5.2.1 Influence of Load Variation

In this section the consequence of load variation and how it affects the solar cars parameters is presented. Although there are numerous variations of load scenarios, the focus is on

the handling limits during maximum weight allowance for the solar car. As such, the load scenarios, reference naming and the effect on load-to-curb weight ratio are described in Table 5.4.

TABLE 5.4: Scenario effect on weight and curb-to-load-weight ratio.

Description	Scenario	Additional weight	Total weight	Curb-to-weight ratio
Empty	S0	0 kg	281.52 kg	0%
Driver	S1	80 kg	361.52 kg	28%
Driver, passenger and luggage	S2	240 kg	521.52 kg	85%

To study how much the location of mass influence the parameters of the vehicle, the luggage mass has been shifted in the lateral and longitudinal direction to their furthest points for space allowance within the solar car. In such scenarios for S2 is expressed in terms of the location of the luggage's lateral distance from the vehicle centre line as; S2a – on the centre line, S2b – behind the driver, S2c – behind the passenger. These scenarios have been expanded to allow for study of change in longitudinal location of the luggage, which is expressed in terms of distance from the front axis (FA). As such the load scenarios and reference naming can be found in 5.5.

TABLE 5.5: Detailed description of scenarios with load variation and change in location

Scenario	Scenario description
S0	Empty vehicle
S1 mass	Driver Only mass has been updated
S1	Driver Vehicle parameters have been updated
S2 mass	Driver, passenger and luggage included Only mass has been updated
S2a1.2 S2a2 S2a2.5	Driver, passenger and luggage included Luggage location: Centralised Distance from centre line = 0 Longitudinal distance from front axis = 1.2; 2 & 2.5 m
S2b1.2 S2b2 S2b2.5	Driver, passenger and luggage included Luggage location: Behind driver Distance from centre line: +0.5575 Longitudinal distance from front axis: 1.2; 2 & 2.5 m
S2c1.2 S2c2 S2c2.5	Driver, passenger and luggage included Luggage location: Behind passenger Distance from centre line: -0.5575 Longitudinal distance from front axis = 1.2; 2 & 2.5 m

5.2.1.1 Load Scenario Influence on Parameters

Large parametric changes can be displayed for the loaded vehicle scenarios in comparison to the empty vehicle as per Table 5.6. Particularly large values are displayed for scenario S2b at 1.2m from FA, further on referred to as S2b12, with a 90% increase in moment of inertia around the z axis.

TABLE 5.6: Parameter details in relation to the corresponding load scenario.

Longitudinal distance from FA (m)	Mass (kg)	L_f (m)	L_r (m)	I_{xx} (kg/m^2)	I_{yy} (kg/m^2)	I_{zz} (kg/m^2)
		S0				
N/A	281.52	1.52	1.48	141.56	263.58	566.58
		S1				
N/A	361.52	1.39	1.61	302.14	275.62	771.05
		S2a				
1.2	521.52	1.3	1.7	538.36	283.73	1017.46
2	521.52	1.42	1.58	392.32	325.87	883.88
2.5	521.52	1.5	1.5	323.25	395.35	869.41
		S2b				
1.2	521.52	1.3	1.7	588.06	283.73	1078.52
2	521.52	1.42	1.58	428.57	325.87	928.96
2.5	521.52	1.5	1.5	353.19	395.35	906.92
		S2c				
1.2	521.52	1.3	1.7	498.85	283.73	967.5
2	521.52	1.42	1.58	365.67	325.87	849.16
2.5	521.52	1.5	1.5	302.63	395.35	841.9

5.2.2 Results and Analysis

In this section, the results of the implemented controls and the influence of parametric changes due to load variation are presented and discussed. A double lane change manoeuvre is performed via an open-loop driver, at a constant speed of 80km/h. Flat and smooth

road surface with the high adhesion coefficient ($\mu = 0.9$) has been assumed in this paper. The scenarios used for the result sets are described in Table 5.5 and in-depth details can of parameters in Table 5.6.

Integral squared error (ISE), integral of the absolute value of error (IAE) and integral of the time-weighted absolute error (IATE) as used in [99], was used to investigate the tuning of the controllers, in the results section it is used as a quantitative evaluation of the different controllers.

5.2.2.1 Vehicle Parameter Sensitivity

To limit the data sets, and highlight the importance of updating the parameters of the vehicle plant, all scenarios were first simulated for an uncontrolled vehicle. Although the peak values are close for both yaw rate and sideslip, it was found that only changing the mass as per S1 mass and S2 mass, caused phase shift discrepancy from the base vehicle, S0, in comparison to when also updating all the inertial parameters 5.15.

The yaw rate is larger for S1 mass and S2 mass, compared to the empty vehicle, whilst when all parameters are updated the yaw rate is smaller. The magnified results also indicate that S1 mass produces a slight phase shift, whilst S2 mass shift significantly further in comparison to the empty vehicle. Similar can be observed for the S2 scenarios with updated parameters, which is expected due to the change of inertial parameters. However, it's the difference in phase shift between S2 mass compared to the other S2 scenarios which should be noted, since this can cause incorrect expectations of how the actual vehicle behaves in comparison with simulation.

The sideslip angle, similar to the yaw rate, show there is a phase shift.Whereas the phase shift for the sideslip angle between S2 mass and the updated S2 parameter scenarios is even more evident. There is an approximately 0.2 s shift between S2 mass and S0, whist for S2a1.2 less than 0.05 s, which is a difference of about 25%. In terms of sideslip peak values, there is only a slight difference in magnitude between S1 mass, S2 mass and S0, whilst S1 produces a larger sideslip angle than S0 and the updated S2 scenarios are lesser

than S0. The differences in peak magnitudes are fairly small between all scenarios, which is worth to take into consideration.

Due to employing an open-loop driver for steering angle input, the Lissajous diagram cannot clearly indicate that steering efforts are reduced. However, it indicates that S2 mass, compared to when all parameters have been updated, produce much less yaw during some steering angles.Which reconfirms the previous statement, that inaccurate modelling approaches can cause an incorrect assumption of the vehicles actual behaviour. As expected, S2c2.5 and S2b1.2, which have the highest and lowest moment of inertia in the z-axis, produce the lowest and highest yaw amongst the S2 scenarios. Since S2c2.5 is the furthest from the S0 future results will only consider these two of the S2 scenarios to make the result sets more concise.

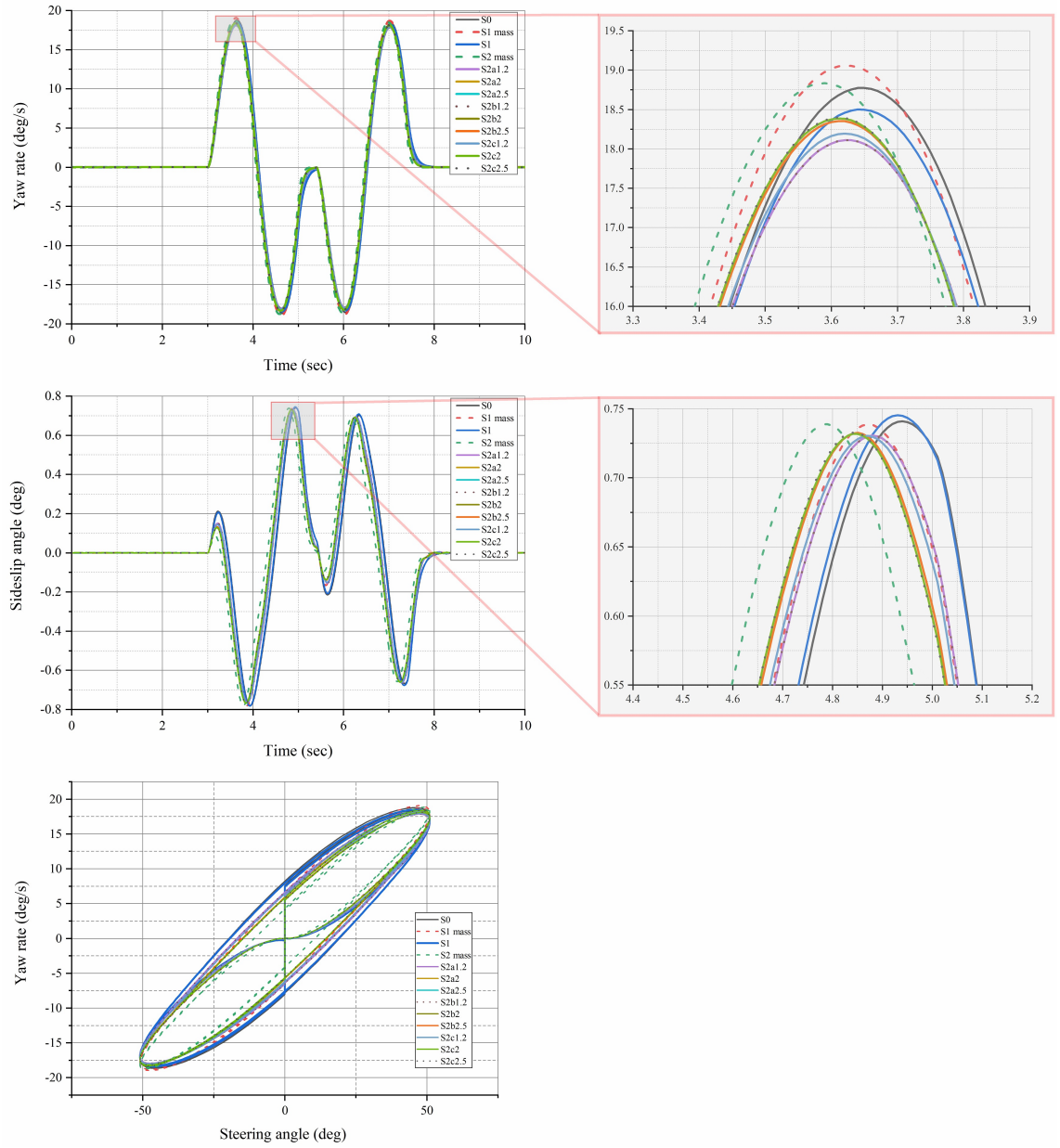

FIGURE 5.15: Yaw rate, sideslip angle and Lissajous diagram of the uncontrolled vehicle during load variation scenarios and corresponding magnified results.

5.2.2.2 SMC Control Efficiency for Parametric Changes

To evaluate how ignoring the change in the internal parameters influence the SMC control performances, we decided to display the uncontrolled S2 mass and S2b1.2 and compare to controlled S2 mass and S2b1.2 5.16. Note that SMC (nom) refers to the nominal control whilst SMC considers the uncertainty as explained in Section 4.5 and (4.33) . The results

show the uncontrolled yaw rate for S2mass and S2b1.2 which is the same as the previous section in 5.15.When applying a controller to these scenarios, yaw is successfully reduced by both SMC and the nominal SMC. It can be seen that the S2 mass generates a slightly lower yaw rate than S2b1.2, although the difference is fairly small. Similarly, there is not a major difference between the performance of the SMC and the nominal SMC (Figure 5.16).

The quantitative evaluation of the controllers supports that there is a lower error for yaw rate in the S2 mass scenario than for S2b1.2, which is not desired. In a real car, the internal parameters automatically change as the vehicle is loaded, which would mean that if we want to physically test, the S2b1.2 scenario correlates better with reality. As such, this highlights potential risks with only considering a change in mass and neglecting the inertial parameters, as this cause the assumption that the controller is more efficient than what is actually the case. Comparing the nominal SMC with the SMC we can see that that the overall peak value for the nominal SMC is lower than for the SMC (Figure 5.16). Although this is desired, the overall performance, even if a minor difference, of the SMC, compared to the nominal SMC is better when we consider the quantitative evaluation in Table 5.7.

The vehicle sideslip angle more clearly displays that there is a significant difference between the controlled S2 mass and S2b1.2, which similar to the yaw rate, would cause for an assumption that the controller is more efficient than it would be in reality. The peak with and without correctly updated internal parameters changes by 50%, indicating a reduced quality of performance overall (Figure 5.16). This is supported by the ISE in Table 5.7, where there is close to a 50% difference between the S2 mass scenario and S2b1.2. Similar to the yaw rate, the peaks for sideslip are slightly lower with the nominal SMC in Figure 5.16, however the overall performance is marginally better for the SMC as per Table 5.7.

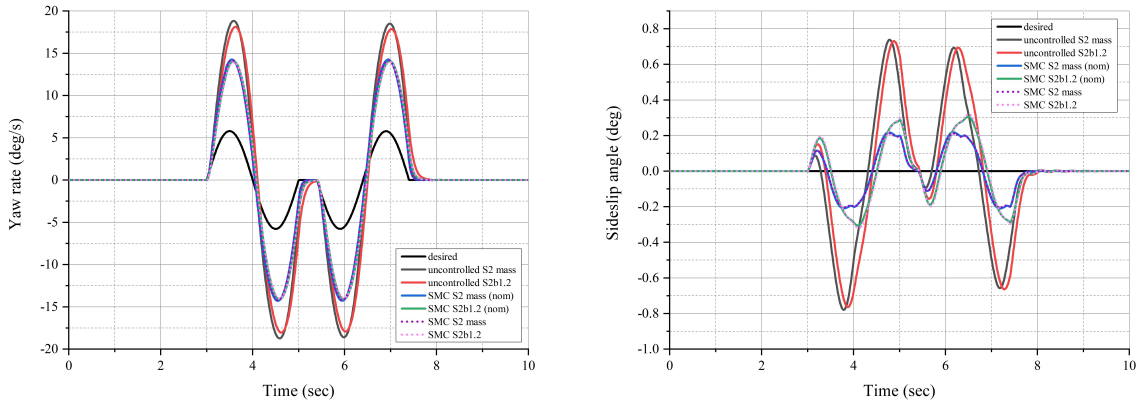

FIGURE 5.16: Yaw rate and sideslip of the uncontrolled vehicle compared to the vehicle with SMC when only considering the change in mass versus when inertial parameters have been updated.

TABLE 5.7: Quantitative evaluation of SMC and nominal SMC using IAE, IATE and ISE for error in yaw rate and sideslip.

Scenario	S2 Mass			S2b1.2		
Test	IATE	IAE	ISE	IATE	IAE	ISE
			Yaw rate			
SMC	121	22.9	156.6	122.8	22.99	156.1
SMC (Nom)	122	23.08	159.2	123.8	23.18	158.8
			Sideslip angle			
SMC	3.193	0.5893	0.09605	4.518	0.8287	0.1854
SMC (Nom)	3.251	0.5997	0.09994	4.56	0.8359	0.1889

5.2.2.3 Control Performance

This section looks at how well the controllers perform for a loaded vehicle. Hence, in this section, all parameters are updated and we are excluding S0, as in reality at least a driver should be included. S1, without control, and S2b1.2, without control, are compared to S2b1.2 with the three controllers. This way, we can investigate how well they perform compared to one another (Figure 5.17).

The SMCs produces lower yaw compared to the DCC and the PI control, by approximately 10% at peaks. Although there is potential for the DCC to settle faster during transitions

in the manoeuvre compared to the other controllers, it tends to over and under shoot. Although the controllers settle rapidly, there is a slight inconsistency towards the end. Whilst the SMC settles to zero at a similar rate as the uncontrolled vehicle, and the PI performs well, there is a larger error for the DCC (Figure 5.17).

The quantitative evaluation of the controllers in Table 5.8 correlates to the observation in the plotted yaw rate in Figure 5.17. As presented in the previous section, there is only a marginal difference between the nominal SMC and SMC, however, a more significant variation can be observed between the different controllers. Both IAE and ISE for yaw rate show an almost 25% difference between SMC and DCC, and close to 30% between SMC and PI (Table 5.8).

The SMCs are superior to when it comes to reducing the sideslip compared to the DCC and PI, with an almost 40% difference in peak-to-peak value at most. Even if the DCC at times display lower response than for the SMC, the behaviour is rather erratic and overall higher. The PI control can successfully reduce the sideslip angle, however, not as much as the SMCs and DCC. Yet, the PI indicates that it is going toward zero at a faster rate than the other two controllers (Figure 5.17).

Similarly, the quantitative evaluation of the sideslip indicates that there is a substantial difference in error between the controllers (Table 5.8). There is a 30% difference of ISE between SMC and DCC, and close to 50% for SMC and PI, which highlights the superior performance of the SMC.

In terms of the vehicles lateral acceleration, the SMCs performs better than both the DCC and PI control. The initial peak suggests that the PI is outperforming the DCC, whilst at the later peak one can see that they are achieving similar results (Figure 5.17).

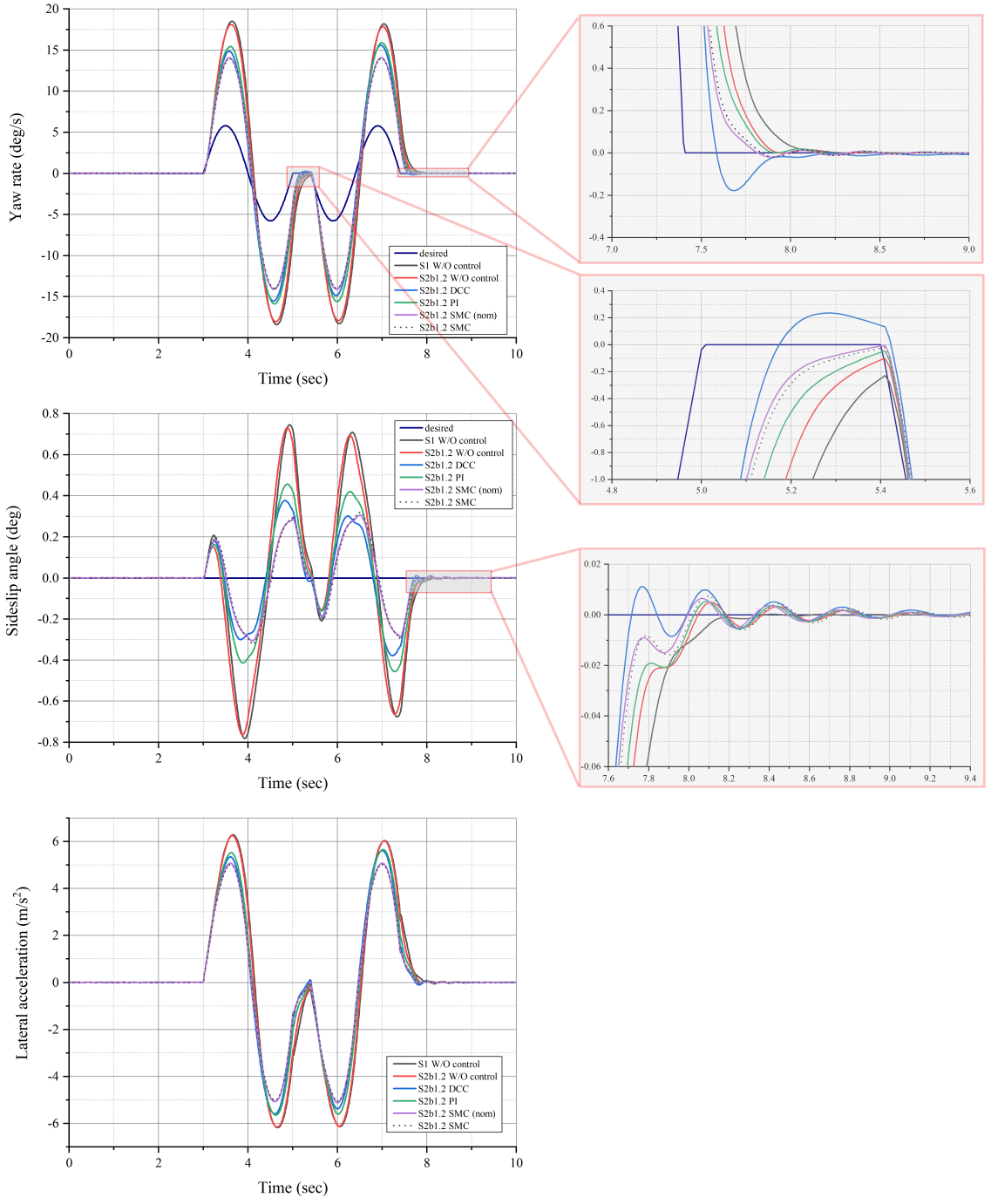

FIGURE 5.17: Comparison between PI, DCC, SMC and uncontrolled vehicle: yaw rate, sideslip angle and lateral acceleration.

TABLE 5.8: Quantitative evaluation of control strategies using IAE, IATE and ISE for error in yaw rate and sideslip.

Scenario	S2b1.2		
Test	**IATE**	**IAE**	**ISE**
	Yaw rate		
SMC	122.8	22.99	156.1
SMC (Nom)	123.8	23.18	158.8
DCC	137.1	25.62	196.6
PI	148.9	27.79	226.2
	Sideslip angle		
SMC	4.518	0.8287	0.1854
SMC (Nom)	4.56	0.8359	0.1889
DCC	5.243	0.9527	0.2504
PI	6.484	1.172	0.3867

5.2.3 Conclusion of

This study investigated (i) the influence in a change in load, (ii) the impact of only updating mass, rather than all parameters for the vehicle plant, and (iii) the performance of DYC strategies (DCC, SMC and PI control) for a loaded vehicle versus when only the driver is present. Unlike previous studies, this investigation was evaluated on an ultra-lightweight vehicle which experiences a high curb-to-load weight ratio as well as relatively large track and wheelbase. The overall weight of the vehicle was increased together with longitudinal changes in location of centre of gravity depending on the loading scenario. This will cause a deviation from design values causing changes in assumptions of an unchanged vehicle model used to define the vehicles desired behaviour.

For the uncontrolled vehicle, it was found that by only updating the mass of the vehicle, rather than mass and internal parameters, it can give a false impression that the vehicle is performing better than it should. This was displayed when introducing an SMC strategy, particularly for the sideslip. When only the mass was updated, the controlled value had

a 50% better peak value compared to when all parameters were updated. Since in reality, the vehicles parameters update as the vehicle is loaded. This would mean that when the controller is transferred to an actual vehicle, it is less efficient than what would have been evaluated simulation. In such, it's important to include changes in vehicle internal parameters when evaluation control systems.

The SMCs, PI and DCC, all have the ability to reduce yaw, sideslip and lateral acceleration. However, the SMC strategies are superior, with approximately 10% difference between yaw rate peaks and an almost 40% difference in the peak value compared to the PI. The DCC generally displays lower response for yaw, sideslip and lateral acceleration than the PI and although producing lower response than the SMCs at instances, it is not as consistent and tends to overshoot. There was only a marginal difference in performance between the nominal SMC and the SMC that include uncertainty, with overall peaks being showing better performance for the nominal SMC, whilst overall error is lower for the SMC. Further refinements should be made to the SMC to avoid the inconsistency present at the end of the manoeuvre due to change in load.

This study was performed to highlight the dangers with vehicles with large changes in load-to-curb weight ratio, and particularly the effect of not considering the change in the internal parameters. Vehicles that are highly dependent on system information, such as autonomous vehicles, could be particularly sensitive to errors due to changes in loading conditions. If not considered appropriately it can be a cause of detrimental outcomes.

Chapter 6

Vehicle Integration and Parameter Estimation

In this chapter the implementation phase for physical testing is presented. The control hardware (dSPACE MicroAutoBox II) is integrated to the vehicle network and vehicle parameter measurement, sensor and parameter tuning were performed.

6.1 Integration to the Controller Area Network

Controller Area Network (CAN) is a serial communication protocol standard which allows for efficient communication between controllers, sensors and other nodes in real-time systems [100]. This protocol is used in industrial automation and areas which require embedded network control, such as machinery, building automation, medical equipment etc. [100]. In vehicles, the CAN protocol facilitates the communication between the network connected components, such as the lights and switch setting or Electronic Control Unit (ECU) and actuators. The use of networks in vehicles allows for improved diagnostics and the coordination between the operations of different subsystems [100]. In the ATN solar car all major electrical components are integrated to the vehicles CAN system in order to provide seamless communication and monitoring.

6.1.1 Vehicle Integration and CAN Layout

The existing CAN is connected to the headlights, MoteC C187 dash to communicate the driver commands, Tritium WaveSculptor22 motor controllers to communicate driver commands from the MoTeC to the motors, the battery and charger port to monitor BMS and charging as in Figure 6.1.

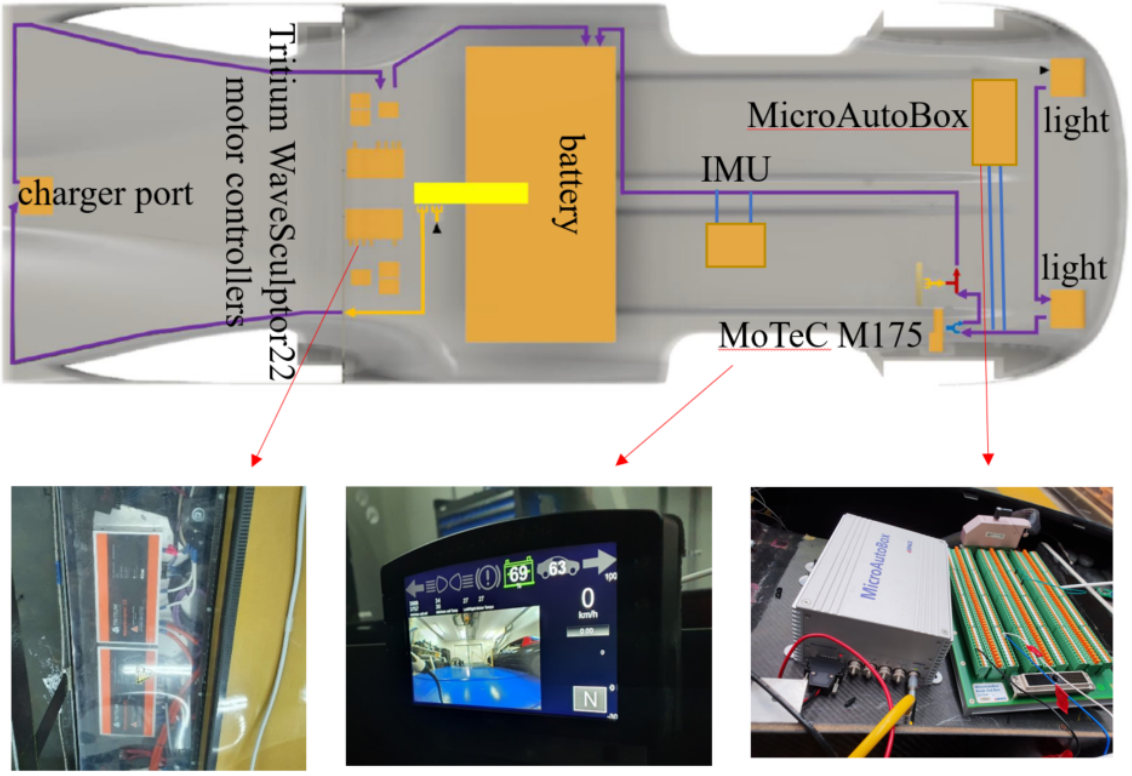

FIGURE 6.1: Vehicle CAN layout with display of components. Adapted from graphics supplied by ATN Solar Car Project, 2019

The existing vehicle control originally consist of a MoTeC C187 dash and two Tritium WaveSculptor22 Motor Inverters. These are able to process simple driver commands, however, the set-up is not capable of any advanced control mathematics. As such, the control strategy is implemented by connecting a dSPACE MicroAutoBox II to the existing network. In addition a Honeywell TARS-IMU was installed and integrated to the CAN to record angular velocities and accelerations as in Figure 6.1.

6.1.2 dSPACE MicroAutoBox II

The dSPACE To verify a control, and assure the safety of the vehicle and its occupants the Simulink® control model is implemented to the vehicle via the dSPACE MicroAutoBox. This step allows for evaluation of the control and parameter estimation and tuning.

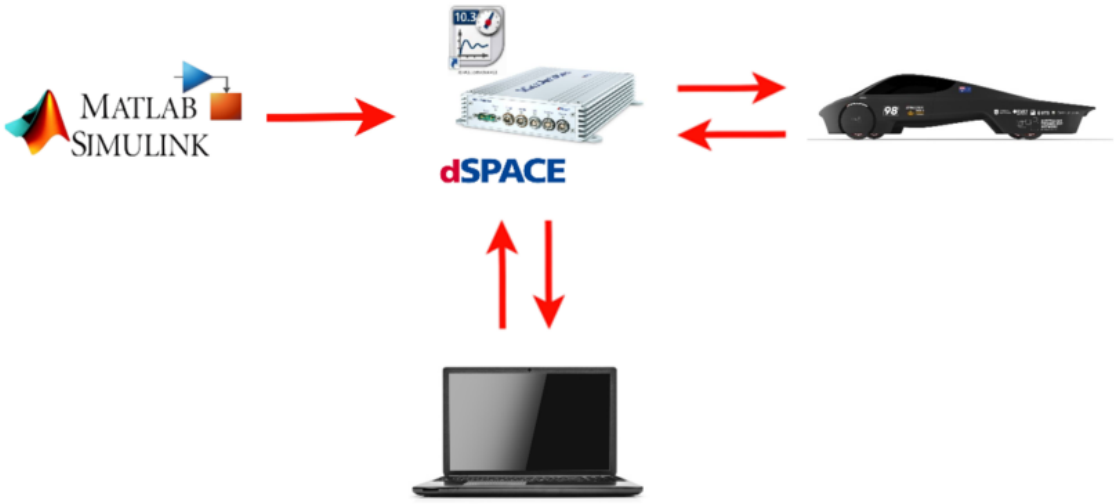

FIGURE 6.2: Control communication layout

The dSPACE MicroAutobox allows for data recording, enabling, disabling and control selection in real-time via the associated dSPACE control desk software. In addition, real-time monitoring permits quick evaluation of data during testing, which assists in tuning sensors and parameter estimations.

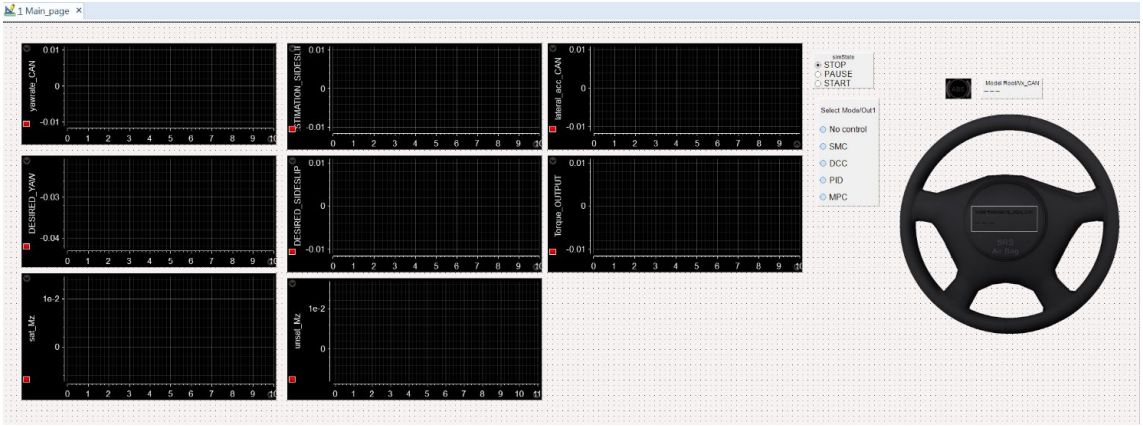

FIGURE 6.3: dSPACE control desk layout for real-time control selection and monitoring

6.2 Center of Gravity Estimation

Due to the design nature of the solar car, with inexact knowledge and representation of the physical components location and actual size. To calculate the COG position, vehicle parameters are obtained by direct measurements (APPENDIX A). The vehicles wheelbase, track and tyre radius are measured using a tape measure. The vehicles static weight distribution can be found by measuring the weight at each contact patch of the tyres, this is done by using the Longcare Computerscales® AccuSet II™ Basic System corner scales. For calculations of the lateral and longitudinal positions of the COG, the corner scale pads have been leveled, with the wheels centred at each pad.

In race vehicles this is done for the conditions in which the vehicle will be raced, including driver, fuel and other fluids topped up. The solar car is however designed as practical vehicle with the option to be driven with either just a driver or both driver and passenger. As such measurements were done for the empty vehicle, with driver, and with driver and passenger.

FIGURE 6.4: COG position measurement set-up

The location of the COG on the x-axis can be calculated from the percentage of the mass which acts upon the front axis as follows:

$$COG_x = \frac{m_f}{m} \times l \tag{6.1}$$

The location of the COG from left to right on the y-axis is calculated from the percentage of mass acting on the right hand side as follows:

$$COG_y = \frac{m_{Right}}{m} \times l_t \tag{6.2}$$

When it comes to finding the height location, the z-axis, of the of COG, measurements are not as straight forward. The rear of the vehicle is lifted, whereas the lifted height and tilt angle together with the front mass distribution is used to find the location of the COG.

$$l_{adj} = \sqrt{L^2 - h_z^2} \tag{6.3}$$

The tilt angle can easily be calculated using trigonometry or below expression can later be used directly:

$$\tan \Phi = \frac{h_z}{l_{adj}} \tag{6.4}$$

The change of front axial mass can be described as:

$$m_{\Delta f} = m_f - m_{fh_z} \tag{6.5}$$

From equations (6.3) to (6.5), the location of COG on the z-axis can be expressed as:

$$COG_z = r_w + \frac{l \times m_{\Delta f}}{m \times \tan(\Phi)} \tag{6.6}$$

These calculations have been applied and summarised in table 6.1 and the visual representation of the location is displayed in Figure 6.5 - 6.7.

TABLE 6.1: Location of center of gravity depending on occupant conditions

Occupants	Left to right position	Front to rear position	Position from ground
Empty	0.7934	1.6387	0.7820
Driver	0.8190	1.5139	1.3401
Driver and passenger	0.7763	1.37682	1.9928

Upon review, the measurements the angle Φ is below the recommended minimum which is likely to cause error for the z-axis calculations. Commonly, vehicles have tie-down points which allows for safe adjustment when changing the tilt angle, this can be hook points or simply around the rim and tyre of the vehicle. Due to the solar cars custom design and with the in-wheel motors occupying the rear wheels, no such point is available without potentially damaging the chassis. In real life testing, these values are not necessarily crusial, however for an accurate model in simulation, the accuracy is key.

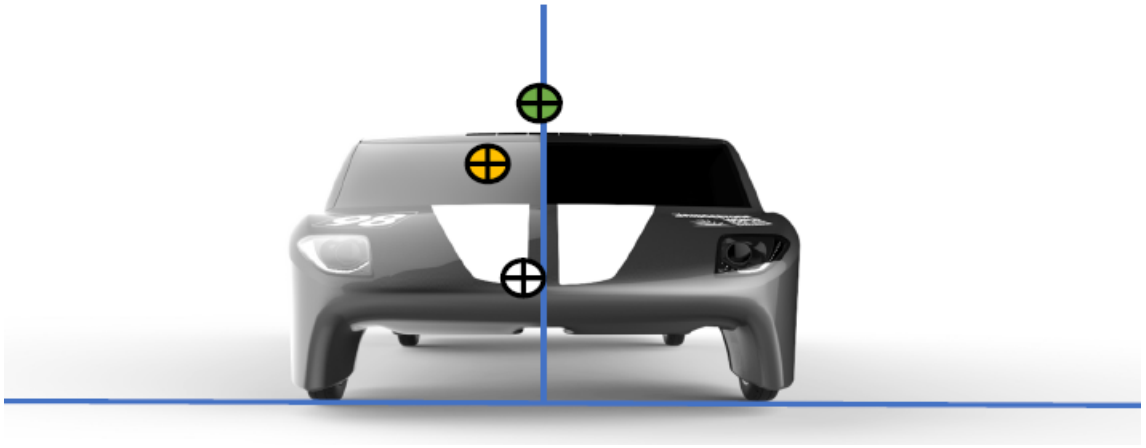

FIGURE 6.5: Visual representation of front view of COG. Adapted from graphics supplied by ATN Solar Car Project, 2019

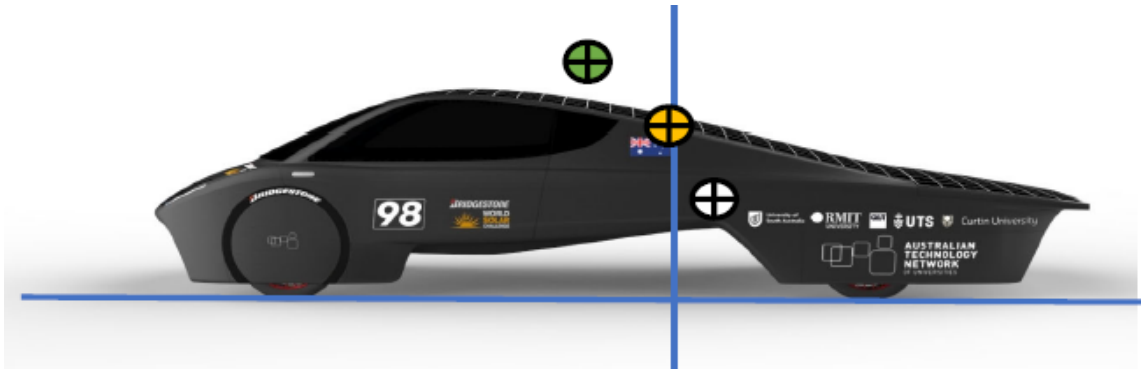

FIGURE 6.6: Visual representation of side view of COG. Adapted from graphics supplied by ATN Solar Car Project, 2019

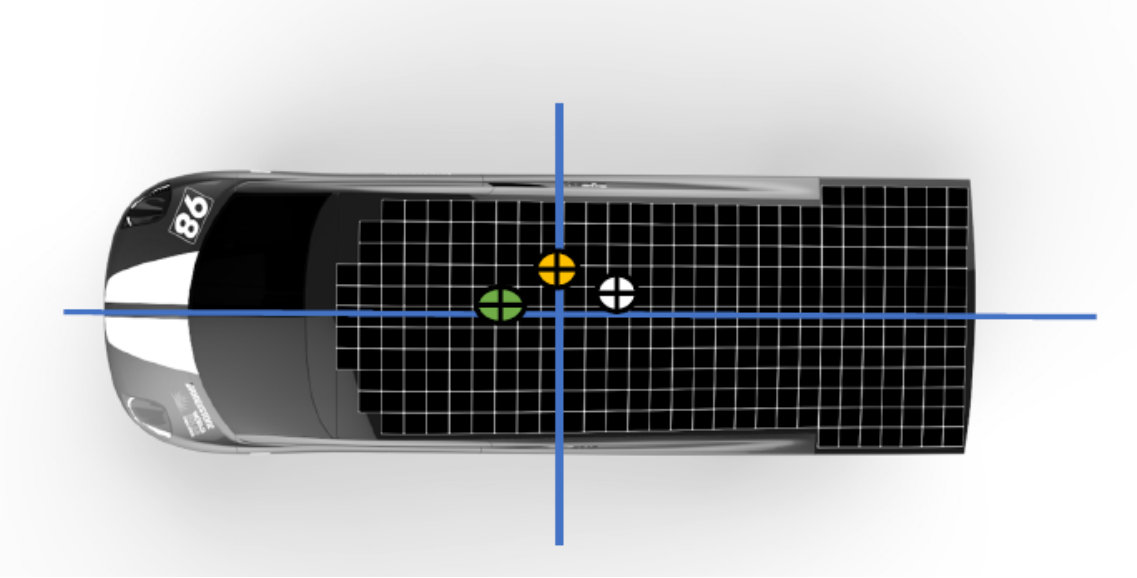

FIGURE 6.7: Visual representation of top view of COG. Adapted from graphics supplied by ATN Solar Car Project, 2019

6.3 Road Angle Compensation

As mentioned in Section 1.5, the adverse test area, shown in Figure 6.8, requires adjustments which were previously out of scope of this research. The test area is limited in size, in combination with the size of the vehicle and its turning circle,it is not possible to perform fishhook or circular trajectory testing. Due to the limited length, it is also not safe to perform any high speed maneuvers. However, the main issue with the test area is the road bank angle, with a seemingly insignificant average of 1.8 degrees, which needs to be adjusted for as it can cause significant error which is presented in Section 6.4.

FIGURE 6.8: Vehicle driving test area.

An inertial measurement unit (IMU) is a sensor unit which measures linear acceleration, orientation and the angular velocity around three axis in space. The IMU provides the measurements in the body frame, which is a coordinate frame of a moving IMU with the origin at the center of the sensor which is usually indicated on its casing [101]. The IMU is sensative in both the linear and local gravitation fields, and is influenced by chassis angles and requires orientation determination. The inertial frame on the other hand is an earth-fixed coordinate system, which means the reference is fixed to earth. The inertial rotation angles and rates are known as Euler angles [102].

The Euler angles can be expressed as a rotation matrix as in [102]:

$$D(\phi,\theta,\psi) = \begin{bmatrix} 1 & \sin(\phi)\tan(\theta) & \cos(\phi)\tan(\theta) \\ 0 & \cos(\phi) & -\sin(\phi \\ 0 & \sin(\phi)/\cos(\theta) & \cos(\phi)/\cos(\theta) \end{bmatrix} \tag{6.7}$$

The Euler rates can be expressed as:

$$\begin{bmatrix} \dot{\phi} \\ \dot{\theta} \\ \dot{\psi} \end{bmatrix} = \begin{bmatrix} p + q\sin(\phi)\tan(\theta) + r\cos(\phi)\tan(\theta) \\ q\cos(\phi) - r\sin(\phi \\ q\sin(\phi)/\cos(\theta) + r\cos(\phi)/\cos(\theta) \end{bmatrix} \tag{6.8}$$

Whereas in this particular matrix p sensor output roll rate, q refers to the output pitch rate and r the sensor output yaw rate. Not to get confused with the denoted r for yaw rate in Chapter 2 and 3.

6.4 Sideslip Estimation

In simulation environments, finding the vehicle sideslip is simple, however as previously mentioned it can be tricky to measure in real life. There are two primary methods for sideslip estimation known as Model Based Observers and Kinematic Based Observers [65]. The Model Based Observer commonly rely on the liner bicycle model and in such the tyre cornering stiffness, which is known to be influence the accuracy. The Kinematic Based Observers are independent from tyre-road parameters, as they rely on the correlation of the vehicles measured yaw rate, lateral and longitudinal velocity, and the longitudinal and lateral acceleration [65, 66, 103]. Due to prior knowledge that the custom solar car tyres have limited tyre data, it was early decided that the Kinematic Based Observer would be more suitable.

In [64, 70, 96], dynamic curvature was introduced as a control variable, which has the potential of removing the use of complicated estimators during real-life testing. Assuming steady-state of the reference model Chapter 3, Section 3.4, where lateral tire forces at front

and rear are equal to the centrifugal force and the moment due to lateral force is zero and four wheels are considered. The radius of a vehicles driving path for steady state can be described as the curvature in [64, 91] as:

$$\frac{1}{R} = \frac{\delta}{L + mv_x^2(\frac{l_r C_r - l_f C_f}{2C_f C_r L})} \tag{6.9}$$

Where R is the radius of the vehicles cornering path. The drawbacks, as described by [64] is the potential error due to the curvature being derived from the steady state model as well as the cornering stiffness of the tyres have been linearized and approximated. Assuming small slip angle the dynamic curvature variable denoted as k, as presentd in [70], can be expressed as:

$$k = \frac{\dot{\beta} + r}{v_x} \tag{6.10}$$

The use of $k(t)$ allows for the use of the instantaneous curvature at any time during manoeuvring. The lateral acceleration a_y can be obtained from the IMU and is mathematically be expressed as:

$$a_y = (\dot{\beta} + r)v_x \tag{6.11}$$

By expressing (6.10) in relations to (6.11), a relationship between obtainable data and sidelsip can be made as:

$$k = \frac{\dot{\beta} + r}{v_x} = \frac{a_y}{v_x^2} \tag{6.12}$$

Rearrange

$$\dot{\beta} = \frac{a_y}{v_x} - r \tag{6.13a}$$

then sideslip can then be expressed as:

$$\beta = \int \left(\frac{a_y}{v_x} - r \right) dt \tag{6.13b}$$

6.4.1 Lateral Acceleration Compensation

The the lateral and longitudinal acceleration experience bias due to road bank and chassis angles [104]. The measured acceleration, a_{ym} requires gravity compensation in order for a correct estimation of the sideslip as mentioned in [105, 106]. Which can be achieved as follows:

$$a_y = a_{ym} - g\sin(\phi + \chi) \tag{6.14}$$

Whereas χ is the road bank angle, thus $(\phi + \chi)$ represents the vehicle roll angle in the relation to the global co-ordinate field. Correspondingly, the measured roll angle from the IMU can be described $\phi_m = (\phi \pm \chi)$, accommodating for a positive or negative bank angle depending on which direction the vehicle is facing in relation to the IMU coordinate field. As per [105], (6.14) can now be written as:

$$a_y = a_{ym} - g\sin(\phi_m) \tag{6.15}$$

As such, the sideslip with gravity compensation can in its full expansion be expressed as:

$$\beta = \int \left(\frac{a_{ym} - g\sin(\phi_m)}{v_x} - r \right) dt \tag{6.16}$$

The integral is sensitive to sensor offsets and noise which can result in large cumulative errors. In order to remove noise between the maneuvers and to overcome the issue of division by a small numbers, the control has a velocity initiation at 2 m/s. The control initiation velocity is low enough for the vehicle to be considered within its stability region, as such does not oppose any safety concerns. velocity is no longer constant, an accumulative error is introduced.

6.4.2 Evaluation of Sideslip on the Test Track

In order to assess how the the lateral acceleration and sideslip estimation is affected, the vehicle was driven on the test track which has a bank angle of an average of 1.8 degrees. For

a better understanding of the vehicles movement during testing, the velocity and steering angle are displayed in Figure 6.9.

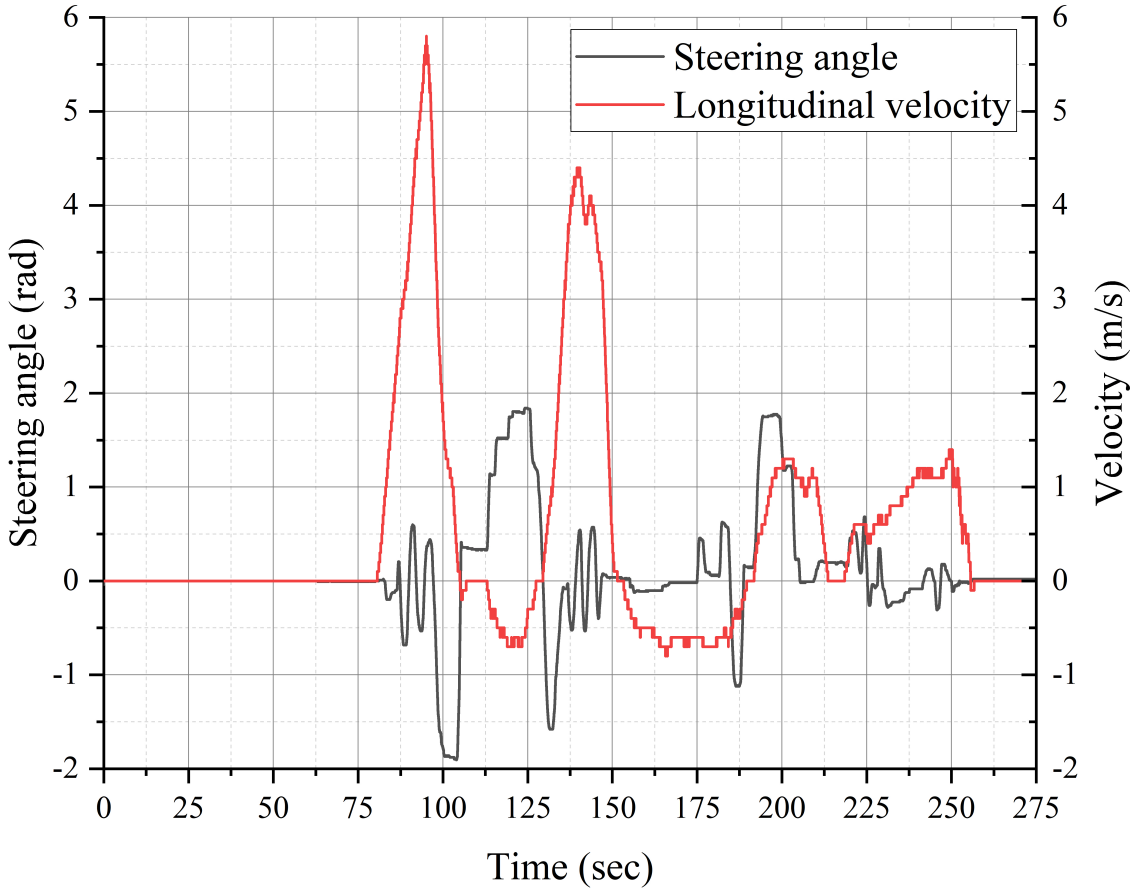

FIGURE 6.9: Vehicle movment in terms of velocity and steering angle during sideslip estimation test

In Figure 6.10, the raw lateral acceleration from the IMU is compared to the lateral acceleration with compensation for gravity. In order to translate the findings in, the actions taken during this test as correlating with Figure 6.9 were (i) instance 0-85 seconds Idle vehicle and straight line driving, driver positioned as $(\phi + \chi)$ which is causing a positive offset for the raw data; (ii) 85-97.5 seconds: slalom manoeuvre; 97.5 - 125 three point turn, whereas the front of the vehicle faces uphill; 125-150 slalom manoeuvre, driver now positioned at $(\phi - \chi)$ which is resulting in a negative offset; 150-175 straight line; 175-275 second: the vehicle is turning uphill to proceed into warehouse area onto a flat smooth concrete flooring, the remaining offset is due to the chassis angle caused by the weight of the driver.

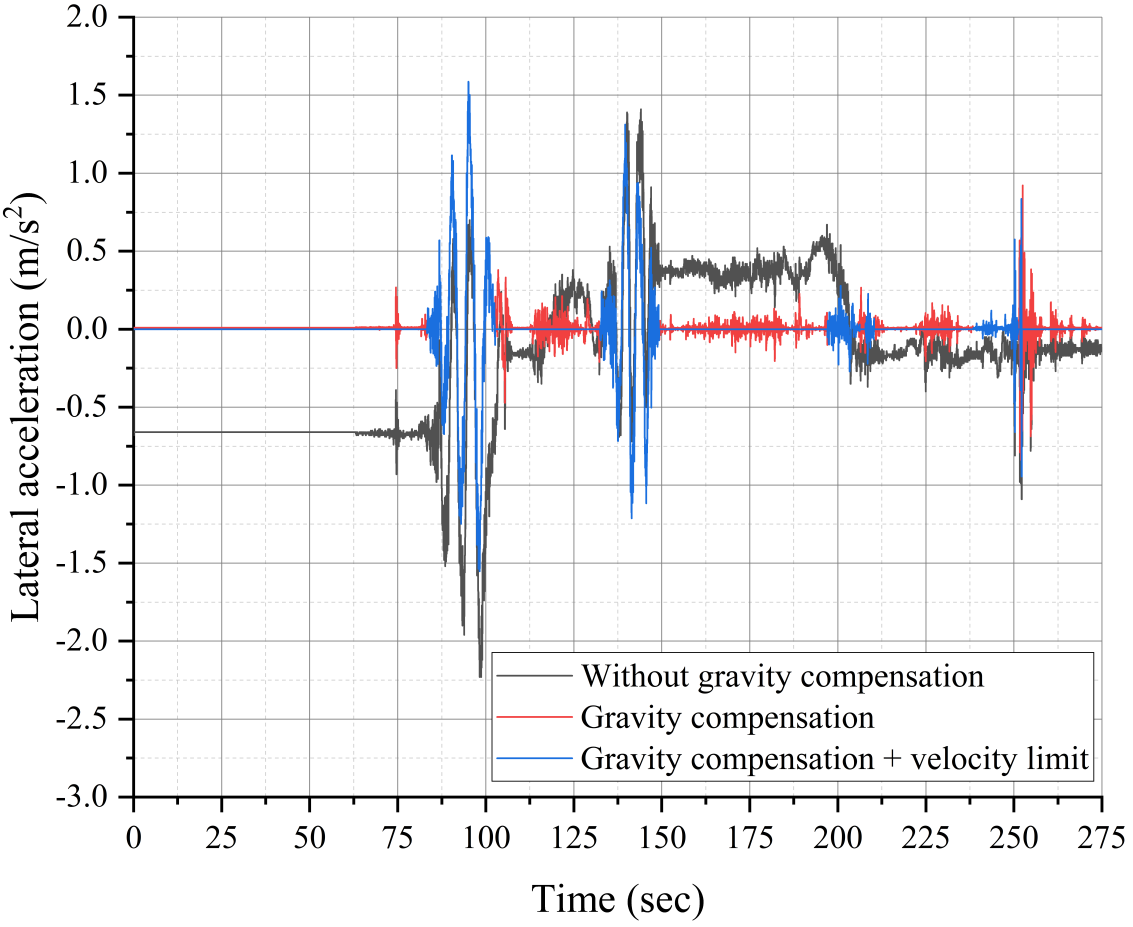

FIGURE 6.10: Lateral acceleration with compensation for gravity.

In Figure 6.11, the impact of which the lateral acceleration has on the estimation of the sideslip is displayed. It can be viewed that the uncompensated acceleration causes an accumulative error. The integral is sensitive to sensor noise, by introducing the initiation limit, it reduces the occurrence of accumulative error.

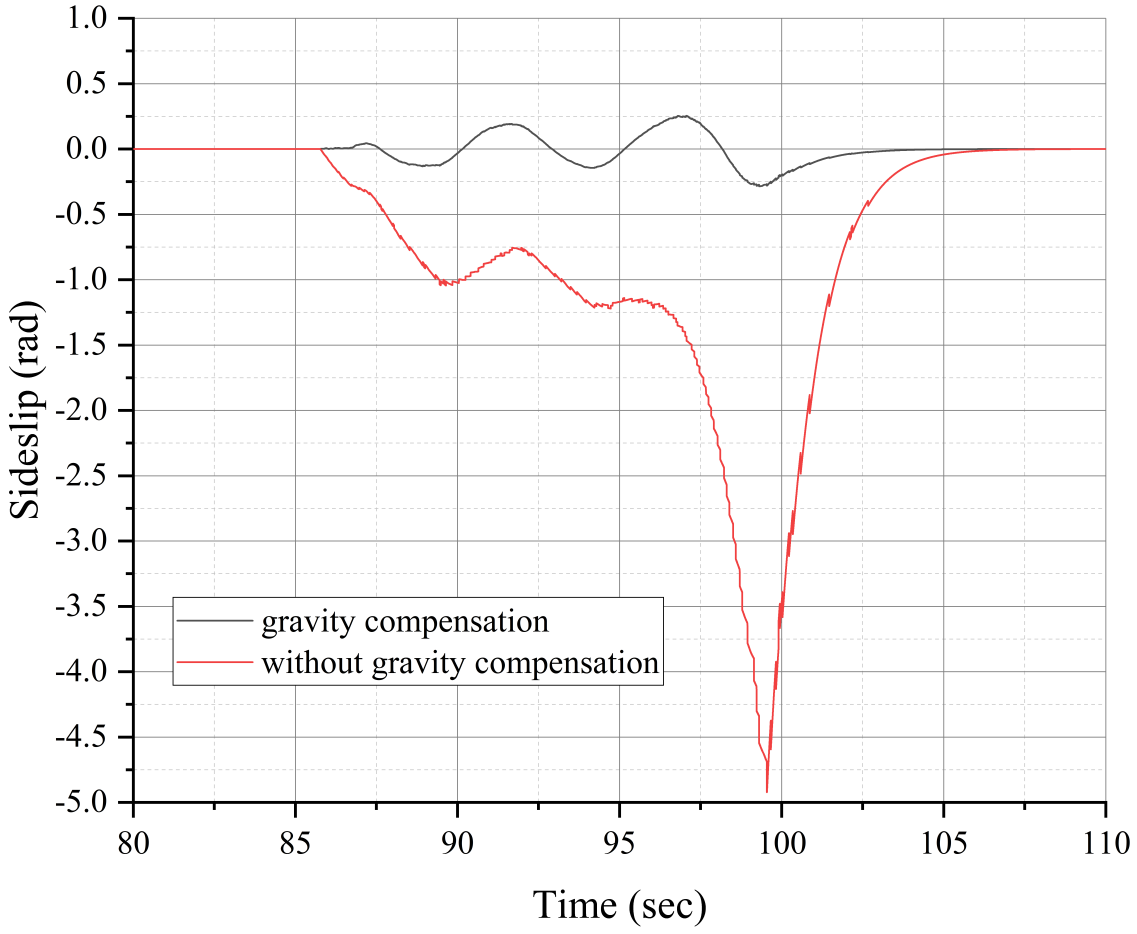

FIGURE 6.11: Sideslip estimation with and without gravity compensation.

When using a Simulink switch block, initial error occurs due to non-smooth transition when initiated. In order to avoid a sudden offset error, a MATLAB function using a persistent variable is introduced to perform the integration as per Appendix C. The comparison between the two methods is presented in Figure 6.12. The initial step error is be eliminated, and the carried error throughout the estimation is reduced. At the time instance 97.5 the three point turn is commenced, the large steering angle produces a fairly large slip and if Figure 6.9 is examined closely, velocity is below just before 100 seconds, which agrees with the instantaneous zero output of the sideslip using the switch block. This does not correlate well with the real-world scenario, however since the control will be disabled at 2 m/s this does not raise a concern. Similarly, the smooth return to zero for the persistent function. In order to avoid similar cut-off, the data sets during testing will consider straight line driving prior and after maneuvers.

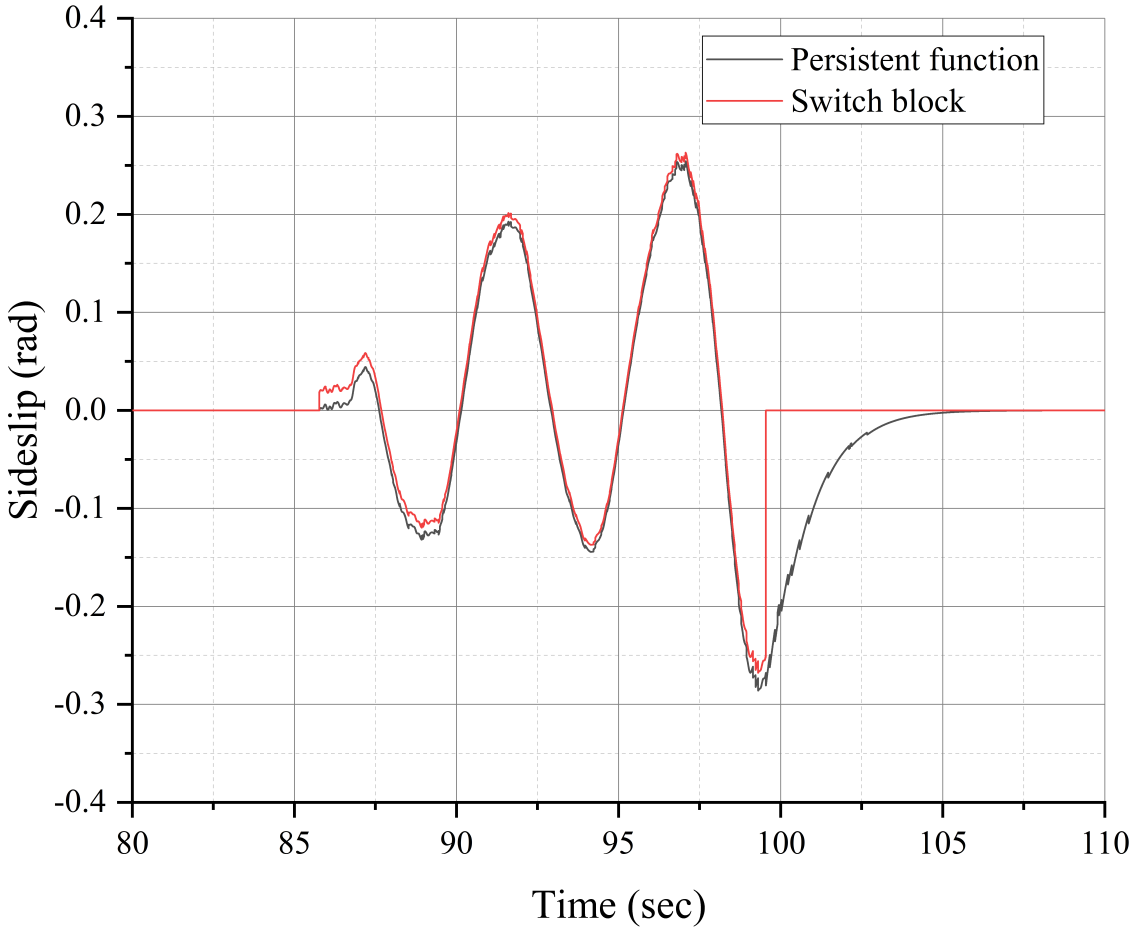

FIGURE 6.12: Sideslip estimation with and without gravity compensation.

6.5 Parameter and Model Tuning

6.5.1 Steering Angle Sensor Offset

The steering angle sensor is installed directly to the steering column and attached to a custom 3D-printed bracket, as per Figure 6.13. Due to undesired slip and flex of the bracket after installation and sensor tuning, the steering angle sensor data includes a significant undesired offset. Since the error was discovered after data collection and due to resource and time constraint, amendment was not possible, instead a manual offset as Figure 6.14 was introduced during post-processing.

FIGURE 6.13: Steering angle sensor installed in the vehicle.

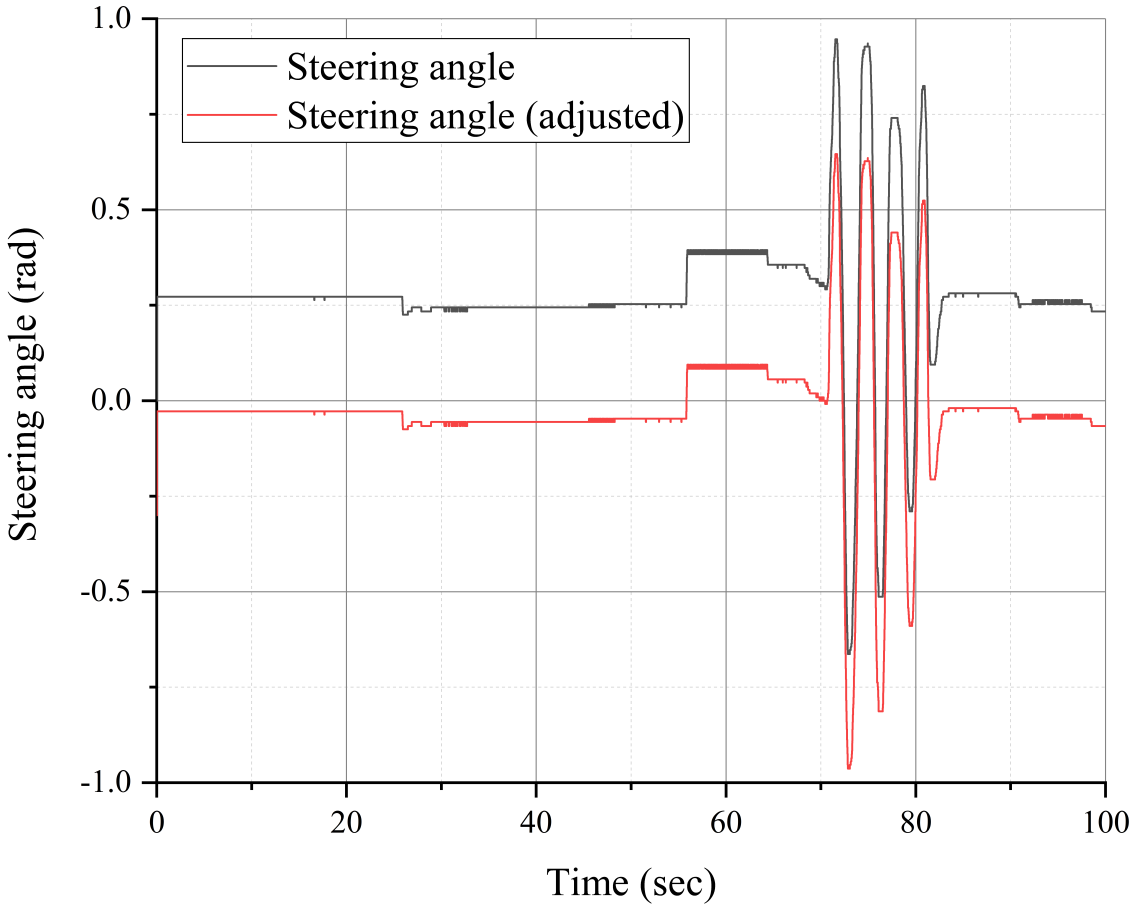

FIGURE 6.14: Steering angle sensor installed in the vehicle.

The set of data presented in Figure 6.15 is collected from slalom steering with the baseline vehicle set up. When introducing a manual offset, it is possible to avoid over/undershoot in the desired model caused by the steering angle error as per Figure 6.15. The offset is adjusted by studying the desired yaw rate. As displayed in Figure 6.15, there is a clear initial step error for the desired yaw rate with no offset, compared to when the offset is introduced. To find the accurate offset for this set of data, the desired model was closely studied at the time instance 70-73 seconds and 82-85 seconds, whereas the initial error at start of maneuver should closely relate to the measured yaw rate.

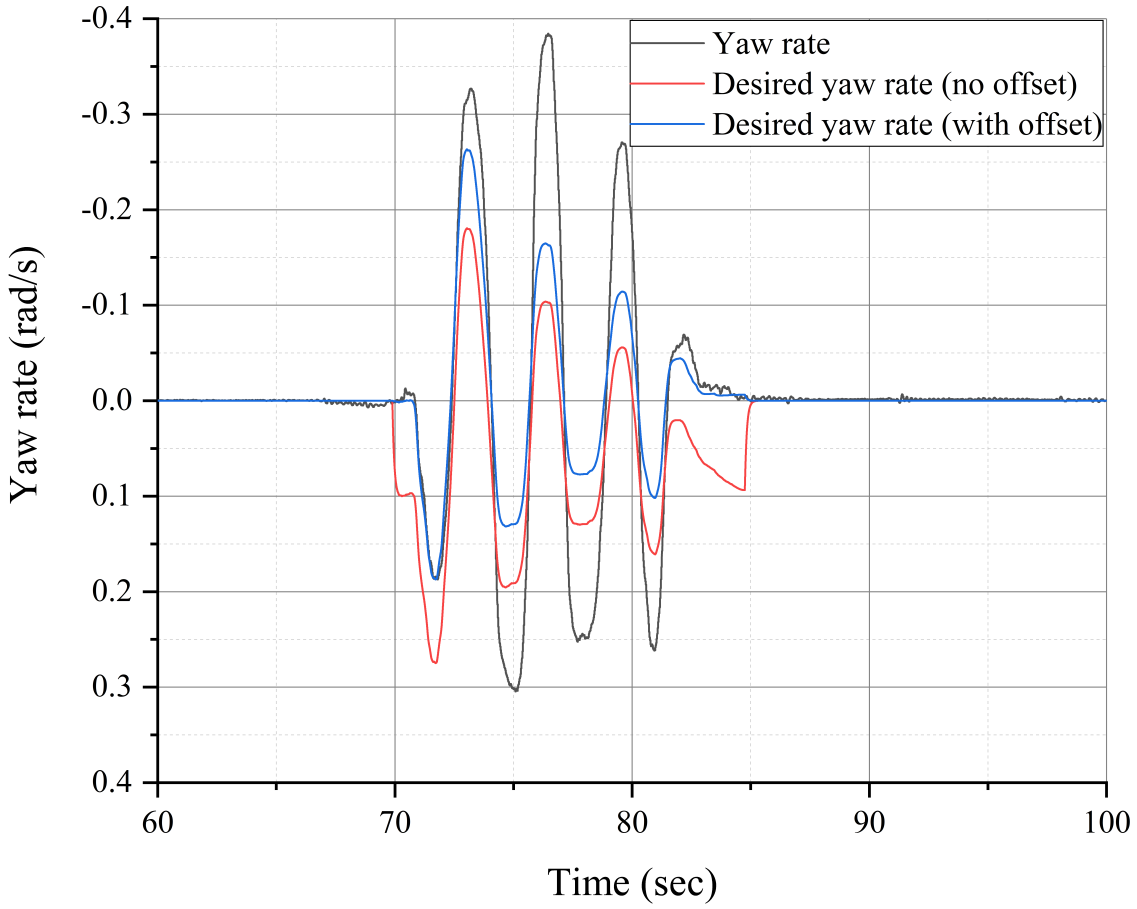

FIGURE 6.15: Yaw rate with steering angle offset.

6.5.2 Tyre Cornering Stiffness Estimation

In the simulation model in Chapter 3 and in [96], the tyre cornering stiffness was estimated using tyre data available in Siemens Amesim^{TM} and the Magic Tyre Formula. In order to estimate tyre properties which better correlates with the vehicles real tyres, data from steady-state cornering is required.

Steady-state cornering is studied by driving the vehicle following a circular path with a constant radius on a flat surface. By changing the longitudinal velocity, the change in lateral acceleration and yaw rate, the sideslip angle can be studied. In a steady-state maneuver, the yaw velocity is constant for given longitudinal velocity and as such the cornering stiffness can be estimated from the slope of the lateral force versus the sideslip. However, as described in Section 1.5, the lack of resources made this impractical.As such,

the cornering stiffness had was tuned via post-processing of experimental data and compared to literature.

6.5.2.1 Tuning Parameters for Cornering Stiffness

The solar car is equipped with radial tubeless Bridgestone Ecopia Ologic tyres, which are custom made for solar racing. With a diameter of 55.7 mm and width of 98 mm, these tyres are closer in resemblance to motorcycle tyres in terms of sizing. In [107] the experimental results for a motorcycle tyre with the vertical load of 1400 N has a cornering stiffness of 410 N/deg. From the measurements recorded during the weighing of the car, it is possible to approximate the cornering stiffens.

TABLE 6.2: Axial load at the wheels

Location	Front		Rear	
	Right	Left	Right	Left
Weight (N)	1,098	1,001	1,177	961

In addition, when the vehicle drives in a steady state, the data collected from driving should correlate closely with the bicycle model. This would mean that the collected yaw rated data should be close to the desired yaw rate during lower velocities, since the vehicle is within its linear region.

By adjusting the cornering stiffness in increments, it was found that $C_f = 380N/deg$ and $C_r = 390N/deg$ correlates with research data presented in [107] and in approximation to the vertical load in Table 6.2, as well as monitoring the behaviour of the desired yaw rate in Figure 6.16. The inability to maintain constant velocity during the maneuvering and the road bank angle, makes an exact match difficult to achieve. For future work, it is recommended to estimate the tyre cornering stiffness using the more conventional method of steady state circular trajectory.

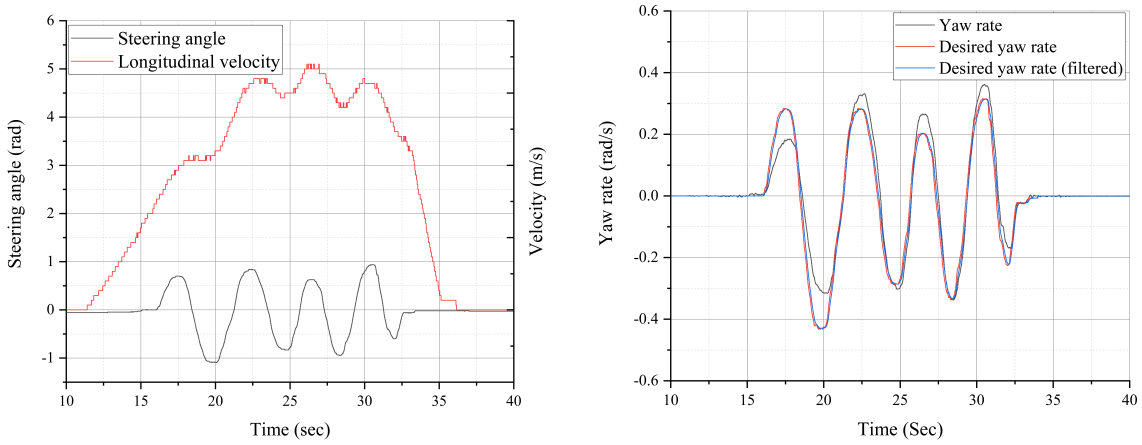

FIGURE 6.16: Steering angle and velocity, comparison of desired yaw rate and measured yaw rate for cornering stiffness estimation.

Chapter 7

Real-Time Driving

This chapter presents the real-time, real-life testing which was performed at the University of Technology Sydney, Tech Lab, Botany.

Due to the impact of COVID-19 as mentioned in Section 1.5, the adverse test area was a major cause of the limitations for the control validation. The test area is limited in size, in combination with the size of the vehicle and its turning circle, it is not possible to perform fishhook, lane change or circular trajectory testing without risk of human, hardware or property injury/damage. In addition, due to the limited length of the track, it is not safe nor possible to perform any high speed maneuvers, as well as apparent difficulties in achieving high enough constant velocity during maneuvering.

Although compensation of road and chassis angles have been included in the strategy, the reference models does not account for this when considering a steady state cornering test.

The road bank angle, sensor inaccuracies and offsets are reflected on the results in this chapter. As such, the control strategy will not be enabled. However, data attained, which was used for parameter estimation and tuning in Chapter 6, can also be used to examine the control viability.

7.1 Control Evaluation

The control evaluation is performed in an open loop setting, meaning that the control strategy runs in parallel with the original driver control. As such, there is never an input to the system by the controller. However, the real life driving allows for the study of the driver and vehicle behaviour, and importantly that the assistive yaw moment and torque are assured to be within a safe range if the control strategy is to be enabled in future works.

The vehicle is driven in a slalom maneuver, at a close to constant velocity during maneuvering and with the control initiating above a velocity of 2 m/s. It is deemed that velocities below 2 m/s are safe enough for cut-off, as the vehicle would be within its stability region. In addition, for the purpose of control evaluation, steering maneuvering is only performed as the vehicle has reached a high enough velocity for the control to be enabled. The cut-off velocity was introduced to avoid control output irregularities caused by noise and to avoid division by small numbers in the control algorithm.

The test scenarios in this section have been summarised as per Table 7.1.

TABLE 7.1: Real-time test scenario ID and description.

ID	Description
00_baseline	Baseline vehicle, all tyres 65, PSI velocity < 5 m/s
02_65PSI	All tyres 65 PSI, velocity > 5m/s
08_65PSI_P	All tyres 65 PSI, with passenger
01_45PSI	All tyres 45 PSI

7.2 Baseline Vehicle

7.2.1 Baseline: 65 PSI, Low Speed

The baseline vehicle considers a low speed (longitudinal velocity < 5 m/s) slalom maneuver, where all four tyres have an equal tyre pressure of 65 PSI. By examining a lower velocity,

it allows for the adjustment of the tyre cornering stiffness, which was detailed in Section 6.5.2.1.

The longitudinal velocity in Figure 7.1.a indicates that the control is enabled at approximately 15.5 seconds, whereas the steering angle in Figure 7.1.b indicates that the maneuver commence at 16 seconds. There is a steering angle offset which has been compensated for in the beginning of the maneuver. However, there is a small offset present upon termination of the maneuver. These offsets, due to bracket plasticity, and their impact on the desired model were discussed in Chapter 6, Section 6.5.1.

The estimated sidelslip in Figure 7.1.c indicates the largest peak occurs just after 20 seconds, which correlates the steering action in Figure 7.1.b. The sideslip angle is significantly larger than expected and does not flutter about the zero. This indicates that both error and drift have been introduced to the estimation due to accumulative effect of such error. Examining Figure 7.1.c, it can be found that the sideslip as the control action is disabled at the time instance 33 seconds, is about -0.3 radians, which is a relatively large offset as the true value should be reaching zero at lower velocities.

Since the sideslip is estimated based on the lateral acceleration, the longitudinal velocity and the yaw rate, there are three sources of error. The yaw rate is of little concern as the yaw rate is not heavily impacted by the road bank angle, as well as the raw data in Figure 7.1.d correlating well with the steering action at a reasonable magnitude. The two main concerns of error are due to (i) non-constant velocity as per Figure 7.1.a and (ii) offset error in the lateral acceleration due to the road bank angle. Since the observer considers the steady state cornering of the bicycle on a flat surface, a more detailed model is required for more accurate estimation on road bank angle. Plausible solutions to sideslip estimation error and drift is further discussed in Chapter 9.

Figure 7.1.d shows the raw yaw rate data recording in comparison to the desired yaw rate, filtered and unfiltered. In this baseline vehicle, it is expected that the desired yaw rate should be a close match to the vehicle's yaw rate. Since the desired model is derived from the linear bicycle model, which considers a constant velocity on a flat surface, a certain degree of error is to be expected due to the test area. This is also expected during the time range 16-22.5 seconds, as the vehicle is undergoing relatively large acceleration compared

to the remainder of the maneuver. The undesired offset in the steering angle sensor is expected to introduce a slight error, particularly in the beginning and towards the end of the manoeuvre. This produces a small step error at the end of the maneuver as the desired yaw returns to zero while the vehicle velocity is below 2 m/s. In terms of the desired yaw rate, the magnitude is small enough to be neglected since the raw yaw rate is a close match as per Figure 7.1.d.

The controller peaks correlate with the peaks of steering angle in Figure 7.1.b and the desired yaw rate in Figure 7.1.d, during the time range 18-22 seconds and 28-32 seconds. In Figure 7.1.e, the assistive yaw moment is displayed, which indicates that the MPC produces a slightly larger moment than the SMC. This is directly reflected on the torque in Figure 7.1.f, where the MPC produce a slightly larger torque. In general, the MPC is requesting a larger effort to reach the reference yaw rate compared to the SMC. The more apparent deviations between the the MPC and SMC is at the end of the manoeuvre. The MPC produces a relatively smooth transition which is desired, whilst the SMC is abruptly cutting off at approximately 1 Nm. The steering offset has previously been found to produce these type of cut-offs in the desired yaw rate which was discussed in Chapter 6. However, since the steering angle also is an input to the system matrix, this would reflect on the controller behaviour. Overall, there is a fine difference between the two control methods; however, the MPCs ability to handle the sensor errors and offsets is an advantage.

These results do not necessarily reflect the correct action of either of the controllers under study due to it being performed in an open-loop since the control action is not applied to the system. Nonetheless, the comparison of the controllers effort when unchanged real-time data is processed and estimation error is present makes it possible to evaluate if the control action is appropriate and safe to be enabled in future works. The evaluation of this baseline vehicle setup indicates that since the torque is relatively low and evenly distributed, it should be considered safe enough for closed-loop testing even if estimation error for sideslip and sensor error is present. It is however desired that the sideslip estimation and sensor errors are rectified and evaluated prior a closed-loop testing for more accurate representation.

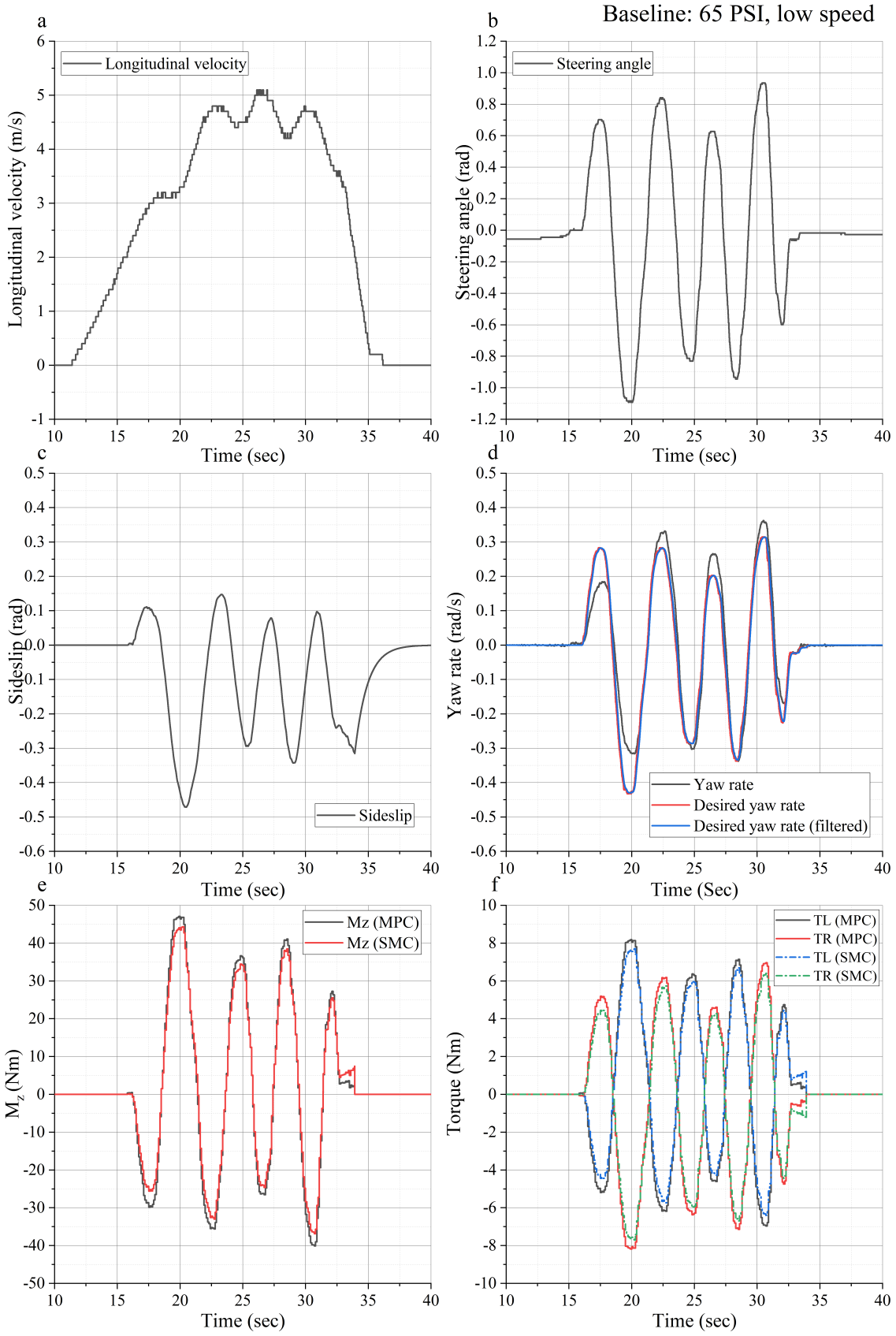

FIGURE 7.1: Baseline vehicle displaying a) longitudinal velocity b) steering angle c) measured yaw rate versus desired yaw rate d)sideslip e) corrective yaw moment M_z f) assistive torque

7.3 Condition Variation to Baseline Set-Up

In this section, the vehicle remains in the baseline vehicle set-up. However, the conditions surrounding the tests change. In the firs part, a larger velocity case is presented and in the second part a passenger is introduced.

7.3.1 65 PSI With Velocity > 5 m/s

The baseline vehicle in Section 7.2.1 considered a longitudinal velocity < 5 m/s whilst performing a slalom maneuver, with all four tyres of an equal tyre pressure of 65 PSI. In this section, the test is repeated with a higher velocity to examine if there are deviations between the raw yaw rate and the desired yaw rate.

The longitudinal velocity in Figure 7.2.a indicates that the control strategy is enabled approximately at the instant 70 seconds and the steering angle in Figure 7.2.b indicates that the maneuver commence closely thereafter. The first steering action is performed at a velocity of 4 m/s and steering angle 0.65 rad, which is within the range of velocity and steering angle for the baseline vehicle in Figure 7.1. The steering angle offset has been accommodated for in the beginning of the maneuver. However, there appears to be a small offset present upon termination, which is of similar magnitude to the baseline test.

Although the velocity is not constant for the baseline vehicle in Figure 7.1.a, there is a close to constant velocity during the maneuvers starting from the instant 22.5 seconds. Whilst the increased velocity in Figure 7.2.a experiences less even continuity during the maneuvers, which may be a reason why the sideslip drift in Figure 7.2.c is more conspicuous. Although the velocity is one culprit, it cannot be excluded that the increased drift is not due to lateral acceleration offsets or change in location center of gravity.

Evidently, there is a larger deviation between the desired yaw rate and measured yaw rate when the velocity is increased as per Figure 7.2.d, when compared to the baseline vehicle in Figure 7.1.d. This implies that due to the increased velocity, the vehicle is deviating from steady state handling for the current velocity, which is likely due to the tires reaching their linear limit. In Figure 7.2.a, at the time instance 70-75 seconds, the

vehicle is undergoing relatively large acceleration, from 2 m/s to 6 m/s. At the same time, the driver is performing the large steering actions per Figure 7.2.b. As a result, the desired yaw rate in Figure 7.2.d at this time is relatively large in comparison to the remainder of the maneuver. However, there is a closer match between the desired yaw rate and the measured one indicating that the vehicle is within its linear region. Comparing the desired yaw rate in Figure 7.2.d with the baseline in Figure 7.1.d, its evident that the desired yaw rate is smaller even though the velocity is higher. This is due to the smaller steering action in Figure 7.2.b in comparison to Figure 7.1.b, which indicates that the steering angle affects the desired yaw rate more than the velocity. In terms of the raw yaw rate, the higher velocity produces a higher yaw rate even though the steering action is less evasive. The offset in the steering angle in Figure 7.2.d produces a stable offset towards the end of the manoeuvre until the vehicle reaches the control cut-off at 2 m/s .

In terms of the assistive yaw moment and torque in Figures 7.2.e and 7.2.f, the peaks correlate well with the steering angle and consequently desired yaw rate peaks. Due to the smaller steering angles, the torque output does not reach the same magnitude as the baseline vehicle in Figure 7.1.e and 7.1.f, even if more significant drift of sideslip is present for this test. This indicates that the sideslip drift does not vastly impact the controller performance. Similar to the baseline vehicle however, the sideslip offset in combination with the steering angle offset are the cause of the controller peaking at the end. Once again there is just a fine difference between the two control methods. However, the MPC ability to handle the sideslip error is favourable.

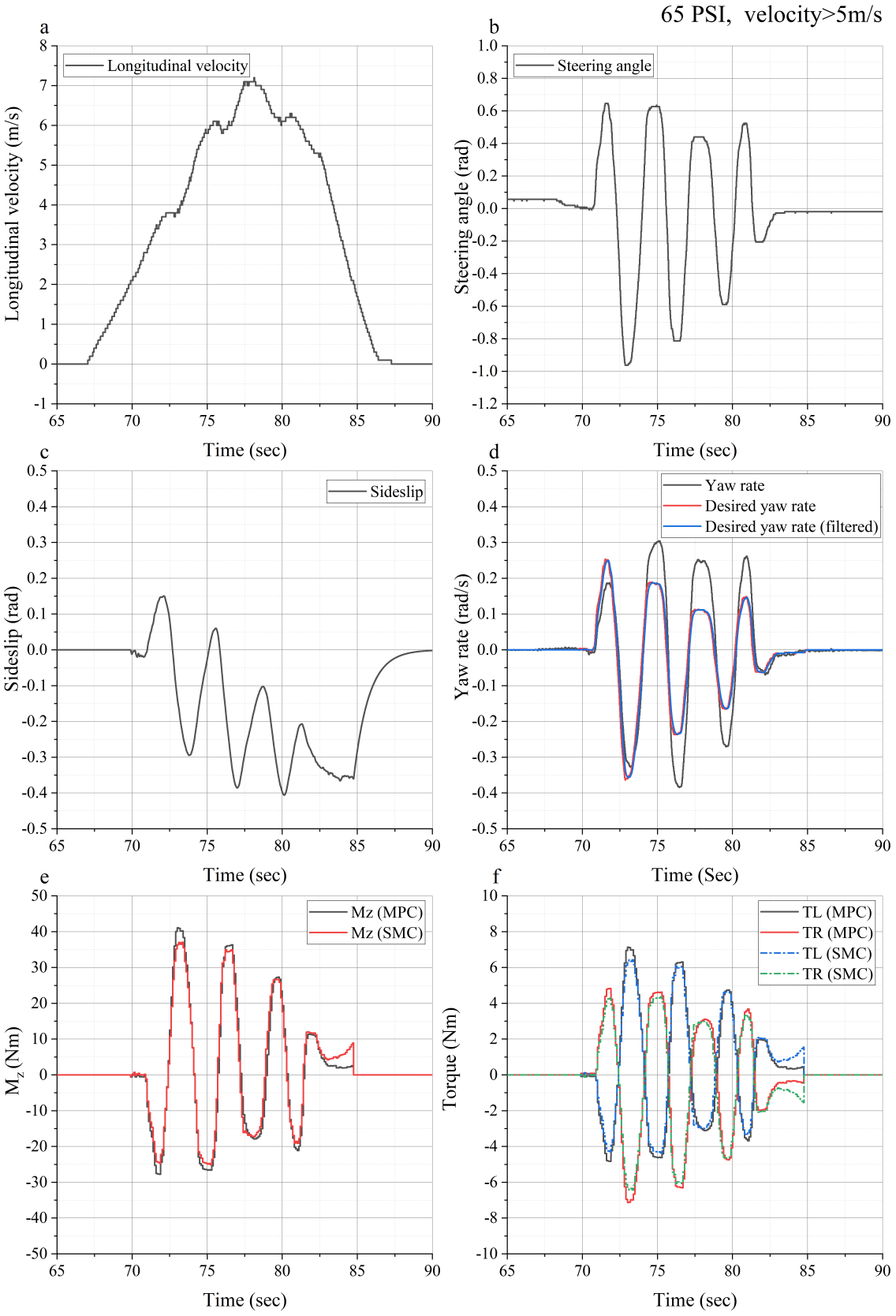

FIGURE 7.2: All four tyres with 65 PSI with velocity >5m/s displaying a) longitudinal velocity b) steering angle c) measured yaw rate versus desired yaw rate d)sideslip e) corrective yaw moment M_z f) assistive torque

7.3.2 65 PSI With Passenger

The baseline vehicle in Section 7.2.1 included only the driver whist performing slalom maneuver, with all four tyres presents an equal tyre pressure of 65 PSI. In this section, the test is repeated with driver and passenger.

The longitudinal velocity in Figure 7.3.a indicates that the control strategy is enabled approximately at 11 seconds. The steering angle in Figure 7.3.b indicates that the maneuver commence closely thereafter. The first steering action is performed shortly thereafter at a range which correlates better with the +5 m/s velocity test in Figure 7.2.b closer than the steering actions for the baseline vehicle test in Figure 7.1.b.

The velocity during the initial steer is above 4 m/s, which is larger than both the previous tests and would be the cause of a larger initial peak in sideslip as per Figure 7.3.c. Similar to Figure 7.2.c, there is a significant drift in sideslip compared to the baseline vehicle in Figure 7.1.c. Although the longitudinal velocity is changing at a similar rate as Figure 7.1.a, the drift error in Figure 7.2.c is likely due to the change in center of gravity caused by the additional passenger.

It is clear that Figure 7.3.d shows a deviation between the desired and measured yaw rate, which is similar to when the velocity was increased in Figure 7.2.d. In this case however, this is partially due to the miss-match in the model since additional mass has been introduced whilst the model use its original parameters. This means that the desired model produces the desired yaw rate for a vehicle with the same set-up as the baseline vehicle. The increased mass does not only impact the overall weight, but also causes a location change in the center of gravity and the tyre properties. Recalling, the simulation of load variation from Chapter 5, Section 5.2.2.1 where vehicle parameter sensitivity was studied, Figure 5.15 shows that the change in vehicle parameters cause phase shift in the yaw rate. Looking closely at Figure 7.3.d there is a clear phase shift in raw yaw rate, as the vehicles parameters have changed, in comparison to the desired yaw rate which considers the original parameters.

In terms of the assistive yaw moment and torque in Figure 7.3.e and 7.3.f, the peaks correlate well with the steering angle and consequently the desired yaw rate peaks. Due

to the smaller steering angles, the torque output does not reach the same magnitude as the baseline vehicle in Figure 7.1.e and 7.1.f, which is similar to Figure 7.2.e even if a more significant drift of sideslip is present. The more notable difference between the two previous test is the reduced error offset towards the end of the manoeuvre for the yaw moment in Figure 7.3.e and consequently the torque in Figure 7.3.f. As previously noted, the MPC is able to handle the offset errors better than the SMC. Although the SMC provides a smaller peaking assistive yaw moment in Figure 7.3.e compared to the baseline vehicle in Figure 7.1.e, the MPC produces a far better response.

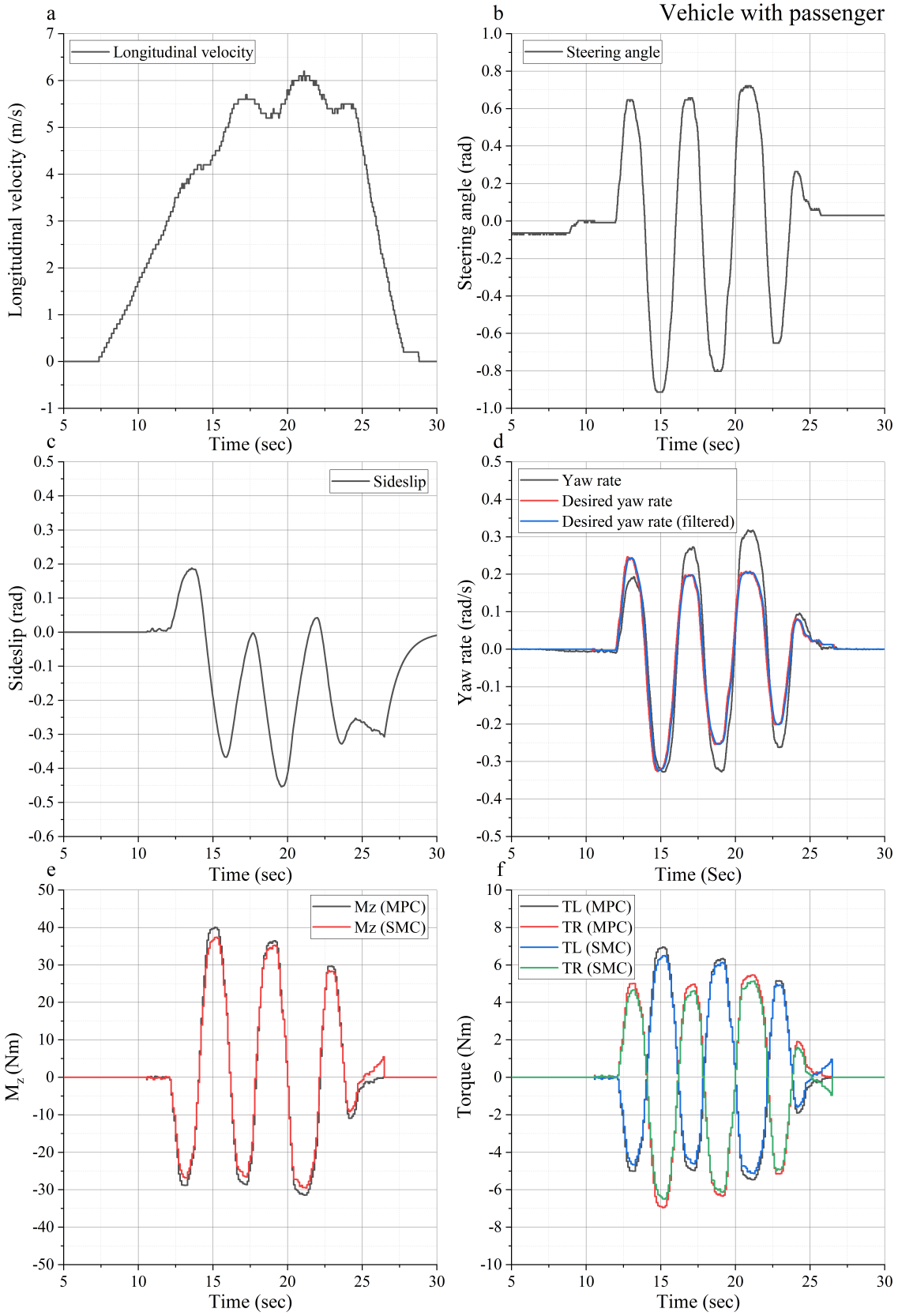

FIGURE 7.3: Vehicle with passenger displaying a) longitudinal velocity b) steering angle c) measured yaw rate versus desired yaw rate d)sideslip e) corrective yaw moment M_z f) assistive torque

7.4 Low tyre pressure

In this section two cases of low tyre pressure is presented. These results are compared and discussed in regards to the the baseline vehicle test as presented in Section 7.2.1. The baseline vehicle in Section 7.2.1 included only the driver whist performing slalom maneuver, with all four tyres of an equal tyre pressure of 65 PSI. In this section, the same test is replicated, but with a tyre pressure of 45 PSI.

7.4.1 Tyre pressure: 45 PSI

The longitudinal velocity in Figure 7.4.a indicates that the control action is enabled prior to 200 seconds, whilst the steering maneuver commences after 200 seconds, as per Figure 7.4.b. As such, the steering adjustments in that time frame are reflected in the sideslip estimation in Figure 7.4.c, the control output in Figure 7.4.d and 7.4.e. However, the desired yaw rate is not as affected as depicted in Figure 7.4.d. Nevertheless, the offset error towards the end of the maneuver is causing more obvious offsets for the desired yaw rate and the control action. In comparison to previous studies the steering offset is much larger for this test. This is likely owing to the force required by the driver as the steering becomes heavier when the tyre pressure is reduced, causing undesired flex in the steering angle sensor bracket.

The sideslip drift in Figure 7.1.c is consistent with the results in Section 7.2.1 and Section 7.3. However, the offset is prolonged further than in the previous tests. The deceleration of longitudinal velocity in Figure 7.1.a, Figure 7.2.a and Figure 7.3 is considerably steeper than in Figure 7.4.a. The much lower deceleration velocity of -0.5 m/s, clearly indicates that there is a link between the rate of deceleration and prolonged sideslip error offset.

Despite the longitudinal velocity being relatively close to the baseline test, the desired yaw rate in Figure 7.4.d does not present a close match to the raw yaw rate as the match observed in Figure 7.1.d. This is because the reduced tyre pressure cause a further missmatch in the estimated tyre cornering stiffness. Although there is a raw yaw rate present at the end of the maneuver, there is a clear offset caused by the steering angle offset.

The steering angle offset is reflected in both the assistive moment in Figure 7.4.e and the torque in Figure 7.4.f. However, considering that there is a slight yaw present, and the torque is below 1 Nm, this is not a major cause of concern. Overall both controllers behave very similar to the previous tests, with the MPC providing an overall larger moment but less offset when estimation error is present. Despite this having larger miss-match and uncertainty introduced than the previous test, there are no sizable or erratic outputs by the controller, which reinforces that the control can be enabled in future tests.

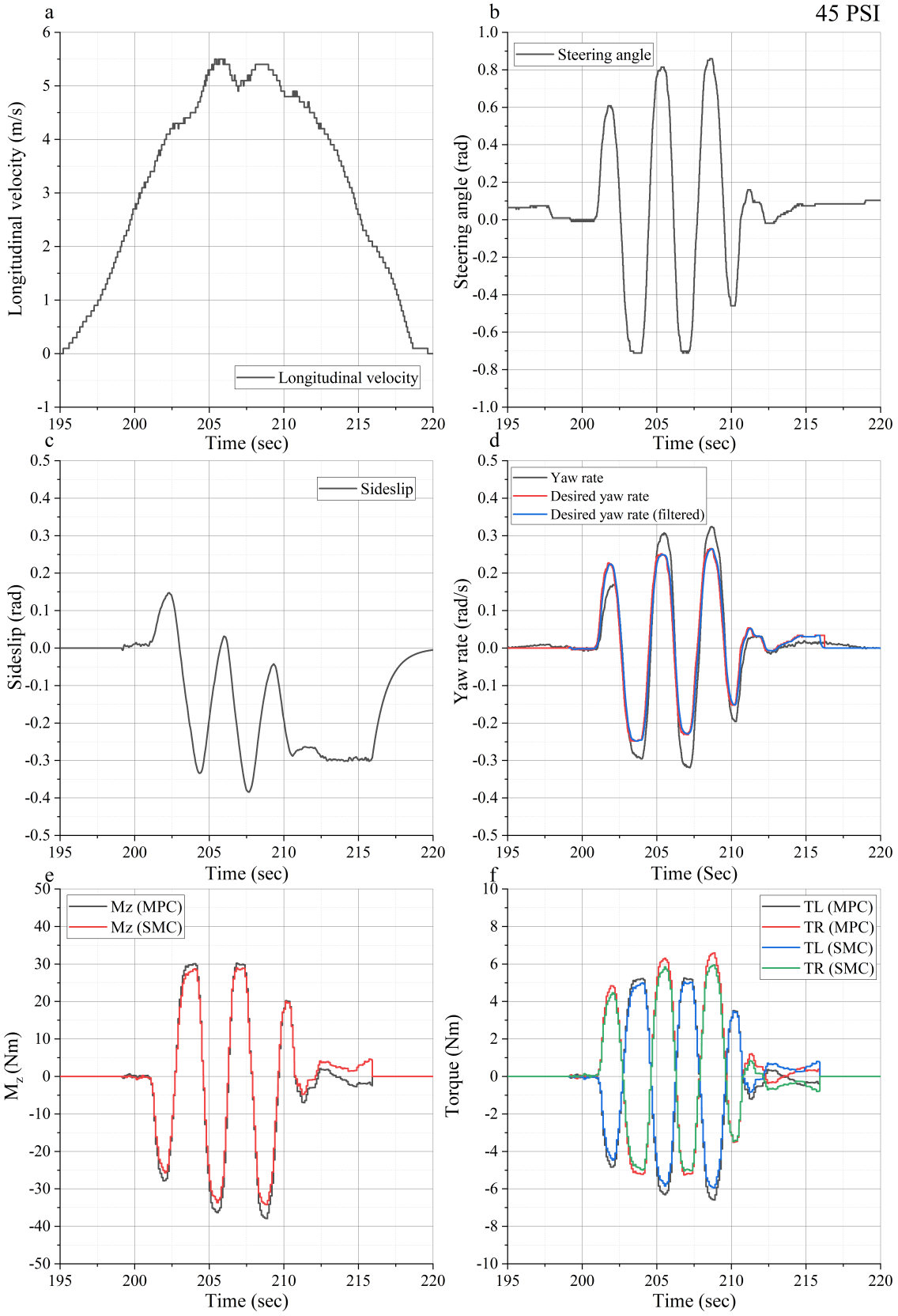

FIGURE 7.4: Low tyre pressure test: 45 PSI, displaying a) longitudinal velocity b) steering angle c) measured yaw rate versus desired yaw rate d) sideslip e) corrective yaw moment M_z f) assistive torque.

Chapter 8

Model Validation

In Chapter 5, the Siemens Amesim^{TM} iCar model was used to simulate the solar car behaviour. These models did not account for the measured parameters as presented in Chapter 6, due to the pressed time frame caused by COVID-19. As such, in this section the vehicle model has been updated and the simulated results are compared to the real-time data for the baseline vehicle as presented in Chapter 7, Section 7.2.1.

8.1 Simulation Adjustments and Limitations

Tyre cornering stiffness may not be an exact match due to the use of Magic Formula, based on the tyre properties. These had to be adjusted in steps in order to find a reasonable suitable correlation. The cornering stiffness is adjusted to match the one estimated for the real vehicle in Chapter 6. However, other properties related to the tyre were unattainable.

8.2 Simulation Model Comparison

The baseline vehicle considers a low speed (longitudinal velocity < 5 m/s) slalom maneuver, where all four tyres have an equal tyre pressure of 65 PSI as presented in Chapter 7, Section 7.2.1. In the results presented in Figure 8.1, the results from Chapter 7, Section 7.2.1 are

presented together with simulated results where the vehicle is using the real-time steering angle data as per Figure 8.1.b, whilst main tainting a constant velocity as per Figure 8.1.a.

As stated in Chapter 7, Section 7.2.1, the sideslip angle for the real testing is significantly larger than expected, which is supported by results in the simulation. When the vehicle is within a controllable limit, the magnitude of the sideslip angle is in general remarkably less than the yaw rate magnitude. Both simulated and real-time test sideslip were estimated using the same method. Recalling Chapter 3, Section 3.2, Siemens Simcenter Amesim^{TM} super-component allows for sensor measurement of the sideslip. The simulated result was performed with both the measured and estimated sideslip. Since both data were identical, the measured one was excluded from the results in Figure 8.1.b. This is an excellent example how the observer is affected by uncertainty caused by real world testing and further highlights the need of additional considerations in terms of testing and/or observer design.

The resulting simulated yaw rate is a very close match to the measured yaw rate, unlike the larger mismatch during real testing. This highlights how real-time testing is affected by unideal testing conditions and non-constant velocity, requesting larger desired yaw rate despite lower velocity.

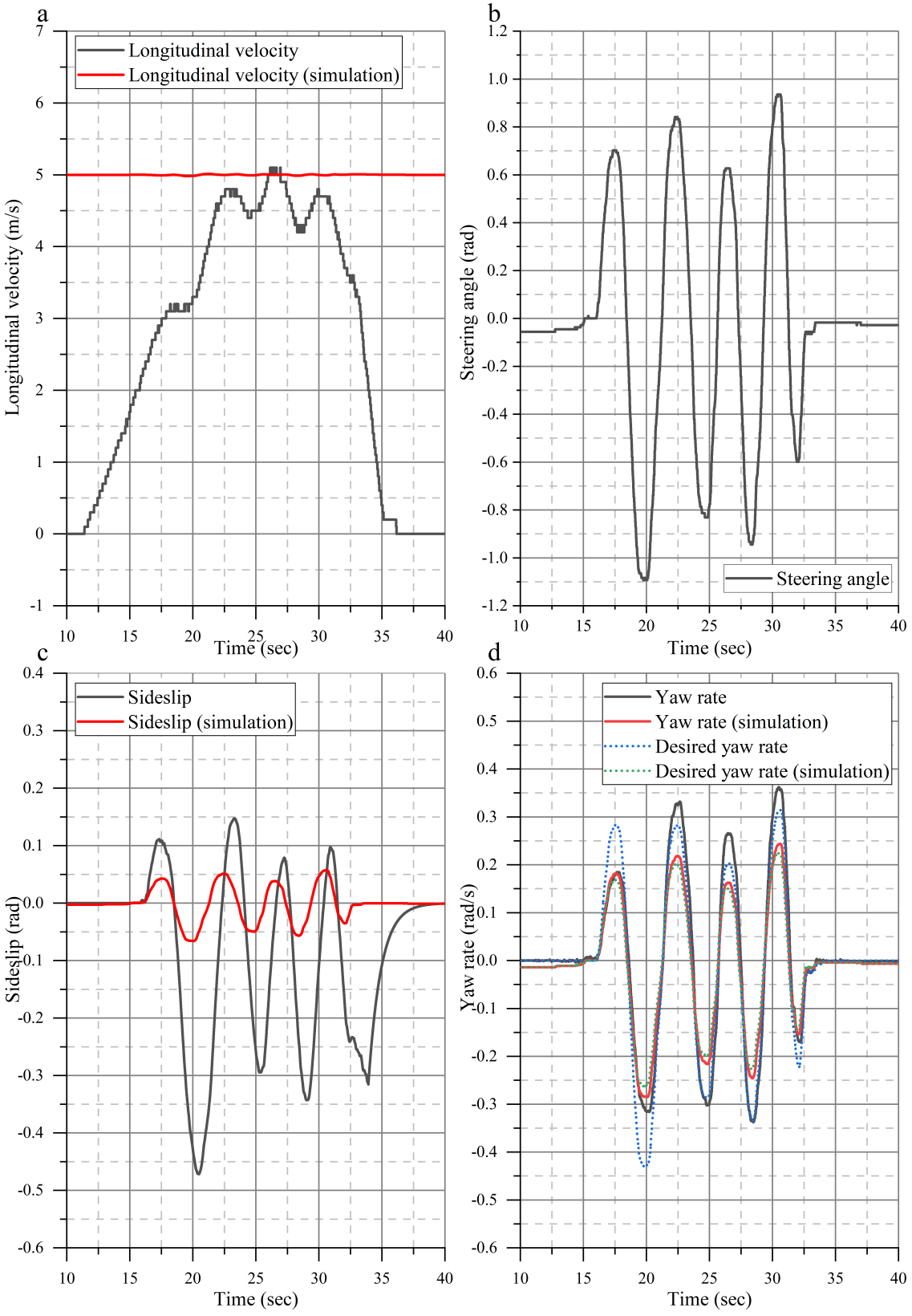

FIGURE 8.1: Comparison between baseline vehicle and simulation. Displaying a) Longitudional velocity, b) steering angle, c) Sideslip angle and d) yaw rate.

8.2.1 Influence of MPC

In this section, the response of the open-loop real-time MPC test is compared to the closed-loop simulated MPC. For the open-loop real-time test case, the prediction horizon was reduced in order to remove accumulative prediction error caused by sensor noise and dubious test circumstances. The control set-up for the real-time test vehicle was applied to the simulated vehicle in order to study the control influence.

As per Figure 8.2, the two torques respond in a similar manner, with the discrepancy of the magnitude. However, the lower magnitude for the simulation is more likely due to a more ideal test scenario and as of being a closed-loop case compared to an open-loop. Despite the real-time test vehicle experiencing a drift in sideslip estimation, no phase-shift or large influxes are visible in comparison to the simulated vehicle with a more ideal sideslip estimation.

The simulated control does not have a velocity cut-off limit at 2 m/s as the velocity remains constant, which produce a slight input at the beginning of the maneuver due to steering wheel adjustments. The small input supports that the cut-off velocity does not affect the overall function of the control.

Both the torque for the simulated vehicle and the real-time test have a slight peak at the end of the maneuver, which disclose that the error in the steering angle sensor may be a larger culprit than a large offset and drift in the sideslip estimation.

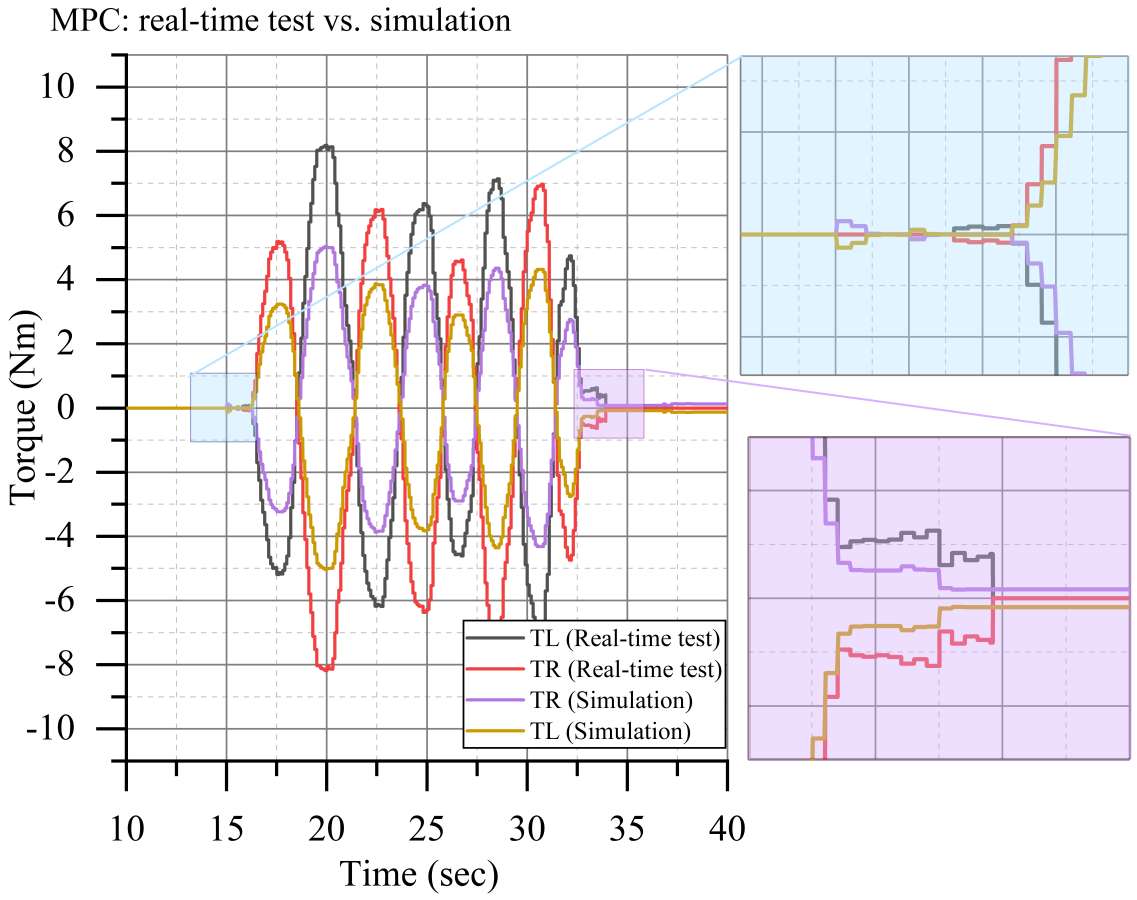

FIGURE 8.2: Closed-loop control in simulation vs. open-loop real-time test, torque output provided by the MPC strategy.

In terms of the yaw rate in Figure 8.3, there are only marginal improvement in yaw rate. This is due to transferring an open-loop control into a closed-loop setting. This would imply that the controller might require tuning to match the updated vehicle parameters. However, this being said, the reference yaw rate in comparison to the measured yaw rate for the simulated vehicle is already a very close match. This is owed to the study of the baseline vehicle, where it should be expected to be a close match due to being within reasonably stable conditions.

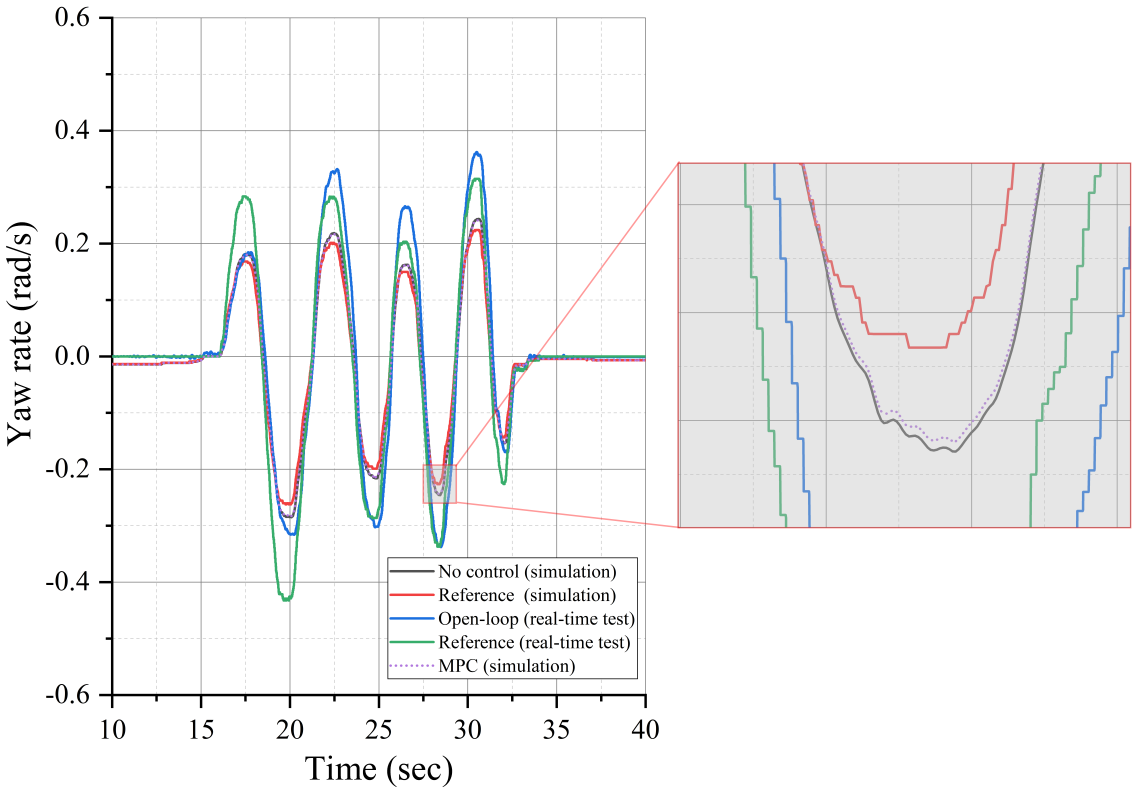

FIGURE 8.3: Impact of MPC on yaw rate: closed-loop control in simulation vs. open-loop real-time test.

Chapter 9

Conclusion and Future Work

In this thesis, control strategies were developed for the purpose of applying an assistive yaw moment to a customised solar-electric vehicle, by allocating torque to the rear in-wheel motors. In this chapter, the contributions, conclusions and future work with recommendations will be presented.

9.1 Contribution

One of the prominent research gaps identified early on was that the solar car is unique due to its design parameters. Whereas literature studying lightweight vehicles are commonly fairly small, the solar car has a large chassis compared to its weight. Therefore, there is significant opportunity when it comes to real-time testing and data acquisition. This research has contributed as follows:

- Developed a simulation model of the ATN solar car
- Investigated the influence of load variation on the solar car
- Designed four control strategies to provide an assistive yaw moment.
- Investigating the influence of uncertainty over the controllers performance
- Engineering application – vehicle implementation

- Real-time testing
- Driver-in-the-loop
- Real data
- Correlate real-time and simulation phase lag in the desired model caused by additional weight
- Model validation
- Control evaluation – safe for implementation
- Increasing vehicle safety

9.2 Simulation

Since the vehicle development evolved and particularly following physical measurements and evaluation, it is clear that there was fairly large parameter discrepancies. Due to the limited time remaining of the candidature, re-evaluation of all prior simulations were impracticable.

Nevertheless, important findings were made whilst investigating (i) the influence in a change in load, (ii) the impact of only updating mass, rather than all parameters for the vehicle plant, and (iii) the performance of DYC strategies (DCC, SMC and PI control) for a loaded vehicle versus when only the driver is present. Unlike previous studies, this investigation was evaluated on an ultra-lightweight vehicle which experiences a high curb-to-load weight ratio.

This study was performed to highlight the dangers in vehicles with large changes in load-to-curb weight ratio, and particularly the effect of not considering the change in the internal parameters. Vehicles that are highly dependent on system information, such as autonomous vehicles, could be particularly sensitive to errors due to changes in loading conditions. If not appropriately considered and managed it can be a cause of detrimental outcomes.

9.3 Real-Time Testing

The experimental validation of this project was originally designed for track testing with ideal flat surface area. Due to the implication of COVID-19 and the limitations it imposed on this research, important areas such as the impact of road bank angle was not investigated until the experimental data analysis. The road bank angle compensation was previously out of scope for this research. However, due to the discrepancies detected, they had to be accounted for as presented in Chapter 6.

One of the drawbacks with the test scenarios was the ability to repeat the maneuvers for each test scenario. For the base vehicle, good tyre pressure and low velocity allows for a larger steering maneuver to be performed without particular effort from the driver. Whilst when velocity is higher, or uneven tyre pressure, the steering action needs to be reduced due to safety concerns by driver and as the steering action becomes relatively heavy particularly when the pressure of the steering tyres are low.

The steering wheel is relatively heavy even under ideal circumstances, as the solar car is designed to maintain mostly straight driving during the race. Due to this, the driver tended to shift in the seat whilst performing the maneuver, which in Chapter 7 was discussed as a point of error in sidelsip estimation due to shifts in center of gravity.

Although there were efforts of compensating for the road bank angle in the sideslip estimation, major drifts still appeared during the real-time testing scenarios in Chapter 7. These were traced to be due to accumulative errors caused by the integral stage in the estimator, which is likely to be because of a combination of non-constant velocity, offsets in the lateral acceleration and potentially the IMU location. As described in [26], drifts can occur due to misalignment of the IMU in comparison to the vehicle axes or if the sensor is not located at the center of gravity. Due to the solar cars light weight, the center of gravity is easily impacted and could be caused by the driver simply shifting in the seat. Although not registered, shifts did occur during testing, as mentioned earlier particularly those during heavy steering.

The main issue of the sideslip drift traces back to the testing and test area itself. This can be approached in two ways: (i) flat road testing or (ii) re-design the sideslip observer

to accurately account for road bank angles. Option (i) simply requires enough funds to be secured to allow for transportation of the vehicle, equipment, staff and other logistics for track testing. In terms of (ii), it is suggested that the skewed accumulation error may be significantly reduced by combining the model-kinematic method for sideslip estimation [66]. This will require additional theoretical work and testing, which is not within the time-frame of this thesis and has to be considered for future work.

Despite all these challenges, there are not major variations of the assistive moment produced by the SMC or the MPC. Which is an indication that regardless of the uncertainty surrounding the test bed as is, there are not no major concerns in allowing for closed loop testing with the assistive control enabled.

9.4 Model Validation

Due to the unfavorable test circumstances, it is difficult to completely validate the real-time test data with the simulated vehicle. The simulation was set for flat road testing which does not correlate with the bank angle in the real test scenario. It is also possible to maintain constant velocity in the simulation environment in comparison to the real test where the test area is too short to reach an adequate velocity.

Tyre data would be required to get a proper representation using the Magic Formula tyre model in the simulation. Although the slope BCD (3.8) and the normal force, F_z, were adjusted to accommodate the findings from Chapter 6, more data is required to give a more accurate representation of the solar car tires. In addition, due to the vehicles customised build, vehicle properties such as moment of inertia, chassis frequencies, suspension stiffness etc. were decided by calculated estimations based on available information. In order to get an even more accurate simulation model, comprehensive work is required with the purpose of obtaining data from the real vehicle. It should also be considered to evaluate the vehicle on flat road testing, which correlates well with the suggested approach to investigating the sideslip observer.

9.5 Future Work

This thesis has provided the foundation for future deployment of in-wheel yaw moment control on the ATN solar car. The control strategies in this research have been deemed safe for low speed tests in its current state.However, there are amendments which are recommended to be addressed as per the following section.

One of the flaws with this thesis was due to the limitation of the test area. As such, it is recommended to obtain an area which is flat and large enough to perform different maneuvers with fixed parameters in order to validate the vehicle steady state handling. By doing so it will be possible to observe the effect of various factors. For example an unchanged case can be used to compare the case of change in e.g. tyre pressure, mass variation or the affects of road bank angles on the observer and reference model, to draw a more systematic conclusions about the separate cases and controllers.

By performing a steady-state circular drive test, more accurate tyre data can be obtained, which can be used to improve the system model and aid in refined control tuning. If the road bank angle is eliminated, the sideslip observer can be investigated in its current design as well as giving the opportunity to investigate, and develop an observer that can better account for a road bank angle. Similarly, further research can be carried out into a system and reference models which account for road bank angles.

Lastly, it is also recommended to replace the steering angle sensor bracket to remove sensor error readings and to re-tune all sensors for testing.

If accurate data can be obtained, together with the closed-loop control performance, there is endless potential to more advanced control development.

Appendix A

Early simulation model

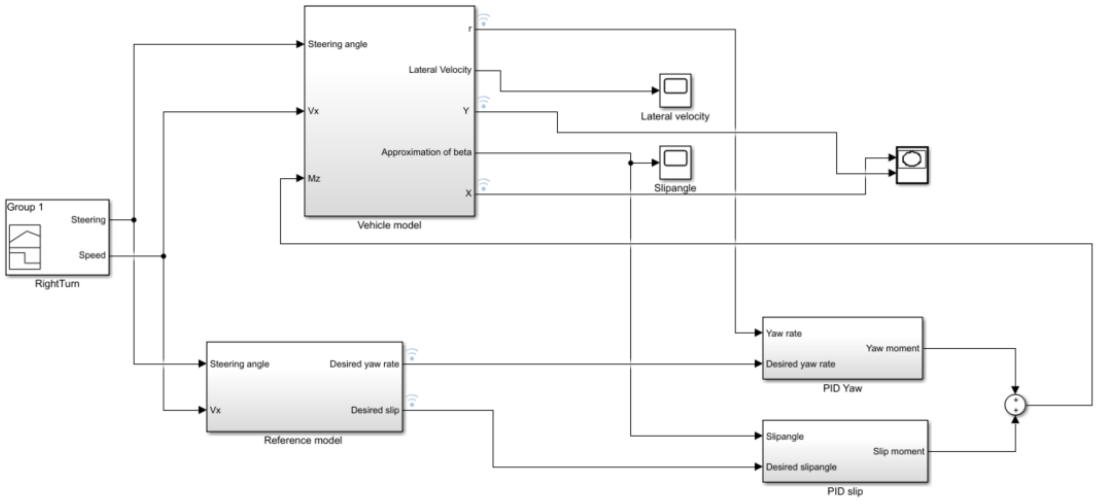

FIGURE A.1: Simple vehicle model used for early simulation.

Appendix B

Weight distribution data

Weight distribution data collected for center of gravity calculations.

Table B.1: Weight distribution data of the ATN solar car.

Case	$\mathbf{Weight_{FR}}$	$\mathbf{Weight_{FL}}$	$\mathbf{Weight_{RR}}$	$\mathbf{Weight_{RL}}$	Angle
Empty	76	81	104	85	0.00000
	76	82	104	84	0.01500
	74	81.5	103	84	0.03167
	73	81	105	86	0.04668
Driver	112	102	120	98	0.00000
	117.5	102	122	91	0.01500
	119	102	123	91	0.01500
	120	102	125	98	0.01667
Driver and passenger	129	141	125	104	0.00000
	138	146	126	105	0.01500
	141	145	127	105	0.01500
	138	146	131.5	111	0.01667

Appendix C

Sideslip observer

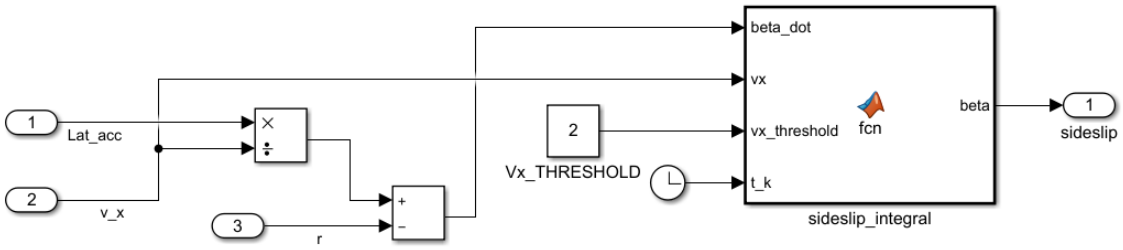

FIGURE C.1: Sideslip observer Simulink design

The integral using the persistent function as follows:

```
function beta = fcn(beta_dot, vx, vx_threshold, t_k)

persistent t_k_1
if isempty(t_k_1)
    t_k_1 = 0;
end

persistent accumulate
if isempty(accumulate)
    accumulate = 0;
```

```
end



DT = t_k - t_k_1;
if (vx>vx_threshold)
    accumulate = DT*beta_dot + accumulate;
else
    if(accumulate>=0)
        accumulate = (1-DT)*accumulate;
        if (accumulate<0)
            accumulate = 0;
        end
    else
        accumulate = (1-DT)*accumulate;
        if (accumulate>0)
            accumulate=0;
        end
    end
end

t_k_1 = t_k;

beta = accumulate;
```

Bibliography

[1] Wen Sun, JunNian Nian Wang, QingNian Nian Wang, Francis Assadian, and Bo Fu. Simulation investigation of tractive energy conservation for a cornering rear-wheel-independent-drive electric vehicle through torque vectoring. *Science China Technological Sciences*, 61(2):257–272, 2018. ISSN 1862281X. doi: 10.1007/s11431-017-9139-5.

[2] Florian Kohlhuber, M Lienkamp, and Peter E Pfeffer. Load problem of lightweight electric vehicles and solution by online model adaptation. pages 281–302, 2014. doi: 10.1007/978-3-658-05978-1_22.

[3] Pongsathorn Pongsathom Raksincharoensak, Sato Daisuke, and Mathias Lidberg. Direct Yaw Moment Control for Enhancing Handling Quality of Lightweight Electric Vehicles with Large Load-To-Curb Weight Ratio. *Applied Sciences (Switzerland)*, 9 (6), 2019. ISSN 20763417. doi: 10.3390/app9061151.

[4] Kyosuke Takekoshi, Yusuke Udagawa, and Taichi Shiiba. Robust Handling Performance Against Weight Variation for Light Weight Vehicle. In *Volume 12: Transportation Systems*. American Society of Mechanical Engineers, 11 2014. ISBN 978-0-7918-4961-3. doi: 10.1115/IMECE2014-39200.

[5] Milan Batista and Marko Perkovič. A simple static analysis of moving road vehicle under crosswind. *Journal of Wind Engineering and Industrial Aerodynamics*, 128: 105–113, 2014. ISSN 01676105. doi: 10.1016/j.jweia.2014.02.009.

[6] Alberto Parra, Asier Zubizarreta, Joshué Pérez, and Martín Dendaluce. Intelligent torque vectoring approach for electric vehicles with per-wheel motors. *Complexity*, 2018:1–14, 2018. doi: 10.1155/2018/7030184.

[7] M. De Santis, S. Agnelli, and O. Giannini. Torque vectoring system for improving manoeuvrability of light electric vehicles. *2017 AEIT International Annual Conference: Infrastructures for Energy and ICT: Opportunities for Fostering Innovation, AEIT 2017*, 2017-Janua:1–6, 2017. doi: 10.23919/AEIT.2017.8240575.

[8] M Vignati, E Sabbioni, D Tarsitano, and F Cheli. Electric powertrain layouts analysis for controlling vehicle lateral dynamics with torque vectoring. In *2017 International Conference of Electrical and Electronic Technologies for Automotive*, pages 1–5. IEEE, 2017. doi: 10.23919/EETA.2017.7993204.

[9] X Xie, L Jin, Y Jiang, and B Guo. Integrated dynamics control system with ESC and RAS for a distributed electric vehicle. *IEEE Access*, PP(99):1–11, 2018. doi: 10.1109/ACCESS.2018.2819206.

[10] Xiangkun He, Kaiming Yang, Yulong Liu, and Xuewu Ji. A Novel Direct Yaw Moment Control System for Autonomous Vehicle. In *SAE Technical Papers*, volume 2018-August. SAE International, 8 2018. doi: 10.4271/2018-01-1594.

[11] Leonardo De Novellis, Aldo Sorniotti, Patrick Gruber, Javier Orus, Jose-Manuel Manuel Rodriguez Fortun, Johan Theunissen, and Jasper De Smet. Direct yaw moment control actuated through electric drivetrains and friction brakes: Theoretical design and experimental assessment. *Mechatronics*, 26:1–15, 3 2015. ISSN 09574158. doi: 10.1016/j.mechatronics.2014.12.003.

[12] S Li, D Zhao, L Zhang, and Y Tian. Lateral stability control system based on cooperative torque distribution for a four in-wheel motor drive electric vehicle. In *2017 36th Chinese Control Conference (CCC)*, pages 1119–1123, 2017. doi: 10.23919/ChiCC.2017.8027497.

[13] E N Smith, E Velenis, D Tavernini, and D Cao. Effect of handling characteristics on minimum time cornering with torque vectoring. *Vehicle System Dynamics*, 56(2): 221–248, 2018. ISSN 0042-3114. doi: 10.1080/00423114.2017.1371771.

[14] Massimo Canale, Lorenzo Fagiano, Antonella Ferrara, and Claudio Vecchio. Comparing internal model control and sliding-mode approaches for vehicle yaw control.

IEEE Transactions on Intelligent Transportation Systems, 10(1):31–41, 2009. ISSN 15249050. doi: 10.1109/TITS.2008.2006772.

[15] Yu Cao, Li Zhai, Tianmin Sun, and Hongtao Gu. Straight Running Stability Control Based on Optimal Torque Distribution for a Four in-wheel Motor Drive Electric Vehicle. *Energy Procedia*, 105:2825–2830, 2017. ISSN 18766102. doi: 10.1016/j.egypro.2017.03.616.

[16] Dejian Han, Zhen Yan, Feng Xiao, and Shaokun Li. Development of an Advanced Stability Control System of 4WD Electric Vehicle with In-Wheel-Motors. *SAE Technical Papers*, 2016-April(April):1–7, 2016. ISSN 01487191. doi: 10.4271/2016-01-1671.

[17] Efstathios Siampis, Efstathios Velenis, and Stefano Longo. Rear wheel torque vectoring model predictive control with velocity regulation for electric vehicles. *Vehicle System Dynamics*, 53(11):1555–1579, 2015. ISSN 17445159. doi: 10.1080/00423114.2015.1064972.

[18] Sriharsha Bhat, Mohammad Mehdi Davari, and Mikael Nybacka. Study on Energy Loss due to Cornering Resistance in Over-Actuated Vehicles using Optimal Control. *SAE International Journal of Vehicle Dynamics, Stability, and NVH*, 1(2):263–269, 2017. ISSN 23802162. doi: 10.4271/2017-01-1568.

[19] Christoforos Chatzikomis, Aldo Sorniotti, Patrick Gruber, Matthew Bastin, Raja Mazuir Shah, and Yuri Orlov. Torque-Vectoring Control for an Autonomous and Driverless Electric Racing Vehicle with Multiple Motors. *SAE International Journal of Vehicle Dynamics, Stability, and NVH*, 1(2):338–351, 2017. ISSN 23802162. doi: 10.4271/2017-01-1597.

[20] Qinghua Meng, Chunjiang Qian, and Pan Wang. Lateral motion stability control via sampled-data output feedback of a high-speed electric vehicle driven by four in-wheel motors. *Journal of Dynamic Systems, Measurement and Control, Transactions of the ASME*, 140(1):1–8, 2018. ISSN 15289028. doi: 10.1115/1.4037266.

[21] Leonardo De Novellis, Aldo Sorniotti, and Patrick Gruber. Wheel torque distribution criteria for electric vehicles with torque-vectoring differentials. *IEEE Transactions on Vehicular Technology*, 63(4):1593–1602, 5 2014. ISSN 00189545. doi: 10.1109/TVT.2013.2289371.

[22] Basilio Lenzo, Aldo Sorniotti, Patrick Gruber, and Koen Sannen. On the experimental analysis of single input single output control of yaw rate and sideslip angle. *International Journal of Automotive Technology*, 18(5):799–811, 2017. ISSN 1976-3832. doi: 10.1007/s12239-017-0079-4.

[23] James Balkwill. *Performance Vehicle Dynamics : Engineering and Applications*. Elsevier Science & Technology, Saint Louis, UNITED STATES, 2017. ISBN 9780128126943. URL `http://ebookcentral.proquest.com/lib/uts/detail.action?docID=4986282`.

[24] Balazs Nemeth, Peter Gaspar, Daniel Fenyes, Jozsef Bokor, B Németh, P Gáspár, D Fényes, Jozsef Bokor, Balazs Nemeth, Peter Gaspar, Daniel Fenyes, and Jozsef Bokor. Robust control design for the integration of steering and torque vectoring using a variable-geometry suspension system. *Proceedings of the American Control Conference*, pages 291–296, 2017. ISSN 07431619. doi: 10.23919/ACC.2017.7962968.

[25] Takahiko Yoshino and Hiromichi Nozaki. About the effect of camber control on vehicle dynamics. *SAE Technical Papers*, 2014-Janua:1–10, 2014. ISSN 01487191. doi: 10.4271/2014-01-2383.

[26] Donald Selmanaj, Matteo Corno, Giulio Panzani, and Sergio M. Savaresi. Vehicle sideslip estimation: A kinematic based approach. *Control Engineering Practice*, 67 (June):1–12, 2017. ISSN 09670661. doi: 10.1016/j.conengprac.2017.06.013.

[27] Florian Kohlhuber and M Lienkamp. Online Estimation of Physical Vehicle Parameters with ESC Sensors for Adaptive Vehicle Dynamics Controllers. In *Internationales Stuttgarter Symposium Automobil-und Motorentechnik*, pages 157–175, 2013.

[28] Zhen Wei, John Xu, and Dunant Halim. Braking force control strategy for electric vehicles with load variation and wheel slip considerations. *IET Electrical Systems in Transportation*, 7(1):41–47, 2017. ISSN 20429746. doi: 10.1049/iet-est.2016.0023.

[29] X Huang and J Wang. Lightweight Vehicle Control-Oriented Modeling and Payload Parameter Sensitivity Analysis. *IEEE Transactions on Vehicular Technology*, 60(5): 1999–2011, 2011. ISSN 1939-9359. doi: 10.1109/TVT.2011.2148135.

[30] J C Limroth and Thomas Kurfess. Real-time vehicle parameter estimation and equivalent moment electronic stability control. *International Journal of Vehicle Design*, 68(1/2/3):221 –244, 2015.

[31] Xuewu Ji, Xiangkun He, Chen Lv, Yahui Liu, and Jian Wu. A vehicle stability control strategy with adaptive neural network sliding mode theory based on system uncertainty approximation. *Vehicle System Dynamics*, 56(6):923–946, 2018. ISSN 17445159. doi: 10.1080/00423114.2017.1401100.

[32] Enrico Regolin, Dzmitry Savitski, Valentin Ivanov, Klaus Augsburg, and Antonella Ferrara. Lateral vehicle dynamics control via sliding modes generation. *Sliding Mode Control of Vehicle Dynamics*, pages 121–158, 2017. doi: 10.1049/pbtr005e_ch4.

[33] J. Folgado, S. S. Valtchev, and F. Coito. Electronic differential for electric vehicle with evenly split torque. In *2016 IEEE International Power Electronics and Motion Control Conference (PEMC)*. IEEE, 9 2016. ISBN 978-1-5090-1798-0. doi: 10.1109/EPEPEMC.2016.7752167.

[34] Basilio Lenzo, Mattia Zanchetta, Aldo Sorniotti, Patrick Gruber, and Wouter De Nijs. Yaw Rate and Sideslip Angle Control Through Single Input Single Output Direct Yaw Moment Control. *IEEE Transactions on Control Systems Technology*, 29(1), 1 2021. ISSN 1063-6536. doi: 10.1109/TCST.2019.2949539.

[35] Y H Xu and M Ahmadian. Study on the performance of active front steering system. *International Journal of Automotive Technology*, 14(4):595–603, 2013. ISSN 1976-3832. doi: 10.1007/s12239-013-0064-5.

[36] Seong-Jun Park and Jeong-Hyun Sohn. Effects of camber angle control of front suspension on vehicle dynamic behaviors. *Journal of Mechanical Science and Technology*, 26(2):307–313, 2012. ISSN 1976-3824. doi: 10.1007/s12206-011-1206-1.

[37] Bekheira Tabbache, Abdelaziz Kheloui, and Mohamed El Hachemi Benbouzid. An Adaptive Electric Differential for Electric Vehicles Motion Stabilization. *IEEE*

Transactions on Vehicular Technology, 60(1), 1 2011. ISSN 0018-9545. doi: 10.1109/TVT.2010.2090949.

[38] Y. E. Zhao, J. W. Zhang, and X. Q. Guan. Modeling and simulation of electronic differential system for an electric vehicle with two-motor-wheel drive. In *2009 IEEE Intelligent Vehicles Symposium*. IEEE, 6 2009. ISBN 978-1-4244-3503-6. doi: 10.1109/IVS.2009.5164454.

[39] Edoardo Sabbioni, Federico Cheli, Michele Vignati, and Stefano Melzi. Comparison of Torque Vectoring Control Strategies for a IWM Vehicle. *SAE International Journal of Passenger Cars - Electronic and Electrical Systems*, 7(2):565–572, 2014. ISSN 19464622. doi: 10.4271/2014-01-0860.

[40] P Raksincharoensak, V Lertsilpachalern, M Lidberg, and R Henze. Robust vehicle handling dynamics of light-weight vehicles against variation in loading conditions. In *2017 IEEE International Conference on Vehicular Electronics and Safety (ICVES)*, pages 202–207, 2017. doi: 10.1109/ICVES.2017.7991926.

[41] Ma Haiying, Li Chaopeng, Wang Zhi Fu, Haiying Ma, Chaopeng Li, Zhi fu Wang, Ma Haiying, Li Chaopeng, and Wang Zhi Fu. Direct Yaw-Moment Control Based on Fuzzy Logic of Four Wheel Drive Vehicle under the Cross Wind. *Energy Procedia*, 105:2310–2316, 2017. ISSN 18766102. doi: 10.1016/j.egypro.2017.03.665.

[42] Wanke; Liu Cao Zhiyin; Chang Yuhua; Szumanowski Antoni., Wanke Cao, Zhiyin Liu, Yuhua Chang, and Antoni Szumanowski. Direct Yaw-Moment Control of All-Wheel-Independent-Drive Electric Vehicles with Network-Induced Delays through Parameter-Dependent Fuzzy SMC Approach. *Mathematical Problems in Engineering*, 2017, 2017. ISSN 15635147. doi: 10.1155/2017/5170492.

[43] Shihong Ding and Jinlin Sun. Direct yaw-moment control for 4WID electric vehicle via finite-time control technique. *Nonlinear Dynamics*, 88(1):239–254, 2017. ISSN 1573-269X. doi: 10.1007/s11071-016-3240-0.

[44] E. Esmailzadeh, A. Goodarzi, and G. R. Vossoughi. Optimal yaw moment control law for improved vehicle handling. *Mechatronics*, 13(7):659–675, 9 2003. ISSN 09574158. doi: 10.1016/S0957-4158(02)00036-3.

[45] Kaoru Sawase, Yuichi Ushiroda, and Takami Miura. Left-Right Torque Vectoring Technology as the Core of Super All Wheel Control (S-AWC), 2006.

[46] Dieter Schramm, Manfred Hiller, and Roberto Bardini. Single Track Models. In *Vehicle Dynamics: Modeling and Simulation*, pages 225–257. Springer Berlin Heidelberg, Berlin, Heidelberg, 2018. ISBN 978-3-662-54483-9. doi: 10.1007/978-3-662-54483-9_10.

[47] B L Boada, M J L Boada, and V Diaz. Vehicle sideslip angle measurement based on sensor data fusion using an integrated ANFIS and an Unscented Kalman Filter algorithm. *Mechanical Systems and Signal Processing*, 72-73:832–845, 2016. ISSN 0888-3270. doi: https://doi.org/10.1016/j.ymssp.2015.11.003.

[48] Giseo Park, Seibum B Choi, Dongyoon Hyun, and Jounghee Lee. Integrated observer approach using in-vehicle sensors and GPS for vehicle state estimation. *Mechatronics*, 50:134–147, 2018. ISSN 0957-4158. doi: https://doi.org/10.1016/j.mechatronics.2018.02.004.

[49] Husain Kanchwala, Pablo Luque Rodriguez, Daniel Alvarez Mantaras, Johan Wideberg, and Sagar Bendre. Obtaining Desired Vehicle Dynamics Characteristics with Independently Controlled In-Wheel Motors: State of Art Review. *SAE International Journal of Passenger Cars - Mechanical Systems*, 10(2):413–425, 2017. ISSN 19464002. doi: 10.4271/2017-01-9680.

[50] Cheng Lin and Zhifeng Xu. Wheel torque distribution of four-wheel-drive electric vehicles based on multi-objective optimization. *Energies*, 8(5):3815–3831, 2015.

[51] Andy Wong, Dhanaraja Kasinathan, Amir Khajepour, Shih Ken Chen, and Bakhtiar Litkouhi. Integrated torque vectoring and power management framework for electric vehicles. *Control Engineering Practice*, 48:22–36, 2016. ISSN 09670661. doi: 10.1016/j.conengprac.2015.12.012.

[52] Hao Hui-min Li, Xiao-bo Wang, Shang-bin Song, and Hao Hui-min Li. Vehicle Control Strategies Analysis Based on PID and Fuzzy Logic Control. *Procedia Engineering*, 137:234–243, 2016. ISSN 1877-7058. doi: https://doi.org/10.1016/j.proeng.2016.01.255.

[53] Leonardo De Novellis, Aldo Sorniotti, Patrick Gruber, and Andrew Pennycott. Comparison of feedback control techniques for torque-vectoring control of fully electric vehicles. *IEEE Transactions on Vehicular Technology*, 63(8):3612–3623, 2014. ISSN 00189545. doi: 10.1109/TVT.2014.2305475.

[54] J Ghosh, A Tonoli, and N Amati. A Torque Vectoring Strategy for Improving the Performance of a Rear Wheel Drive Electric Vehicle. In *2015 IEEE Vehicle Power and Propulsion Conference (VPPC)*, pages 1–6, 2015. doi: 10.1109/VPPC.2015.7352887.

[55] C J Kim, A A Mian, S H Kim, S H Back, H B Jang, J H Jang, and C S Han. Performance evaluation of integrated control of direct yaw moment and slip ratio control for electric vehicle with rear in-wheel motors on split-mu road. *International Journal of Automotive Technology*, 16(6):939–946, 2015. ISSN 1976-3832. doi: 10.1007/s12239-015-0096-0.

[56] Feihua Huang, Chunyun Fu, Xiaolin Tang, and Minghui Hu. Study on stability and handling characteristics and control of four-wheel-drive electric vehicles. *Advances in Mechanical Engineering*, 9(12):1687814017737725, 2017. ISSN 1687-8140. doi: 10.1177/1687814017737725.

[57] Jyotishman Ghosh, Andrea Tonoli, and Nicola Amati. Improvement of Lap-Time of a Rear Wheel Drive Electric Racing Vehicle by a Novel Motor Torque Control Strategy. *SAE Technical Papers*, 2017-March(March), 2017. ISSN 01487191. doi: 10.4271/2017-01-0509.

[58] Zhengyuan Wang, Umberto Montanaro, Saber Fallah, Aldo Sorniotti, and Basilio Lenzo. A gain scheduled robust linear quadratic regulator for vehicle direct yaw moment Control. *Mechatronics*, 51(January):31–45, 2018. ISSN 09574158. doi: 10.1016/j.mechatronics.2018.01.013.

[59] Kiumars Jalali. *Stability Control of Electric Vehicles with In-wheel Motors*. PhD thesis, 2010. URL `http://hdl.handle.net/10012/5268`.

[60] Milad Jalali, Ehsan Hashemi, Amir Khajepour, Shih-ken ken Chen, and Bakhtiar Litkouhi. Integrated model predictive control and velocity estimation of electric vehicles. *Mechatronics*, 46:84–100, 2017. ISSN 09574158. doi: 10.1016/j.mechatronics.2017.07.002.

[61] K Han, M Choi, and S Choi. Estimation of Tire Cornering Stiffness as a Road Surface Classification Indicator Using Understeering Characteristics. *IEEE Transactions on Vehicular Technology*, page 1, 2018. ISSN 0018-9545. doi: 10.1109/TVT.2018.2820094.

[62] Johannes Edrén, Jenny Jerrelind, Annika Stensson Trigell, Lars Drugge, Annika Stensson Trigell, and Lars Dugge. Implementation and evaluation of force allocation control of a down-scaled prototype vehicle with wheel corner modules. *International Journal of Vehicle Systems Modelling and Testing*, 8(4):335–363, 2013. ISSN 17456444. doi: 10.1504/IJVSMT.2013.057528.

[63] Chunyun Fu, Reza Hoseinnezhad, Kuining Li, and Minghui Hu. A novel adaptive sliding mode control approach for electric vehicle direct yaw-moment control. *Advances in Mechanical Engineering*, 10(10):1687814018803179, 2018. doi: 10.1177/1687814018803179.

[64] Youngjin Jang, Minyoung Lee, In-Soo Suh, and Kwanghee Nam. Lateral handling improvement with dynamic curvature control for an independent rear wheel drive EV. *International Journal of Automotive Technology*, 18(3):505–510, 2017. ISSN 1976-3832. doi: 10.1007/s12239-017-0050-4.

[65] Kanwar Bharat Singh. Vehicle Sideslip Angle Estimation Based on Tire Model Adaptation. *Electronics*, 8(2), 2 2019. ISSN 2079-9292. doi: 10.3390/electronics8020199.

[66] Damrongrit Piyabongkarn, Rajesh Rajamani, John A. Grogg, and Jae Y. Lew. Development and experimental evaluation of a slip angle estimator for vehicle stability control. *IEEE Transactions on Control Systems Technology*, 17(1):78–88, 2009. ISSN 10636536. doi: 10.1109/TCST.2008.922503.

[67] Seyed Mohammad Mehdi Jaafari and Kourosh Heidari Shirazi. Integrated vehicle dynamics control via torque vectoring differential and electronic stability control to

improve vehicle handling and stability performance. *Journal of Dynamic Systems, Measurement and Control, Transactions of the ASME*, 140(7):071003–071003, 2018. ISSN 15289028. doi: 10.1115/1.4038657.

[68] S. Melzi and E. Sabbioni. On the vehicle sideslip angle estimation through neural networks: Numerical and experimental results. *Mechanical Systems and Signal Processing*, 25(6):2005–2019, 2011. ISSN 08883270. doi: 10.1016/j.ymssp.2010.10.015.

[69] Ehsan Hashemi, Saeid Khosravani, Amir Khajepour, Alireza Kasaiezadeh, Shih-Ken Chen, and Bakhtiar Litkouhi. Longitudinal vehicle state estimation using nonlinear and parameter-varying observers. *Mechatronics*, 43:28–39, 2017. ISSN 0957-4158. doi: https://doi.org/10.1016/j.mechatronics.2017.02.004.

[70] H Okajima, S Yonaha, N Matsunaga, and S Kawaji. Direct Yaw-moment Control method for electric vehicles to follow the desired path by driver. In *Proceedings of SICE Annual Conference 2010*, pages 642–647, 2010.

[71] Aria Noori Asiabar and Reza Kazemi. A direct yaw moment controller for a four in-wheel motor drive electric vehicle using adaptive sliding mode control. *Proceedings of the Institution of Mechanical Engineers, Part K: Journal of Multi-body Dynamics*, 233(3):549–567, 2019. doi: 10.1177/1464419318807700.

[72] Zhenpo Wang, Yachao Wang, Lei Zhang, and Mingchun Liu. Vehicle Stability Enhancement through Hierarchical Control for a Four-Wheel-Independently-Actuated Electric Vehicle. *Energies*, 10(7), 2017.

[73] Y. Zeyada, E. El-Beheiry, M. El-Arabi, and D. Karnopp. Driver Modeling Using Fuzzy Logic Controls For Human-in-the-Loop Vehicle Simulations. In *Current Advances in Mechanical Design and Production VII*. Elsevier, 2000. doi: 10.1016/B978-008043711-8/50009-X.

[74] Amir Soltani and Francis Assadian. A Hardware-in-the-Loop Facility for Integrated Vehicle Dynamics Control System Design and Validation. *IFAC-PapersOnLine*, 49 (21):32–38, 2016. ISSN 24058963. doi: 10.1016/j.ifacol.2016.10.507.

[75] Masato Abe. Vehicle Motion with Human Driver. In *Vehicle Handling Dynamics*. Elsevier, 2015. doi: 10.1016/B978-0-08-100390-9.00010-5.

[76] ISO 8855:2011. Road vehicles — Vehicle dynamics and road-holding ability — Vocabulary, 2011.

[77] Hans Pacejka and I J M Besselink. *Tire and Vehicle Dynamics*. Elsevier Science & Technology, Oxford, UNITED KINGDOM, 2012. ISBN 9780080970172. URL `http://ebookcentral.proquest.com/lib/uts/detail.action?docID=892225`.

[78] Mike Blundell and Damian Harty. *The Multibody Systems Approach to Vehicle Dynamics*. Elsevier, 2015. ISBN 9780080994253. doi: 10.1016/C2012-0-07000-7.

[79] C. Peng, P. A. Cowell, C. J. Chisholm, and J. A. Lines. Lateral tyre dynamic characteristics. *Journal of Terramechanics*, 31(6):395–414, 11 1994. ISSN 0022-4898. doi: 10.1016/0022-4898(94)90025-6.

[80] Howard Dugoff, P. S. Fancher, and Leonard Segel. An Analysis of Tire Traction Properties and Their Influence on Vehicle Dynamic Performance. In *International Automobile Safety Conference*, 2 1970. doi: 10.4271/700377.

[81] Shaopu Yang, Yongjie Lu, and Shaohua Li. An overview on vehicle dynamics. *International Journal of Dynamics and Control*, 1(4):385–395, 2013. ISSN 2195-2698. doi: 10.1007/s40435-013-0032-y.

[82] Hans B. Pacejka and Egbert Bakker. The magic formula tyre model. *Vehicle System Dynamics*, 21(sup1):1–18, 1992. ISSN 17445159. doi: 10.1080/00423119208969994.

[83] Wuwei Chen, Hansong Xiao, Qidong Wang, Linfeng Zhao, and Maofei Zhu. *Integrated Vehicle Dynamics and Control*. John Wiley & Sons Singapore Pte. Ltd, Singapore, 4 2016. ISBN 9781118380000. doi: 10.1002/9781118380000.

[84] S Ding, L Liu, and W.X.; Zheng. Sliding Mode Direct Yaw-Moment Control Design for In-Wheel Electric Vehicles. *IEEE Transactions on Industrial Electronics*, 64(8): 6752–6762, 2017. ISSN 0278-0046. doi: 10.1109/TIE.2017.2682024.

[85] D V Thang Truong, M Meywerk, and W Tomaske. Torque vectoring for rear axle using Adaptive Sliding Mode Control. In *2013 International Conference on Control, Automation and Information Sciences (ICCAIS)*, pages 328–333, 2013. ISBN null. doi: 10.1109/ICCAIS.2013.6720577.

[86] K Nam, H Fujimoto, and Y Hori. Lateral stability control of in-wheel-motor-driven electric vehicles based on sideslip angle estimation using lateral tire force sensors. *IEEE Transactions on Vehicular Technology*, 61(5):1972–1985, 2012. doi: 10.1109/TVT.2012.2191627.

[87] Hui Zhang and Junmin Wang. Vehicle Lateral Dynamics Control Through AFS/DYC and Robust Gain-Scheduling Approach. *IEEE Transactions on Vehicular Technology*, 65(1):489–494, 1 2016. ISSN 0018-9545. doi: 10.1109/TVT.2015.2391184.

[88] M. K. Aripin, Yahaya Md Sam, Kumeresan A. Danapalasingam, Kemao Peng, N. Hamzah, M. F. Ismail, Yahaya Md Sam, Kumeresan A. Danapalasingam, Kemao Peng, N. Hamzah, and M. F. Ismail. A review of active yaw control system for vehicle handling and stability enhancement. *International Journal of Vehicular Technology*, 2014:15, 2014. ISSN 16875710. doi: 10.1155/2014/437515.

[89] A Ahmed and B Özkan. Simulation of Stability Control for In-Wheel Motored Vehicle Using Fuzzy PID Controller. In *Automotive and vehicle Technologies Conference Proceedings*, 2015.

[90] Massimo Guiggiani. *The Science of Vehicle Dynamics*. Springer Netherlands, Dordrecht, 2014. ISBN 978-94-017-8532-7. doi: 10.1007/978-94-017-8533-4.

[91] Rajesh Rajamani. *Vehicle Dynamics and Control*. Springer US, Boston, MA, 2012. ISBN 978-1-4614-1432-2. doi: 10.1007/978-1-4614-1433-9.

[92] Reza N. Jazar. *Vehicle Dynamics*. Springer International Publishing, Cham, 2017. ISBN 978-3-319-53440-4. doi: 10.1007/978-3-319-53441-1.

[93] Masato Abe. *Vehicle Handling Dynamics : Theory and Application*. Elsevier Science & Technology, Oxford, UNITED KINGDOM, 2015. ISBN 9780081003732. URL `http://ebookcentral.proquest.com/lib/uts/detail.action?docID=2030668`.

[94] Uwe Kiencke and Lars Nielsen. *Automotive Control Systems*. Springer Berlin Heidelberg, Berlin, Heidelberg, 2005. ISBN 978-3-540-23139-4. doi: 10.1007/b137654.

[95] Bing; Guo Zhu Li Tong; Zhao Jian; Gao Fang; Pan Zhen, Bing Zhu, Litong Guo, Jian Zhao, Fang Gao, Zhen Pan, and Luquan Ren. Direct yaw-moment control through optimal control allocation method for light vehicle. *Applied Mechanics and Materials*, 246-247:847–852, 2013. ISSN 16609336. doi: 10.4028/www.scientific.net/AMM.246-247.847.

[96] Anna Lidfors Lindqvist and Paul D Walker. Handling Dynamics of a Lightweight Solar-Electric Vehicle with Direct Yaw Moment Control. In *Advances in Dynamics of Vehicles on Roads and Tracks*, pages 1169–1177. 2020. ISBN 978-3-030-38076-2. doi: 10.1007/978-3-030-38077-9_136.

[97] Kun Jiang, Adina Pavelescu, Alessandro Victorino, and Ali Charara. Estimation of vehicle's vertical and lateral tire forces considering road angle and road irregularity. In *2014 17th IEEE International Conference on Intelligent Transportation Systems, ITSC 2014*, pages 342–347. Institute of Electrical and Electronics Engineers Inc., 11 2014. ISBN 9781479960781. doi: 10.1109/ITSC.2014.6957714.

[98] Yanjun Li, Guodong Yin, XianJian Jian Jin, Chentong Bian, and Jianqiu Li. Impact of Delays for Electric Vehicles with Direct Yaw Moment Control. *Journal of Dynamic Systems, Measurement and Control, Transactions of the ASME*, 137(12):1–8, 2015. ISSN 15289028. doi: 10.1115/1.4031479.

[99] Mahmut Temel Özdemir and Dursun Öztürk. Comparative performance analysis of optimal PID parameters tuning based on the optics inspired optimization methods for automatic generation control. *Energies*, 10(12):2134, 2017.

[100] Karl Henrik Johansson, Martin Törngren, and Lars Nielsen. Vehicle Applications of Controller Area Network. In William S Hristu-Varsakelis Dimitrios }and Levine, editor, *Handbook of Networked and Embedded Control Systems*, pages 741–765. Birkhäuser Boston, Boston, MA, 2005. ISBN 978-0-8176-4404-8. doi: 10.1007/0-8176-4404-0_32.

[101] Manon Kok, Jeroen D. Hol, and Thomas B. Schön. Using Inertial Sensors for Position and Orientation Estimation. *Foundations and Trends® in Signal Processing*, 11(1-2), 2017. ISSN 1932-8346. doi: 10.1561/2000000094.

[102] Christopher Jekeli. *Inertial Navigation Systems with Geodetic Applications*. De Gruyter, Inc., Berlin/Boston, GERMANY, 2000. ISBN 9783110800234. URL `http://ebookcentral.proquest.com/lib/uts/detail.action?docID=3044618`.

[103] Donald Selmanaj, Matteo Corno, Giulio Panzani, and Sergio M. Savaresi. Vehicle sideslip estimation: A kinematic based approach. *Control Engineering Practice*, 67: 1–12, 10 2017. ISSN 09670661. doi: 10.1016/j.conengprac.2017.06.013.

[104] Saied Taheri and Kanwar Bharat Singh. Integrated state and parameter estimation for vehicle dynamics control. *International Journal of Vehicle Performance*, 5(4), 2019. ISSN 1745-3194. doi: 10.1504/IJVP.2019.10025783.

[105] Kwanghyun Cho, Hyunwoo Son, Seibum B. Choi, and Sukchang Kang. Lateral acceleration compensation of a vehicle based on roll angle estimation. In *2010 IEEE International Conference on Control Applications*. IEEE, 9 2010. ISBN 978-1-4244-5362-7. doi: 10.1109/CCA.2010.5611095.

[106] E.L. Ding and T. Massel. ESTIMATION OF VEHICLE ROLL ANGLE. *IFAC Proceedings Volumes*, 38(1), 2005. ISSN 14746670. doi: 10.3182/20050703-6-CZ-1902.01908.

[107] Rutger Uli. *Non-lagging effect of motorcycle tyres : an experimental study with the flat plank tyre tester*. Technische Universiteit Eindhoven, Eindhoven, 2006.